INFN/AExxx, LAL-xxx, SLAC-R-xxx

Super*B* Detector Technical Design Report

Abstract

This report describes the technical design detector for Super$B$.

E. Grauges,
Universitat De Barcelona, *Fac. Fisica. Dept. ECM Barcelona E-08028, Spain*

G. Donvito, B. Santeramo, V. Spinoso
INFN Bari *and* **Università di Bari,** *Dipartimento di Fisica, I-70126 Bari, Italy*

M. Manghisoni, V. Re, G. Traversi
INFN Pavia *and* **Università di Bergamo** *Dipartimento di Ingegneria Industriale, I-24129 Bergamo, Italy*

G. Eigen, D. Fehlker, L. Helleve
University of Bergen, *Institute of Physics, N-5007 Bergen, Norway*

A. Carbone, R. Di Sipio, A. Gabrielli, D. Galli, F. Giorgi, C. Grandi, U. Marconi, S. Perazzini, C. Sbarra, V. Vagnoni, S. Valentinetti, M. Villa, A. Zoccoli
INFN Bologna *and* **Università di Bologna,** *Dipartimento di Fisica, I-40127 Bologna, Italy*

C. Cheng, A. Chivukula, D. Doll, B. Echenard, D. Hitlin, P. Ongmongkolkul, F. Porter, A. Rakitin, M. Thomas, R. Zhu
California Institute of Technology, *Pasadena, California 91125, USA*

G. Tatishvili
Carleton University, *Ottawa, Ontario, Canada K1S 5B6*

R. Andreassen, C. Fabby, B. Meadows, A. Simpson, M. Sokoloff, K. Tomko
University of Cincinnati, *Cincinnati, Ohio 45221, USA*

M. Andreotti, W. Baldini, R. Calabrese, V. Carassiti, G. Cibinetto, A. Cotta Ramusino, A. Gianoli, E. Luppi, E. Luppi, M. Munerato, L. Tomassetti
INFN Ferrara *and* **Università di Ferrara,** *Dipartimento di Fisica, I-44100 Ferrara, Italy*

D. Stoker
University of California, Irvine *Irvine, California 92697, USA*

O. Bezshyyko, G. Dolinska
Taras Shevchenko National University of Kyiv *Kyiv, 01601, Ukraine*

N. Arnaud, C. Beigbeder, F. Bogard, D. Breton, L. Burmistrov, D. Charlet, A. El Berni, J. Maalmi, V. Puill, A. Stocchi, V. Tocut, S. Wallon, G. Wormser
Laboratoire de l'Accélérateur Linéaire, *IN2P3/CNRS, Université Paris-Sud 11, F-91898 Orsay, France*

J.-F. Muraz, J.-S. Real
Laboratoire de Physique Subatomique et Cosmologie, *IN2P3/CNRS, Université Joseph Fourier Grenoble 1 & Institut Polytechnique de Grenoble, 53 rue des Martyrs F-38026 Grenoble Cedex, France*

D. Brown
Lawrence Berkeley National Laboratory, *University of California, Berkeley, California 94720, USA*

A. Calcaterra, R. de Sangro, G. Felici, G. Finocchiaro, P. Patteri, I. Peruzzi, M. Piccolo, M. Rama
Laboratori Nazionali di Frascati dell'INFN, *I-00044 Frascati, Italy*

S. Fantinel, G. Maron
Laboratori Nazionali di Legnaro dell'INFN, *I-35020 Legnaro, Italy*

E. Ben-Haim, G. Calderini, G. Marchiori
Laboratoire de Physique Nucléaire et de Hautes Energies, *IN2P3/CNRS, Université Pierre et Marie Curie-Paris 6, F-75005 Paris, France*

R. Cenci, A. Jawahery, D.A. Roberts
University of Maryland, *College Park, Maryland 20742, USA*

D. Lindemann, P. Patel, S. Robertson, D. Swersky
McGill University, *Montréal, Québec, Canada H3A 2T8*

P. Biassoni, M. Citterio, V. Liberali, F. Palombo, A. Stabile, S. Stracka
INFN Milano *and* **Università di Milano,** *Dipartimento di Fisica, I-20133 Milano, Italy*

A. Aloisio, G. De Nardo, A. Doria, R. Giordano, A. Ordine, S. Pardi, G. Russo, C. Sciacca
INFN Napoli *and* **Università di Napoli Federico II,** *Dipartimento di Scienze Fisiche, I-80126, Napoli, Italy*

A.Y. Barniakov, M.Y. Barniakov, V.E. Blinov, V.P. Druzhinin, V.B.. Golubev, S.A. Kononov, E. Kravchenko, A.P. Onuchin, S.I. Serednyakov, Y.I. Skovpen, E.P. Solodov
Budker Institute of Nuclear Physics, *Novosibirsk 630090, Russia*

M. Bellato, M. Benettoni, M. Corvo, A. Crescente, F. Dal Corso, C. Fanin, E. Feltresi, N. Gagliardi, S. Longo, M. Morandin, M. Posocco, M. Rotondo, G. Simi, R. Stroili
INFN Padova *and* **Università di Padova,** *Dipartimento di Fisica, I-35131 Padova, Italy*

C. Andreoli, L. Gaioni, E. Pozzati, L. Ratti, V. Speziali
INFN Pavia *and* **Università di Pavia,** *Dipartimento di Elettronica, I-27100 Pavia, Italy*

D. Aisa, M. Bizzarri, C. Cecchi, S. Germani, P. Lubrano, E. Manoni, A. Papi, A. Piluso , A. Rossi
INFN Perugia *and* **Università di Perugia,** *Dipartimento di Fisica, I-06123 Perugia, Italy*

M. Lebeau
INFN Perugia, *I-06123 Perugia, Italy, and*
California Institute of Technology, *Pasadena, California 91125, USA*

A. Fella
INFN Pisa *I-56124 Pisa, Italy and* **Laboratoire de l'Accélérateur Linéaire,** *IN2P3/CNRS, Université Paris-Sud 11, F-91898 Orsay, France and* **Università di Ferrara,** *Dipartimento di Fisica, I-44100 Ferrara, Italy*

C. Avanzini, G. Batignani, S. Bettarini, F. Bosi, M. Ceccanti, A. Cervelli, A. Ciampa, F. Crescioli, M. Dell'Orso, D. Fabiani, F. Forti, P. Giannetti, M. Giorgi, S. Gregucci, A. Lusiani, P. Mammini, G. Marchiori, M. Massa, E. Mazzoni, F. Morsani, N. Neri, E. Paoloni, L. Perez Perez, M. Piendibene, A. Profeti, G. Rizzo, L. Sartori, J. Walsh, E. Yurtsev
INFN Pisa, Università di Pisa, *Dipartimento di Fisica, and* **Scuola Normale Superiore,** *I-56127 Pisa, Italy*

D.M. Asner, J. E. Fast, R.T. Kouzes,
Pacific Northwest National Laboratory, *Richland, Washington 99352, USA*

A. Bevan, F. Gannaway, J. Mistry, C. Walker
Queen Mary, *University of London, London E1 4NS, United Kingdom*

C.A.J. Brew, R.E. Coath, J.P. Crooks, R.M. Harper, A. Lintern, A. Nichols, M. Staniztki, R. Turchetta, F.F. Wilson
Rutherford Appleton Laboratory, *Chilton, Didcot, Oxon, OX11 0QX, United Kingdom*

V. Bocci, G. Chiodi, R. Faccini, C. Gargiulo, D. Pinci, L. Recchia, D. Ruggieri
INFN Roma *and* **Università di Roma La Sapienza,** *Dipartimento di Fisica, I-00185 Roma, Italy*

A. Di Simone
INFN Roma Tor Vergata *and* **Università di Roma Tor Vergata,** *Dipartimento di Fisica, I-00133 Roma, Italy*

P. Branchini, A. Passeri, F. Ruggieri, E. Spiriti
INFN Roma Tre *and* **Università di Roma Tre,** *Dipartimento di Fisica, I-00154 Roma, Italy*

D. Aston, M. Convery, G. Dubois-Felsmann, W. Dunwoodie, M. Kelsey, P. Kim, M. Kocian, D. Leith, S. Luitz, D. MacFarlane, B. Ratcliff, M. Sullivan, J. Va'vra, W. Wisniewski, W. Yang
SLAC National Accelerator Laboratory *Stanford, California 94309, USA*

K. Shougaev, A. Soffer
School of Physics and Astronomy, Tel Aviv University *Tel Aviv 69978, Israel*

F. Bianchi, D. Gamba, G. Giraudo, P. Mereu
INFN Torino *and* **Università di Torino,** *Dipartimento di Fisica Sperimentale, I-10125 Torino, Italy*

G. Dalla Betta, G. Fontana, G. Soncini
INFN Padova *and* **Università di Trento,** *ICT Department, I-38050 Trento, Italy*

M. Bomben, L. Bosisio, P. Cristaudo, G. Giacomini, D. Jugovaz, L. Lanceri, I. Rashevskaya, G. Venier, L. Vitale
INFN Trieste*and* **Università di Trieste,** *Dipartimento di Fisica, I-34127 Trieste, Italy*

R. Henderson
TRIUMF *Vancouver, British Columbia, Canada V6T 2A3*

J.-F. Caron, C. Hearty, P. Lu, R. So
University of British Columbia, *Vancouver, British Columbia, Canada V6T 1Z1*

P. Taras
Université de Montreál, *Physique des Particules, Montreál, Québec, Canada H3C 3J7*

A. Agarwal, J. Franta, J.M. Roney
University of Victoria, *Victoria, British Columbia, Canada V8W 3P6*

Contents

1 Particle Identification

Chapter editors: Nicolas Arnaud & Jerry Va'vra

The current version of the plan for the PID TDR chapter can be found at http://mailman.fe.infn.it/superbwiki/images/8/8c/PID_TDR_plan.pdf

The latest version of the PID TDR chapter (updated daily) is available at http://www.slac.stanford.edu/~narnaud/SuperB/DTDR/dtdr-PID.pdf

1.1 Summary of Physics Requirements and Detector Performance goals

1.1.1 Physics requirements

The Standard Model successfully explains the wide variety of experimental data that has been gathered over several decades with energies ranging from under a GeV up to several hundred GeV. At the start of the millennium, the flavor sector was perhaps less explored than the gauge sector, but the PEP-II and KEK-B asymmetric B Factories, and their associated experiments *BABAR* and Belle, have produced a wealth of important flavor physics highlights during the past decade [1]. The most notable experimental objective, the establishment of the Cabibbo-Kobayashi-Maskawa phase as consistent with experimentally observed CP-violating asymmetries in B meson decay, was cited in the award of the 2008 Nobel Prize to Kobayashi & Maskawa [2].

The B Factories have provided a set of unique, over-constrained tests of the Unitarity Triangle. These have, in the main, been found to be consistent with Standard Model predictions. The B factories have done far more physics than originally envisioned; *BABAR* alone has published more than 400 papers in refereed journals to date. Measurements of all three angles of the Unitarity Triangle; the establishment of D^0 mixing; the uncovering of intriguing clues for potential New Physics in B decays; and unveiling an entirely unexpected new spectroscopy, are some examples of important experimental results beyond those initially contemplated. With the LHC now beginning operations, the major experimental discoveries of the next few years will probably be at the energy frontier, where we would hope not only to complete the Standard Model by observing the Higgs particle, but to find signals of New Physics which are widely expected to lie around the 1 TeV energy scale. If found, the New Physics phenomena will need data from very sensitive heavy flavor experiments if they are to be understood in detail. Determining the flavor structure of the New Physics involved requires information on rare b, c and τ decays, and on CP violation in b and c quark decays that only a very high luminosity asymmetric B Factory can provide [3]. On the other hand, if such signatures of New Physics are not observed at the LHC, then the excellent sensitivity provided at the luminosity frontier by a next generation super B-factory provides another avenue to observing New Physics at mass scales up to 10 TeV or more through observation of rare processes involving B and D mesons and studies of lepton flavor violation (LFV) in τ decays.

1.1.2 Detector concept

The DIRC (Detector of Internally Reflected Cherenkov light) [3] is an example of innovative detector technology that has been crucial to the performance of the *BABAR* science program. The DIRC main performance parameters are the following: (a) a measured time resolution per photon of ∼1.7 ns, close to the photomultiplier (PMT) transit time spread of 1.5 ns, (b) a single photon Cherenkov angle resolution of 9.6 mrad for tracks from di-muon events, (c) a Cherenkov angle resolution per track of 2.5 mrad in di-muon events, and (d) a π/K separation greater than 2.5' σ' over the entire track momentum range, from the pion Cherenkov threshold up to 4.2 GeV/c.

An excellent DIRC S/N performance did not come without some effort, and this experience is useful for knowing how we want to design the 'Focusing Detector of Internally Reflected light' (FDIRC) at Super$B$. To obtain the final background performance it was necessary to: (a) apply a tight timing cut of ±8 ns around each event, (b) add a substantial shielding around the beam pipe under the DIRC, which reduced the PMT background by at lest a factor of 6, (c) install many background detectors (here we found, for example, that the rate in neutron detectors correlates with the DIRC background very well, indicating a common origin), and (d) improve operation of the machine. After ∼10 years of operation, the PMT gain was reduced by ∼30%. The electronics dead time was limited to ∼5% at a rate of ∼250 kHz/PMT.

Excellent flavor tagging will continue to be essential for the program of physics anticipated at Super$B$, and the gold standard of particle identification in this energy region is that provided by internally reflecting ring-imaging devices (the DIRC class of ring imaging detectors). The challenge for Super$B$ is to retain (or even improve) the outstanding performance attained by the *BABAR* DIRC [4], while also gaining an essential factor of 100 in background rejection to deal with the much higher luminosity.

A new Cherenkov ring imaging detector is being planned for the Super$B$ barrel, called the Focusing DIRC, or FDIRC. It will reuse the existing *BABAR* bar boxes and mechanical support structure. This structure will be attached to a new photon "camera", which will be optically coupled to the bar box exit window. The new camera design combines a small modular focusing structure that images the photons onto a focal plane instrumented with very fast, highly pixelated, PMTs [5]. These elements should combine to attain the desired performance levels while being at least 100 times less sensitive to backgrounds than the *BABAR* DIRC, while achieving the same PID performance as *BABAR* DIRC.

To cope with higher luminosity, the FDIRC photon camera will provide an overall safety factor of 250 compared to the *BABAR* DIRC. Indeed,

- it is 25× smaller in total than the DIRC water-based camera;
- its new highly pixilated photon detectors will be about 10× faster;
- the photon camera is built using radiation-resistant Fused silica material – instead of water or oil which would be more sensitive to neutron background.

Furthermore, (a) the entire system will have ∼18,000 pixels, (b) will reconstruct photons in 3D (x, y, and time), (c) the Cherenkov angle could be reconstructed based on pixels alone, however, time is included in the final PID likelihood hypothesis, (d) time also plays the important role in FDIRC to reduce the background, and (e) the expected timing resolution of $\sigma\sim$200 ps will also make it possible to reduce the chromatic broadening of Cherenkov angle resolution by 0.5-1 mrad, depending on the photon propagation path length.

Several options were under consideration for a possible PID detector in the forward direction: (a) "DIRC-like TOF" time-of-flight (TOF) [6], (b) pixelated TOF [7] and (c) Aerogel RICH [8]. The chosen technology, based on time-of-flight technique, has been selected by the Super$B$ collaboration in May 2011 and room has been reserved in the Super$B$ design to accommodate this new detector on the forward side. Tests of a full-scale prototype of one sector of the "Forward Time-Of-Flight" (FTOF) detector are foreseen in near future; if they are successful, the FTOF will be included in the Super$B$ baseline. See section 1.5 for more information on this topic.

1.1.3 Charged Particle Identification

The charged particle identification at Super$B$ relies on the same framework as the *BABAR* experiment. Electrons and muons are identified by the EMC and the IFR respectively, aided by dE/dx measurements in the inner trackers (SVT and DCH). Separation for low-momentum hadrons is primarily provided by dE/dx. At higher momenta (above 0.7 GeV/c for pions and kaons, above 1.3 GeV/c for protons), a dedicated system, the FDIRC – inspired by the successful *BABAR* DIRC – will perform the π/K separation.

1.2 Particle Identification Overview

1.2.1 Experience of BABAR DIRC

The *BABAR* DIRC – see Fig. 1.1 – is a novel ring-imaging Cherenkov detector. The Cherenkov light angular information, produced in ultra-pure synthetic fused silica bars, is preserved while propagating along the bar via internal reflections to the camera (the SOB) where an image is produced and detected.

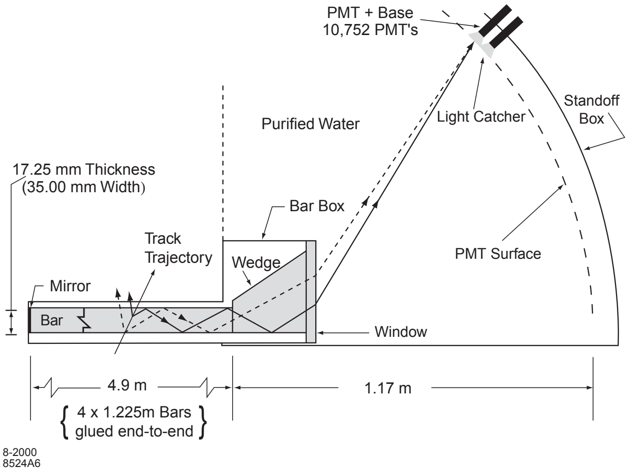

Figure 1.1: Schematic of the *BABAR* DIRC.

The entire DIRC has 144 quartz bars, each 4.9 m long, which are set along the beam line and cover the whole azimuthal range. Thanks to an internal reflection coefficient of ∼0.9997 and orthogonal bar faces, Cherenkov photons are transported to the back end of the bars with the magnitude of their angles conserved and only a modest loss of photons. They exit into a pinhole camera consisting of a large volume of purified water (a medium chosen because it is inexpensive, transparent, and easy to clean, with average index of refraction and relative chromatic dispersion sufficiently close to those of the fused silica). The photon detector PMTs are located at the rear of the SOB, about 1.2 m away from the quartz bar exit window.

The reconstruction of the Cherenkov angle uses information from the tracking system together with the positions of the PMT hits in the DIRC. In addition, information on the time of arrival of hits is used in rejecting background hits, and resolving ambiguities due to the unknown path of a given photon in the quartz.

The *BABAR* DIRC performed reliably and efficiently over the whole *BABAR* data taking period (1999-2008). Its physics performance remained consistent throughout the whole period, although some upgrades, such as the addition of shielding and replacement of electronics, were necessary to cope with evolving machine conditions. Its main performance parameters are the following:

- measured time resolution of about 1.7 ns, close to the PMT transit time spread of 1.5 ns;
- single photon Cherenkov angle resolution of 9.6 mrad for dimuon events;
- Cherenkov angle resolution per track of 2.5 mrad in dimuon events;
- $K - \pi$ separation above 2.5 'σ' from the pion Cherenkov threshold up to 4.2 GeV/c.

1.2.2 Barrel PID: Focusing DIRC (FDIRC)

As discussed above, the PID system in Super$B$ must cope with much higher luminosity-related background rates than in *BABAR* – current estimates are on the order of 100 times higher. The basic strategy is to make the camera much smaller and faster. A new photon camera imaging concept, based on focusing optics, is therefore envisioned. The focusing blocks (FBLOCK), responsible for imaging the Cherenkov photons onto the PMT cathode surfaces, will be machined from radiation-hard pieces of fused silica. The major design constraints for the new camera are the following: (a) it must be consistent with the existing *BABAR* bar box design, as these elements will be reused in Super$B$; (b) it must coexist with the *BABAR* mechanical support and magnetic field constraints; (c) it requires very fine photon detector pixelation and fast photon detectors.

Imaging is provided by a mirror structure focusing onto an image plane containing highly pixelated PMTs. The reduced volume of the new camera and the use of fused silica for coupling to the bar boxes (in place of water as it was in *BABAR* SOB), is expected to reduce the sensitivity to background by about one order of magnitude compared to *BABAR* DIRC. The very fast timing of the new PMTs is expected to provide many additional advantages: (a) an improvement of the Cherenkov resolution; (b) a measure of the chromatic dispersion term in the radiator [9, 10, 11]; (c) separation of ambiguous solutions in the folded optical system; and (d), another order of magnitude improvement in background rejection.

Figure 1.2 shows the new FDIRC photon camera design (see Ref. [5, 12] for more details). It consists of two parts: (a) a focusing block (FBLOCK) with cylindrical and flat mirror surfaces, and (b) a new wedge. The wedge at the end of the bar rotates rays with large transverse angles in the focusing plane before they emerge into the focusing structure. The old wedge is too short so that an additional wedge element must be added to insure that all rays strike the cylindrical mirror. The cylindrical mirror is rotated appropriately to make sure that all rays reflect onto the FBLOCK flat mirror, preventing reflections back into the bar box itself; the flat mirror then reflects rays onto the detector focal plane with an incidence angle of almost 90°, thus avoiding reflections. The focal plane is located in a slightly under-focused position to reduce the FBLOCK size and therefore its weight. Precise focusing is unnecessary, as the finite pixel size would not take advantage of it. The total weight of the solid fused silica FBLOCK is about 80 kg. This significant weight requires good mechanical support.

There are several important advantages gained in moving from the *BABAR* pinhole focused design with water coupling to a focused optical design made of solid fused silica: (a) the design is modular; (b) sensitivity to background, especially to neutrons, is significantly reduced; (c) the pinhole-size component of the angular resolution in the focusing plane can be removed by focusing with cylindrical mirror, and timing can be used to measure the chromatic dispersion, thus improving performance; (d) the total number of photomultipliers is reduced by about one half compared to a non-focusing design with equivalent performance; (e) there is no risk of water leaks into the Super$B$ detector, and no time-consuming maintenance of a water system, as was required to operate *BABAR* safely.

Each new camera will be attached to its *BABAR* bar box with an optical RTV glue, which will be injected in a liquid form between the bar box window and the new camera and cured in place. As Fig. 1.2 shows, the cylindrical mirror focuses in the radial (y) direction, while pinhole focusing is used in the direction out of the plane of the schematic (the x-direction). Photons that enter the FBLOCK at large x angles reflect from the parallel sides, leading to an additional ambiguity. However, the folded design makes the optical piece small, and places the photon detectors in an accessible location, improving both the mechanics and the background sensitivity. Since the optical mapping is 1 to 1 in the y-direction, this “folding” reflection does not create an additional ambiguity. Since a given photon bounces inside the FBLOCK only 2-4 times, the requirements on surface quality and polishing for these optical pieces are much less stringent than that required for the DIRC bar box radiator bars.

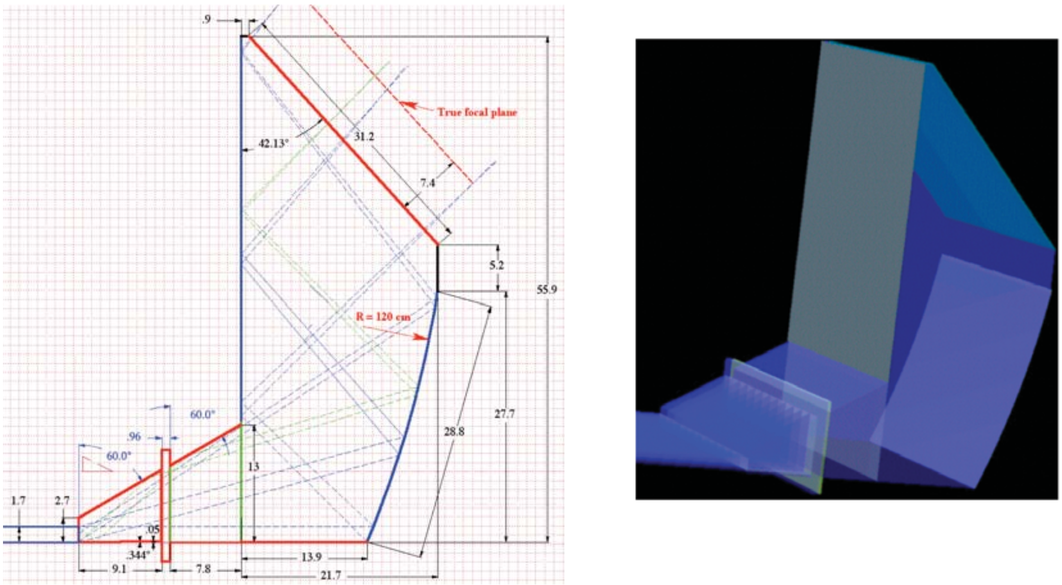

(a) FDIRC optical design (dimensions in cm).

(b) Its equivalent in the Geant4 MC model.

Figure 1.2: Barrel FDIRC Design.

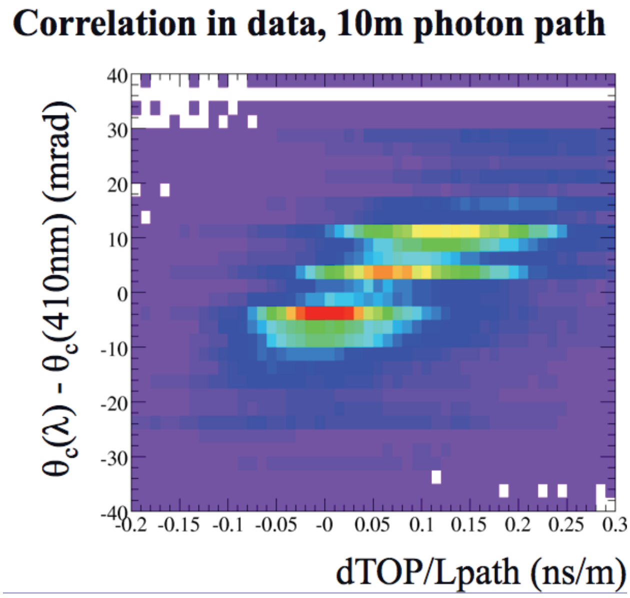

Figure 1.4: The same correlation between the change of the Cherenkov angle and the change in TOP for photons propagating 10 meters in the bar, as seen in the beam test data in the first FDIRC prototype [9, 11].

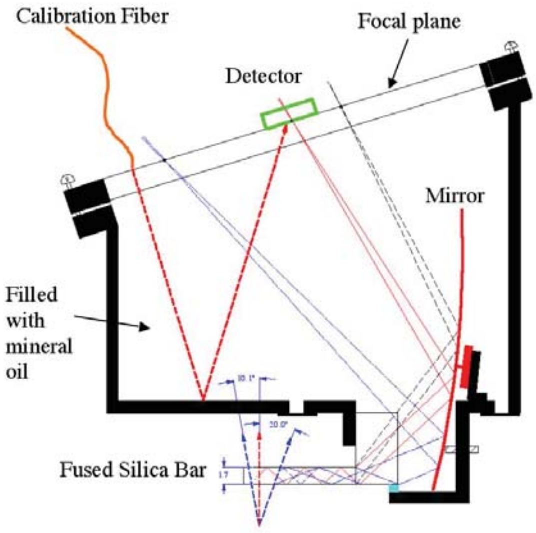

Figure 1.5: The first FDIRC single-bar prototype employing a spherical mirror, oil-filled photon camera, and highly-pixilated photon detectors [9], [10], [11].

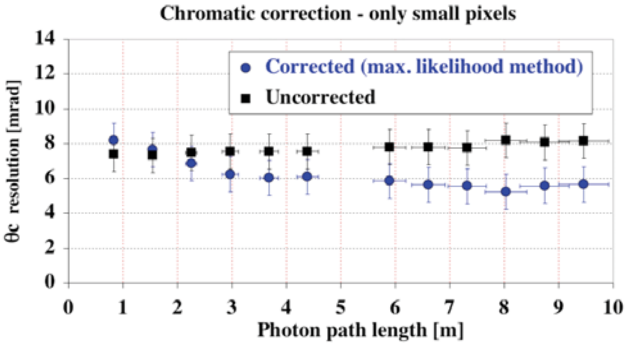

Figure 1.6: Beam test data showing the effect of the chromatic correction for 3 mm × 12 mm pixels obtained with H-9500 MaPMT in the first FDIRC prototype. Note that the Super*B* active region starts 1-2 meters away from the detector camera end. Results with the H-8500 MaPMT are similar, but with slightly worse resolution [9, 11].

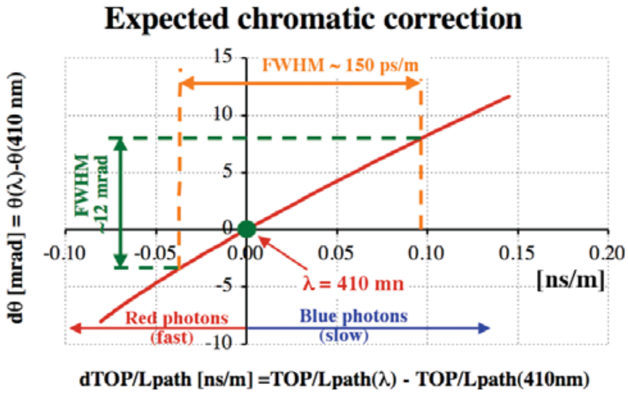

Figure 1.3: Analytical correlation between the variation of the Cherenkov angle and the change in TOP, relative to the mean wavelength of 410 nm [9, 11].

As an intermediate step towards an upgrade of DIRC for the Super*B* detector, we have built and tested the first FDIRC prototype (see Fig. 1.5), in order to learn how to design a smaller FDIRC with new highly-pixilated fast PMTs [9, 11]. This prototype demonstrated for the first time that a chromatic correction could be done with timing. The principle is displayed in Fig. 1.3 showing the analytical correlation between the change of the Cherenkov angle and the change in time-of-propagation (TOP), relative to the mean wavelength of 410 nm. Figure 1.4 shows the same plot, this time with real data from photons propagating 10 meters in the bar. Figure 1.6 shows the final result of the chromatic correction in the beam test data. One can see that the chromatic correction improves the Cherenkov angle resolution by 0.5-1 mrad depending on photon propagation path length. To achieve this, a single photoelectron timing resolution of ∼200 ps is required. This can be achieved with H-8500 or H-9500 MaPMTs.

We have also learned from the first prototype that the Cherenkov ring has worse resolution on the wings than on the center, due to the optical aberration caused by the bar, which is amplified by a mirror. Figures 1.7 and 1.8 show that this error contribution goes from 0 mrad (at ring center) to ∼9 mrad (near the ring wings) and it is *z*-dependent. This aberration is present in the non-focusing *BABAR* DIRC as well, but it is smaller, i.e., the mirror amplifies this effect. The effect is similar for spherical, parabolic and spherical mirrors. For more details see Ref. [12].

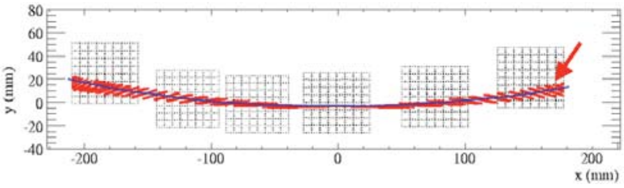

Figure 1.7: Optical ring aberration near the ring wings for the first FDIRC prototype with overlaid detectors and their pixels to show that it is a substantial effect. Calculated for a position in the middle of a bar [9].

Each DIRC wedge inside an existing bar box has a 6 mrad angle at the bottom. This was done intentionally in *BABAR* to provide simple step-wise “focusing” of rays leaving the bar towards negative y to reduce the effect of bar thickness. However, in the new optical system, having this angle on the inner wedge somewhat

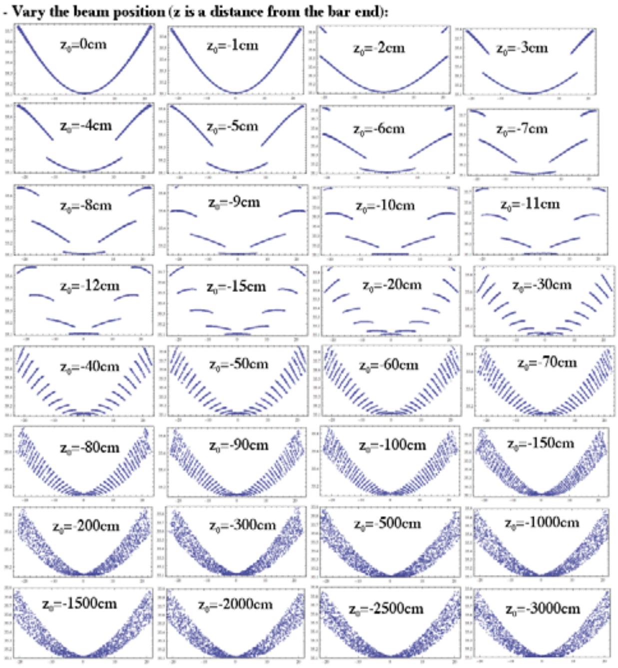

Figure 1.8: Optical ring aberration near the ring wings for the first FDIRC prototype as a function of z-position along the bar [12].

worsens the design FDIRC optics resolution. Figure 1.9 shows the result of a simulation with Mathematica [12]. One can see that the micro-wedge splits the image. There are two choices: (a) either leave it as it is, or (b) glue a micro-wedge at the bottom of the old wedge, inside the bar box, to correct for this angle. Though (b) is possible in principle, it is far from trivial, as the bar box must be opened. Because of this difficulty we have decided for the option (a).

Figure 1.10 shows a Cherenkov ring image for one of the central bars in the new FDIRC. The ring image is more complicated than those from *BABAR* DIRC or from the first FDIRC prototype. This is due to reflections from the sides of the FBLOCK, and the pattern is different for each bar. The image is actually three dimensional and can be simplified if one uses TOP as a way to slice it. The ring radius is not used in the analysis. Instead, we use a dictionary of MC assignments for each pixel: $\mathrm{k}_{\mathrm{pixel}} = (k_x, k_y, k_z)$, and time-of-propagation for direct and indirect photons TOP_{direct} and $\mathrm{TOP}_{indirect}$ for tracks with $\theta_{dip} = 90°$ and $\mathrm{z} = \mathrm{z}_{\mathrm{middle}}$ for each bar. For any other track direction one can then calculate the Cherenkov angle simply as a dot product of two vectors: $\cos\theta_C = k_{\mathrm{track}} \cdot k_{\mathrm{pixel}}$. This procedure has been used successfully with the first FDIRC prototype in the cosmic ray telescope with 3D tracking. In the final physics analysis, the measured photons for each track will be tested against probability distribution functions (PDFs) for each particle hypothesis.

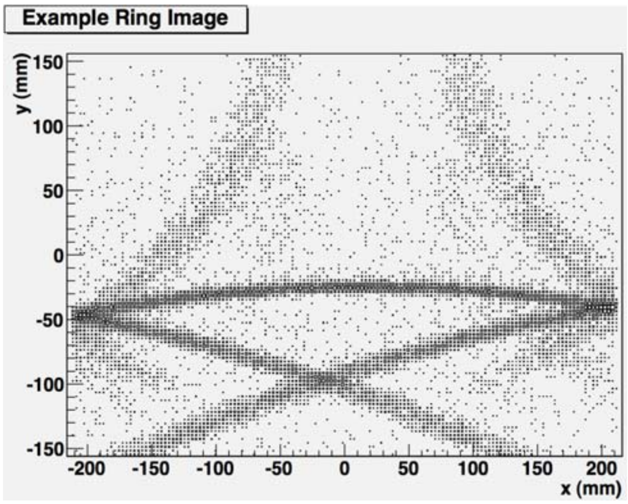

Figure 1.10: Cherenkov ring image from GEANT4 for tracks with $\theta_{\mathrm{dip}} = 90°$ in the central bar at 4 GeV/c [13].

1.3 Projected Performance of FDIRC 2-3 pages

1.3.1 Reconstruction Arnaud, Roberts

1.3.2 MC Simulation

Fast simulation Arnaud

Full simulation Roberts

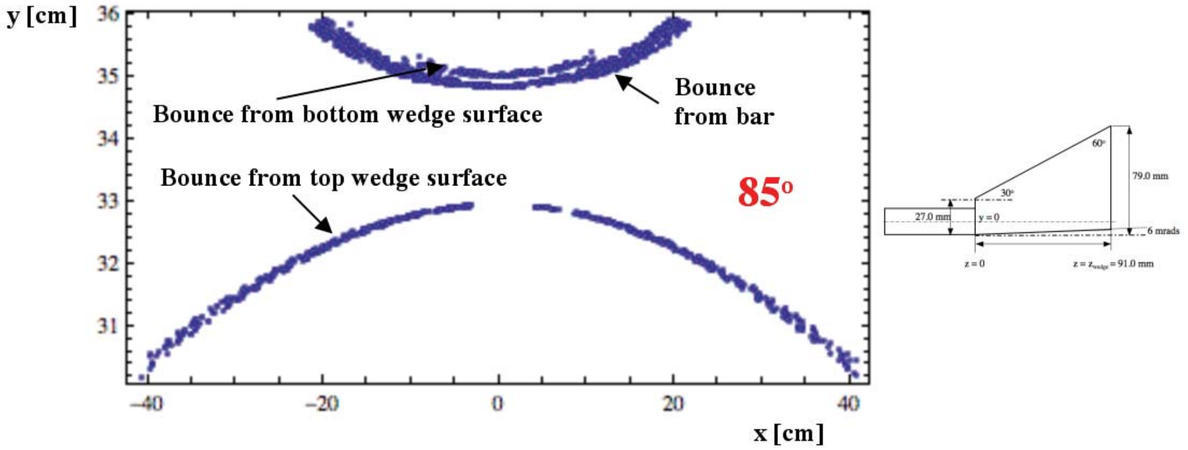

Figure 1.9: Split of Cherenkov ring cause by micro-wedge [12].

1.3.3 Effect of Background on performance **Roberts**

1.4 The Barrel FDIRC Detector Overview

1.4.1 Impact on other systems

Benettoni, Simi, Vavra

1.4.2 Photodetectors

Photon Detector choice There are three photon detectors under consideration, the H-8500 (64 pixels) and the H-9500 (256 pixels), and very recently R-11265-00-M64 (64 pixels) multi-anode PMTs (MaPMT) by Hamamatsu. At present, we have selected the 12-dynode H-8500 tube from several reasons: it is the tube preferred by the medical community and is therefore produced in a larger quantity, it has much smaller price than the H-9500 MaPMT, it has a smaller single electron timing spread (σ_{TTS} ∼140 ps vs. σ_{TTS}∼220 ps), it can be obtained with somewhat enhanced QE (∼24% vs. ∼20%), it has more uniform gain response across its face (1:2 vs. 1:5), and Hamamatsu strongly recommends (at the time of writing this document) not to consider this tube to keep a reasonable delivery schedule of large quantities. On the other hand, H-9500 MaPMT can provide finer sampling in the y-direction and thus provides significantly better Cherenkov angle resolution. We should keep it on the list of possible tubes.

Very recently another Hamamatsu tube, R-11265-00-M64, came up for a consideration [14]. Its main attractions are (a) Super-bialkali QE of 36%, (b) small 2.8 mm pixels, which would allow small binning in y-direction, and therefore better Cherenkov angle resolution, and (c) small dead space around tube boundaries. We would combine 8 small pixels horizontally to create wide pixels in the x-direction, where we do not have focusing; at the same time we would keep the same total number of electronics channels in the system. We will test this tube and decide later. It would require 2304 tubes of this type in the FDIRC system. One should add that Hamamatsu also sells R-11265-00-M16 tube, which has the same pixel size as H-8500 tube. It would be still useful to consider this tube as it has a Super Bialkali QE, and we would benefit from using it. But we would prefer smaller pixel size tube.

The performance of the new FDIRC is simulated with a Geant4 based program [13]. Preliminary results for the expected Cherenkov angle resolution are shown in Table 1.1 for different layouts [5]. Design #1 (a 3 mm × 12 mm pixel size with the micro-wedge glued in) gives a resolution of σ∼8.1 mrad per photon for 4 GeV/c pions at 90° dip angle. The micro-wedge option

FDIRC Design	Option	θ_C resolution [mrad]
1	3 mm×12 mm pixels with a micro-wedge	8.1
2	3 mm×12 mm pixels and no micro-wedge	8.8
3	6 mm×12 mm pixels with a micro-wedge	9.0
4	6 mm×12 mm pixels and no micro-wedge	9.6

Table 1.1: FDIRC performance simulation by Geant4 MC [13].

was supposed to remove a ~6 mrad inclined surface on the old wedge, but adding it would require to open the bar box, and this was judged as too difficult to implement in practice and was discarded. Presently preferred option is #4, which would give $\sigma \sim 9.6$ mrad per photon. This would be a performance about the same as in *BABAR* DIRC [4]. However, if the chromatic correction would be implemented successfully, one could reduce the error by 0.5-1 mrad depending on the photon path length [11].

During the prototyping stage we used H-8500C tube with resistor chain and a HV cable with the SHV connector. In the final application we would still prefer to use the H-8500C tube, as it gives a HV control of each tube - see more discussion in the HV section. This tube comes with a 1.5 mm-thick Borosilicate glass window with a spectral sensitivity between 300 and 650 nm. We would require a minimum QE of ~24%, which corresponds to a blue sensitivity index of 9.5. The dark anode current of this tube is very low (0.1 nA per pixel and 6 nA total), and the after-pulse rate is also almost negligible. Given the design of the dynode structure preventing direct ion backflow to the photocathode, we expect a nominal cathode PMT aging behavior.

Figures 1.11 show (a) a single photoelectron pulse from H-8500 before the amplification at ~1.0 kV, (b) a single electron pulse height spectrum. As one can see from the Hamamatsu spreadsheet shown in Fig. 1.11, the rise time of H-8500 tube is about 0.7 ns. With SLAC amplifier, based on the Analog devices chip AD8000, the amplified rise time was about 1.5 ns, which is sufficient for our purpose. We believe that the tube needs an amplifier with an effective gain of ~40× if one is using a LeCroy 4413 discriminator with a threshold of ~25 mV. Hamamatsu also points out that the pulse height spectra are not uniform across all pixels in a H-8500 tube. How this effect translates into the detection efficiency depends on the type of electronics, noise level and threshold; it will be studied in detail in the FDIRC prototype first using the SLAC amplifier with the IRS-2 waveform digitizing electronics [15], and then be compared to the Super*B* CFD electronics [16] (see section 8.4.6.).

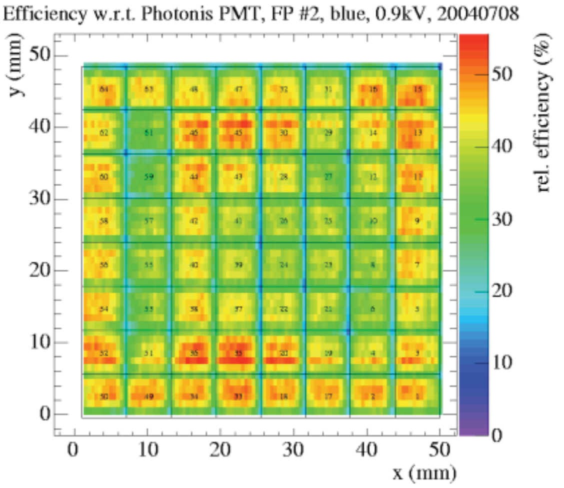

Figure 1.12: Single photoelectron efficiency of a H-8500 tube, normalized to Photonis Quantacon XP2262/B PMT [17].

Figure 1.12 shows the single photoelectron efficiency of a H-8500 tube, normalized to a Photonis Quantacon XP2262/B PMT [17]. This plot was obtained with a SLAC amplifier with

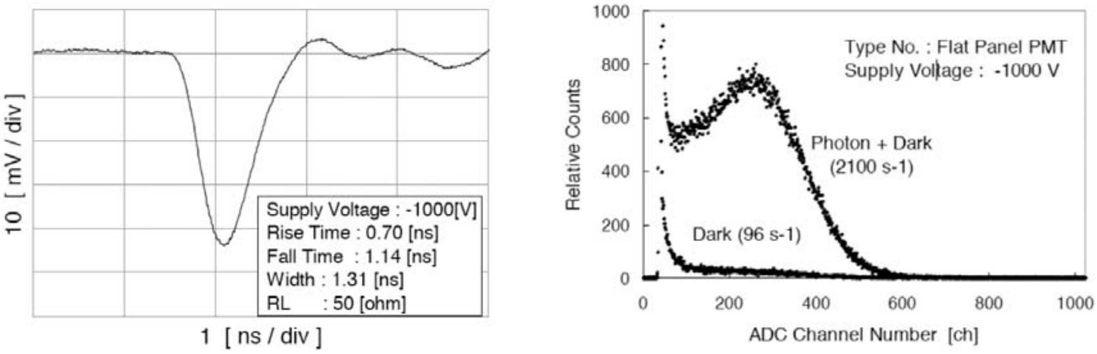

(a) H-8500 MaPMT single electron pulse without an amplifier (response to a 30 ps laser pulse at 407 nm).

(b) H-8500 MaPMT single electron pulse height spectrum.

Figure 1.11: H-8500 MaPMT single electron pulse, noise and single electron pulse height distribution, Hamamatsu data [18].

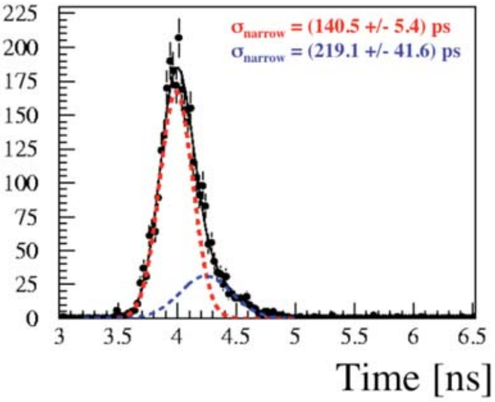

Figure 1.13: The H-8500 single photoelectron transit time resolution is σ_{TTS}~140 ps [17].

Elantek 2075 chip, LeCroy 4413 discriminators with 100mV threshold, LeCroy 3377 TDCs with 0.5 ns/count, and a 407 nm laser. We plan to short two neighboring pixels in the x-direction, as there is only pinhole focusing available, and thus create 3 mm × 12 mm pixels (H-8500), providing 32 readout channels per tube. Each photon camera would have 48 H-8500 MaPMT detectors, which corresponds to a total of 576 tubes for the entire Super$B$ FDIRC, resulting in 18432 pixels total. The H-8500 tube has a pixel size 5.8 mm×5.8 mm, with a pitch between pixels equal to 6.08 mm, the effective detection area of 49 mm × 49 mm, and the H-8500 tube total area of 52 mm × 52 mm.

Figure 1.13 shows H-8500C tube TTS timing resolution with single photoelectrons, indicating σ_{TTS}~140 ps [17], obtained with a laser pointing to the center of a pixel, and using SLAC amplifier with Elantek-2075 chip, Philips 715 CFD and LeCroy 2228A TDC. Hamamatsu data sheets for H-8500 tube indicates a value of FWHM ~400 ps, which gives σ_{TTS}~170 ps. Another measurement comes from R. Montgomery showing an average H-8500 tube TTS resolution of σ_{TTS}~154 ps [19]. This timing performance, coupled to the electronics timing resolution contribution of $\sigma_{Electronics}$~100 ps, allows corrections of the chromatic error for photon path length of more than 2 meters, as long as the total timing resolution per single photon is σ~200 − 250 ps [11].

There is also a new measurement showing that the TTS resolution depends on the position within a given pixel, which is driven by the PMT's electrode structure [20]. The electrode structure, PMT edge effects and gain variation generally degrade the overall TTS resolution, so one should probably assume that the single photoelectron timing resolution is more like 200-

250 ps. This agrees with Fig. 1.14 where we plot TTS timing resolution in the first FDIRC prototype [17], where laser photons populate the entire H-8500 face, i.e., pixels were hit uniformly, including their edges. Figure 1.5 shows how the laser calibration was done in the first FDIRC prototype. This plot probably represents what will be a real TTS performance in practice. Notice also that edge pixels tend to have worse resolution.

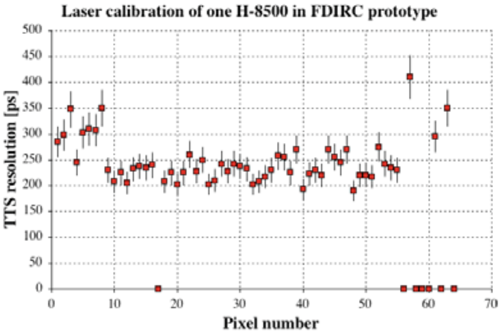

Figure 1.14: The H-8500 single photoelectron transit time resolution across all pixels [17].

There are two effects to take into account when considering interaction between two neighboring pixels: the pixel-to-pixel cross-talk, and the charge sharing avalanche between two pixels. The neighbor pixel-to-pixel single electron cross-talk was measured to be ~3%, when a laser light was placed on the center of a pixel while looking at its neighbor – see Fig. 1.15 (this test used a newer SLAC amplifier with AD8000 chip). However, the pixel-to-pixel cross-talk is even more complicated in all multi-anode tubes [19]. Figure 1.16 shows that the cross-talk depends on the position within a pixel. This will clearly require more study with the FDIRC final electronics. We hoped to utilize the charge sharing, which is related to the avalanche size, to reduce the size of pixels in the y-direction by charge interpolation. However, the attempt to utilize the charge sharing was not successful in this particular tube as it has entrance focusing electrodes defining pixel boundaries, which sweep electrons away from pixel boundaries, *i.e.* Hamamatsu has designed the MaPMT electrode structure in such a way to suppress the charge sharing in these tubes. Both H-8500 and H-9500 have this charge sharing-suppressing feature. Such feature does not exist in MCP-PMT detectors.

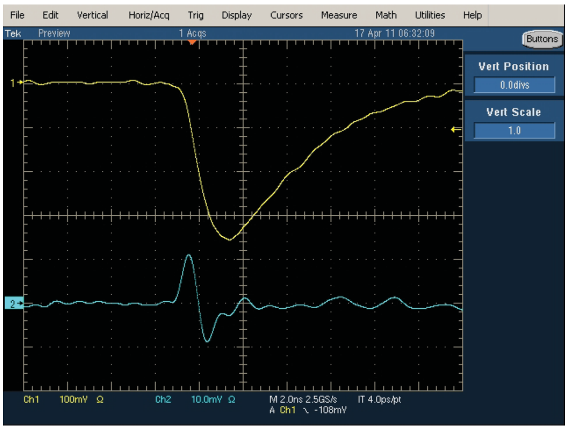

Figure 1.15: The H-8500 tube pixel-to-pixel single electron cross-talk was measured to be ~3%, when the laser light was placed on the center of a pixel while looking at its neighbor [21].

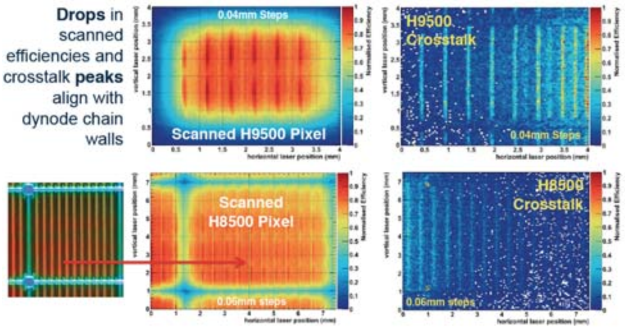

Figure 1.16: Observed periodicities in single electron efficiencies and cross-talk are aligned with the dynode electrode structure [19].

Another special feature of all MaPMT detectors is a double Polya distribution, one corresponding to a photoelectron produced at the cathode and the amplification utilizing all 12

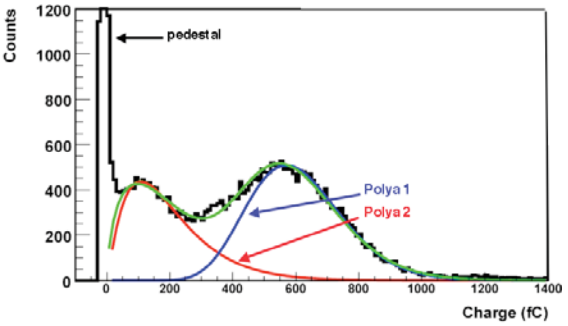

(a) Double-Polya fit to single electron distribution as observed in R7600-03-M16 MaPMT. The lower peak originates from photoelectrons which are missing one amplification stage in the MaPMT [24].

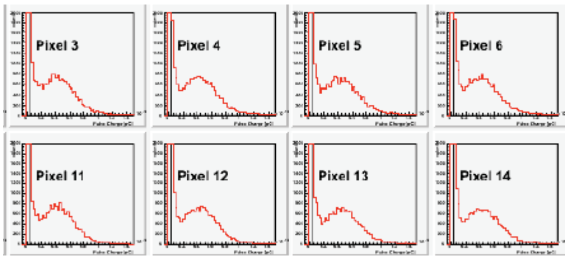

(b) Single electron distributions in H-8500 MaPMT. The lower peak shows up only as a shoulder [23].

Figure 1.17: Single electron pulse height distribution in MaPMTs.

dynodes (this is a nominal distribution), and another one corresponding to a case that a photon produces a photoelectron striking the very first dynode rather than at the photocathode, and the amplification is utilizing only 11 dynodes instead of 12. Missing one amplification stage produces a gain 2-3 smaller than the nominal amplification process, pulses arrive 2-2.5 ns earlier (see Fig. 1.18 [21]). Figure 1.19 shows a time spectrum of normal photoelectrons produced at the cathode, pre-pulse spectrum produced at the first dynode arriving ∼2.5 ns earlier, and backscattered photoelectrons arriving ∼6 ns later [22]. Figures 1.17 show the resulting single electron pulse height spectra either a small shoulder near the pedestal at lower gain [23], or a clear double-Polya distribution at higher gain [24]. Although the pre-pulses are a nuisance, they can be used as normal photoelectrons in the Cherenkov ring analysis and their time can be calibrated out. Their time shift will not affect the chromatic correction, which has a range of only ∼1 ns.

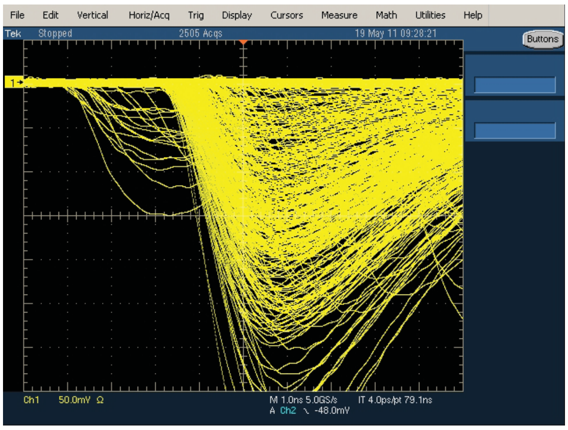

Figure 1.18: The H-8500 single electron pre-pulses corresponding to a case when a photon produces a photoelectron at the very first dynode rather than at the photocathode, and the amplification is utilizing only 11 dynodes instead of 12 [21].

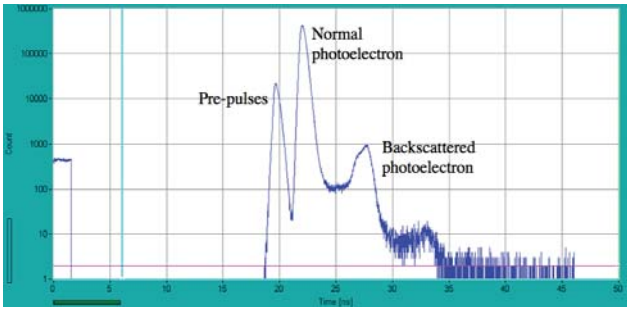

Figure 1.19: The H-8500 single electron time spectrum showing normal photoelectrons, pre-pulses and the backscattered photoelectrons [22].

Figure 1.20 shows that the H-8500 tube gain range is $1 - 3 \times 10^6$ for nominal operating voltage of -1.0 kV [21]. There is a variation of gain from pixel-to-pixel due to non-uniformities in the multi-anode structure. As a result there is a variation in detection efficiency.

Figure 1.21 shows scans of 15 tubes [21], operating at -1.0 kV and -1.1 kV, amplifier gain of

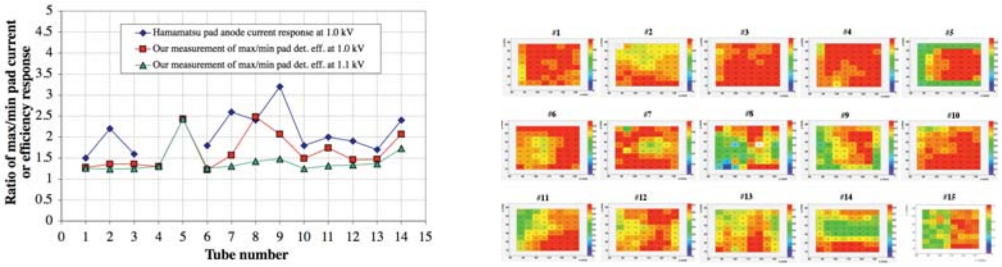

(a) Min-max efficiency uniformity of 64 pixels. This is compared to anode current min-max response across 64 pixels to a fixed photon flux.

(b) Relative efficiency scan of 15 H-8500 tubes operating at -1.0 kV, normalized to XP2262/B PMT).

Figure 1.21: 2D single electron detection efficiency across pixels of 15 H-8500 tubes [21].

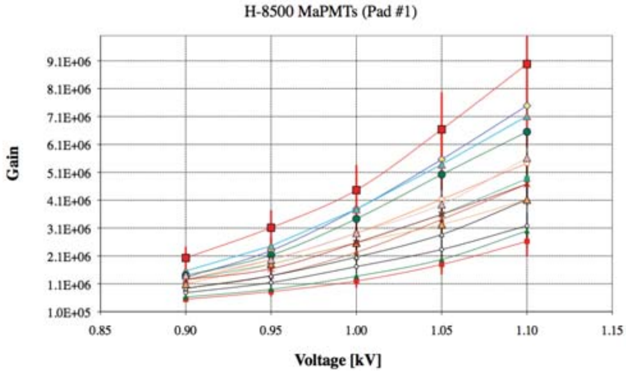

Figure 1.20: The H-8500 tube gain range and dependence on voltage for 14 tubes using pixel 1 in each tube [21].

~40×, a threshold electronics of -25 mV, and indicates that typically the best-to-worst single electron detection efficiency might vary as much as 1:2 across the H-8500 PMT face. This is compared to the anode current response across all pixels to a fixed high photon flux (Hamamatsu data). This figure also shows the efficiency maps of 15 tubes [21], all operating at -1.0 kV, with an amplifier gain of 40×, with a simple threshold electronics, and normalized to the Photonis Quantacon XP2262/B PMT. It indicates that the best-to-worst detection efficiency variation is as much as 1:2 across the H-8500 PMT face. One should stress that the detection efficiency relative to the Quantacon XP2262/B PMT is typically at a level of 40-50% for the worst pixels, and 80-100% for the best pixels.

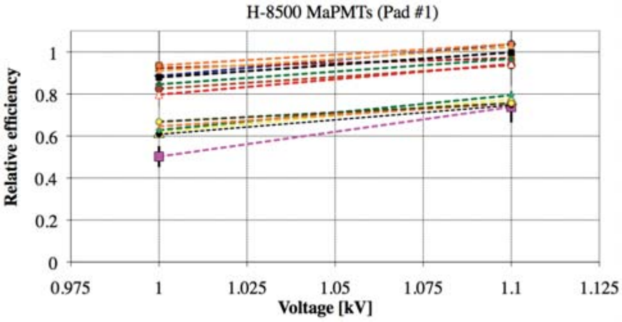

Figure 1.22: The H-8500 single electron detection efficiency dependence on voltage [21].

Figure 1.22 shows how the H-8500 tube single electron detection efficiency depends on voltage [21]. One can see that one can improve the detection efficiency by 10-20% per 100V increase.

There are three possible ways to deal with the pixel-based gain non-uniformity: (a) process each tube, equipped with the final electronics, in a scanning setup; record the individual relative efficiency values and store them into an analysis database, or (b) adjust a discriminator threshold on each pixel, or (c) adjust an amplifier gain on each pixel. This concept has yet to be worked out in detail as this effect depends on details of final electronics. One should remember, when doing the overall gain adjustment, that the absolute maximum voltage on H-8500 is -1.1 kV.

We want to stay below about -1.05 kV for the initial setting to have enough headroom for later period when the detector will loose gain due to aging.

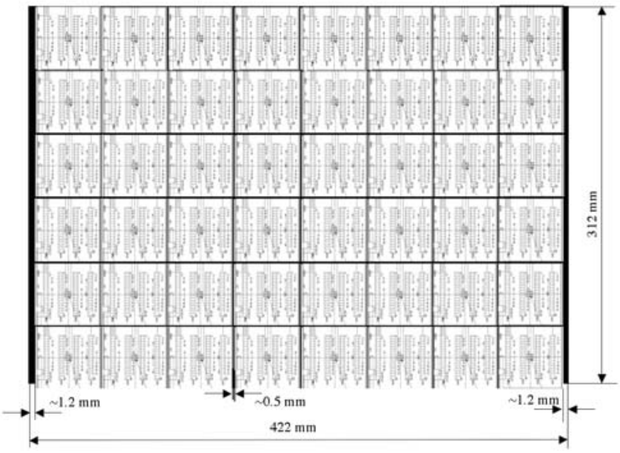

Figure 1.23: Detector matrix on one FDIRC detector camera with 48 H-8500 MaPMTs. The entire FDIRC system needs 576 tubes and 18,432 pixels [5].

Modularity: photodetector mechanical packing fraction There are two factors to consider when determining the photon coverage: (a) detection coverage in the focal plane of the photon camera, and (b) coverage within each tube (we will consider detection losses within the dynode structure later and loss factors later). Figure 1.23 shows the H-8500 matrix of 48 tubes in one photon camera. The size of each H-8500 tube is 52.0 ± 0.3 mm, and a gap between each tube is ∼0.5 mm; this gives a contribution to the packing fraction of ∼98.6%. The photon packing density (effective area/external size) within each tube is ∼89%. These factors give the overall photon packing efficiency of ∼88% for the photon camera based on 48 H-8500 tubes.

Photon detector mechanical support Photon detectors will be supported by the electronics motherboard. The original scheme to have one large motherboard for all 48 detectors was considered as too difficult to implement in practice. Instead, we will use smaller motherboards supporting groups of 6 detectors running in vertical direction. **[yet to be written]**

Optical coupling of detectors to FBLOCK The MC simulation shows (see Fig. 1.24) that we loose 8-25% of photons if we do not optically couple PMTs to the FBLOCK [13]. The event Cherenkov angle resolution ($\sigma \sim 2.94$ mrad) improves by ∼10% with optical coupling [13]. On the other hand, an access to a single failed detector will become complicated, and we may have to abandon a concept of one large single motherboard. If we use the optical coupling, we are considering eight vertical segments, each handling six detectors; each segment could be removable by sliding it vertically off the FBLOCK. In addition, we have not yet selected the optical coupling grease. One should realize that any leak of the grease on the FBLOCK side optical surfaces, would result in a serious loss of photoelectrons. The optical coupling concept has yet to be tested to investigate its practicality, reliability and radiation hardness, and therefore it remains an open issue.

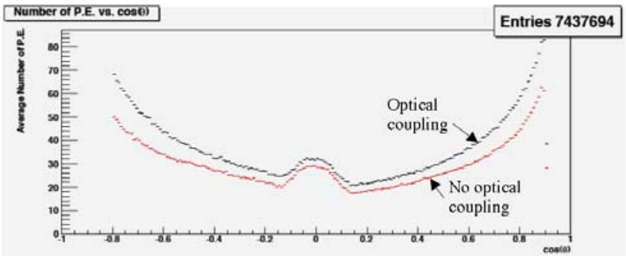

Figure 1.24: Simulated (Geant4 MC) number of detected photoelectrons as a function of the polar angle for two cases: with and without optical coupling between detector face and the FBLOCK [13].

Temperature requirements in Fbox enclosure There are two major sources of heat in the detector enclosure: (a) HV resistor dividers, and (b) electronics. Each tube has a HV divider. All dividers together draw ∼9 W per 48 tubes, which is a trivial amount of heat. Assuming for now that the electronics will dissipate ∼10 W per package, one gets a total amount of heat of ~500 W per 48 detectors. We will need a water-cooled heat exchanger.

Another worry is what happens if we loose cooling. Based on tests with the FDIRC prototype detector enclosure, the temperature would rapidly climb beyond ~80°C. That would be dangerous for tubes, optical grease coupling, glues and that could also create mechanical stresses. Therefore we need an automatic power shutoff system.

Rates and aging issues in H-8500 PMTs One strong point of our design is that we share a total photon background load from a single bar box among 48 H-8500 detectors, and this results in acceptable rate even at the highest luminosity, and an acceptable total charge load after 10 years of operation.

We use two methods to estimate FDIRC rates: (a) empirical scaling (ES) from Belle-I Aerogel counter rates and assuming that the background rate scales as the luminosity (we use Belle-I rates rather than *BABAR* rates because that machine is believed to be closer to the Super$B$ for the background scaling). (b) We then use the MC simulation, which simulates all physics background processes involved in the background production and includes the precise modeling of beam line magnet components all the way up to 16 meters from IP in either direction, and uses correct FDIRC geometry with a proper handling of optical photons. The MC simulation shows that the rate is dominated by the radiative Bhabha scattering (thus, our assumption above that the background scales as the luminosity is justified). The ES method is rather close to the MC prediction (MC) for the contribution from the active detector volume without shielding: 75 kHz (ES) vs. 120 kHz (MC) per double-pixel, or 2.4 MHz (ES) vs. 3.8 MHz (MC) per tube, which would correspond to the total accumulated charge of 1.2 C/cm^2 (ES) vs. 2.3 C/cm^2 (MC) for a total integrated luminosity of L_{int} ~75 ab^{-1}. However, the contribution from the photon camera, which is outside of the magnet, would be much higher without a shielding: 120 kHz (ES) vs. 550 kHz (MC) per double-pixel. The dominating background is due to the Bhabha scattering, the Touschek effect's contribution is less than 10%.

Given the design of the H-8500 dynode structure, which prevents the direct ion backflow to the photocathode, we expect the MaPMT tube cathode-aging rate to be similar to an usual PMT aging behavior, which means that the above numbers appear to be safe. For example, *BABAR* DIRC PMTs accumulated at least ~150 C per tube during ~10 years of *BABAR* operation and tubes have lost some efficiency (~30%), but operated well until the end with a few voltage adjustments to correct the gain loss. This tells us that our nominal starting voltage should not exceed ~1.05 kV to allow possible later gain adjustments. One should, however point out that aging tests are yet to be done for the H-8500 tube. One should also worry about unusual background conditions caused by the machine misbehavior, changes in tune, beam losses, etc., especially in the early periods before reaching the full luminosity. Hamamatsu recommends that the absolute maximum current be ~100μA per tube or ~2μA per pixel. Another constraint is the capability of the electronics to cope with high rates. Super$B$ FDIRC electronics can handle rates up to ~20 MHz per pixel, if one pixel is firing, and up to ~2.5 MHz per tube if all pixels are firing. [**We still need to add a total number of neutrons per cm^2 per year, rate of slow protons from np collisions, rate of ions, and expected dose obtained by electronics. All this after the background shielding and magnetic shielding are added correctly**]

Figure 1.26 shows the Hamamatsu aging data for R8400-00-M64 MaPMT running at 100μA for 10,000 hours. There is no obvious large effect which could not be corrected by a voltage adjustment. Translating this to our expected conditions, and assuming that H-8500 behaves the same way as R-8400 tube, the maximum expected anode current is approximately 500 kHz/double-pixel × 32 channels/pmt × gain × electron charge = $500\times10^3\times32\times2\times10^6\times 1.6\,10^{-19}$~5$\mu$A, which is only ~2× smaller than

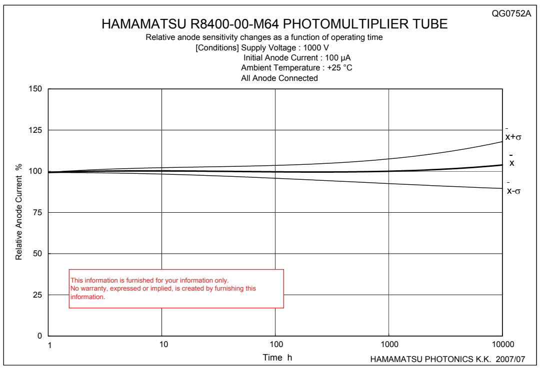

Figure 1.26: Hamamatsu data for R8400-00-M64 MaPMT showing that there is no large drop in photo-current when running 100μA for 10,000 hours (~400 days).

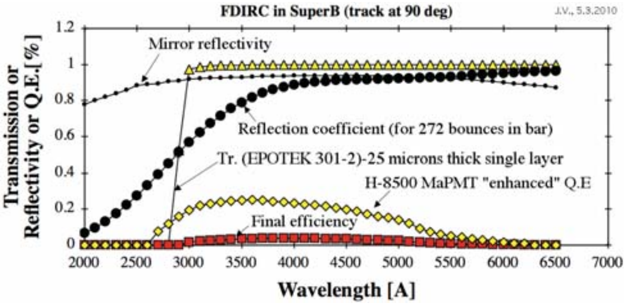

Figure 1.28: FDIRC wavelength response is limited on low wavelength side by EPOTEK 301-2 glue used to glue bars together [5].

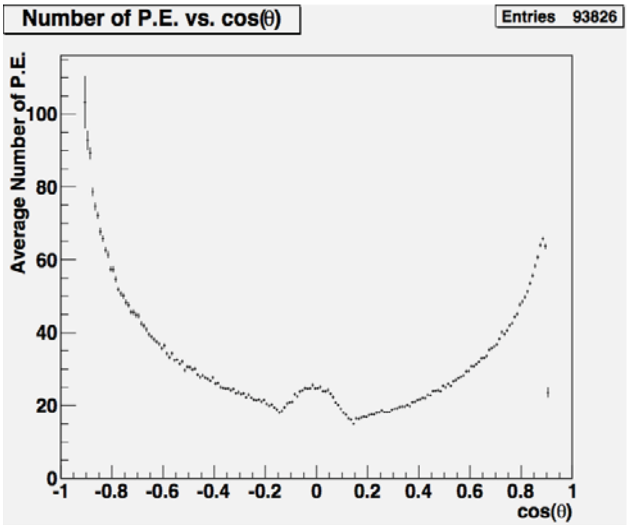

Figure 1.27: MC simulation of number of photoelectrons in FDIRC [13].

Hamamatsu's safe limit from their aging test, if one runs with this rate for 10 years.

Therefore we do need to shield the FBLOCK's contribution to the overall rate, and keep only a contribution from the active region of bar boxes. The present MC background simulation estimate is (a) ~50 kHz/double-pixel as contribution from bar boxes in active region with shielding and ~120 kHz/double-pixel without shielding, and (b) ~60 kHz/double-pixel from FBLOCK with shielding and ~550 kHz/double-pixel without shielding. Table 1.25 summarizes rates under various conditions. Figure 1.52 shows the FDIRC shielding design.

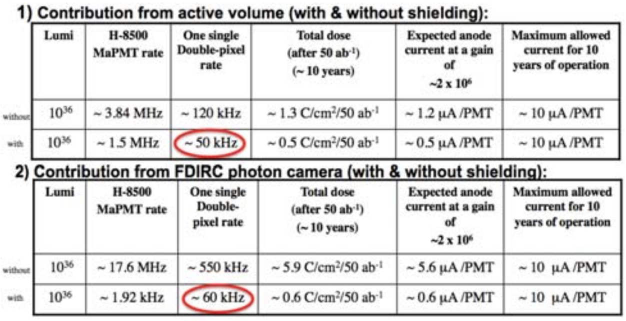

1) Contribution from active volume (with & without shielding):

	Lumi	H-8500 MaPMT rate	One single Double-pixel rate	Total dose (after 50 ab^{-1}) (~ 10 years)	Expected anode current at a gain of ~2 x 10^6	Maximum allowed current for 10 years of operation
without	10^{36}	~ 3.84 MHz	~ 120 kHz	~ 1.3 C/cm^2/50 ab^{-1}	~ 1.2 µA /PMT	~ 10 µA /PMT
with	10^{36}	~ 1.5 MHz	~ 50 kHz	~ 0.5 C/cm^2/50 ab^{-1}	~ 0.5 µA /PMT	~ 10 µA /PMT

2) Contribution from FDIRC photon camera (with & without shielding):

	Lumi	H-8500 MaPMT rate	One single Double-pixel rate	Total dose (after 50 ab^{-1}) (~ 10 years)	Expected anode current at a gain of ~2 x 10^6	Maximum allowed current for 10 years of operation
without	10^{36}	~ 17.6 MHz	~ 550 kHz	~ 5.9 C/cm^2/50 ab^{-1}	~ 5.6 µA /PMT	~ 10 µA /PMT
with	10^{36}	~ 1.92 kHz	~ 60 kHz	~ 0.6 C/cm^2/50 ab^{-1}	~ 0.6 µA /PMT	~ 10 µA /PMT

Figure 1.25: FDIRC pixel rates with and without shielding.

Magnetic shield of H-8500 PMTs For *BABAR* DIRC PMTs, which have a classical PMT dynode design, it was necessary to keep the magnetic field below ~1 Gauss in the SOB to prevent a serious degradation of pulse height spectra [4]. To do that, it was necessary to enclose the entire photon camera into a large magnetic shield. Figure 1.27 shows the effect of the magnetic field on the H-8500 tube pulse height. One can notice that the effect is different near the tube boundary compared to its central region. We conclude that we can tolerate a resid-

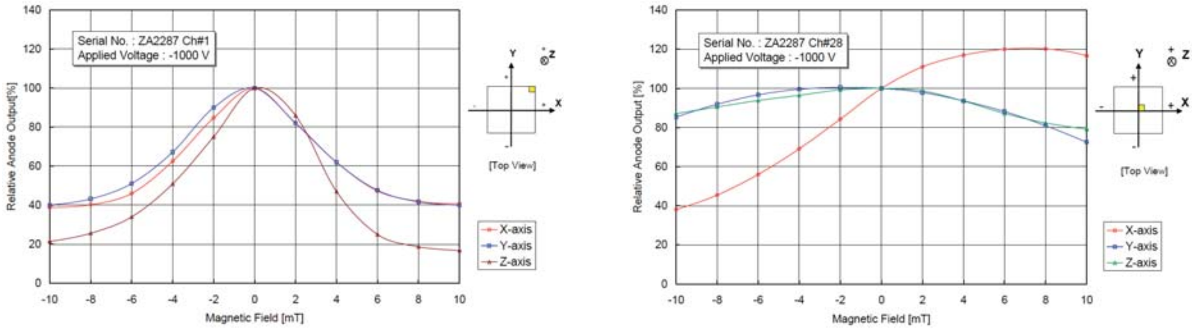

(a) The effect on boundary pixels.

(b) The effect on pixels near center.

Figure 1.27: Magnetic field effect on the H-8500 MaPMT's pulse height (Hamamatsu data).

ual magnetic field up to a level of a few Gauss with no effect on the pulse height. We plan to use a magnetic shield similar to that of *BABAR*.

Prediction of number of photoelectrons per ring Figure 1.28 shows FDIRC's wavelength bandwidth [5]. One can see that we operate in the visible wavelength region and that the effective filter is the Epotek 301-2 epoxy. Assuming a peak QE of 24%, and no optical grease coupling between PMTs and the FBLOCK, one obtains ~32 photoelectrons for tracks with $\theta_{\rm dip} = 90^\circ$ using a simple spreadsheet calculation. Figure 1.29 shows the MC simulation of number of photoelectrons as a function of the dip angle [13]. At $\theta_{dip} = 90^\circ$ it predicts ~27 photoelectrons. We find the FDIRC performance slightly better than the DIRC performance in *BABAR* [4]. **[numbers are still being checked]**

Radiation damage of optical components We used the ^{60}Co source for the irradiation of the glue samples. First, we have investigated the radiation damage of Corning 7980 Fused Silica 3 mm-thick coupons used for support of glue samples and, as expected, found no loss of transmission up to 250 krad. Figure 1.30 shows the irradiation of the Epotek 301-2 epoxy, used for coupling of the new Wedge to the bar box window, and the Shin-Etsu 403 RTV, used for coupling of the FBLOCK and the new Wedge. We show that these glues are acceptable for the Super$B$ conditions, although the Epotek 301-2 does see some small loss of transmission [25].

1.4.3 Laser calibration system

Optics of calibration The aim of this calibration is twofold: (a) check the operation of tubes and electronics, (b) provide pixel offset constants for FDIRC timing calibration, which was found to be useful in the first FDIRC prototype doing the chromatic corrections [21]. Figure 1.31 shows the laser entry into the FBLOCK as implemented in the final FDIRC prototype. The fiber plugs into a connector with a lens (F230FC-A), which makes a parallel laser beam, which then strikes a 5 mm diameter Opal diffuser, which was selected out of several choices for it uniform light diffusing effect. The small diameter diffuser is necessary to limit losses of real Cherenkov photons. We found experimentally that the best arrangement is if the diffuser is pressing against the bottom surface of the FBLOCK with the help of a spring (no gluing as it affects a uniformity of the scattered light). There is one fiber entry per photon camera serving one bar box. Figure 1.32 shows a MC simulation indicating that the total time spread across the focal plane is about 2 ns, which will have to be corrected out to get a single t_0. It also shows an example of MC simulation of the photon time of arrival in a single pixel. It shows multiple peaks corresponding to direct light and various FBLOCK side reflections. We believe that we will be able to determine timing offsets with enough precision using selected significant

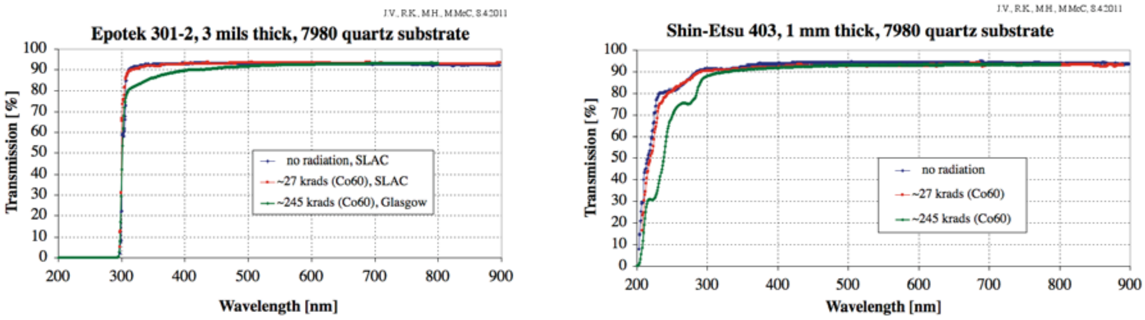

(a) Transmission of Epotek 301-2 epoxy (50-75 microns thick).

(b) Transmission of Shin-Etsu 403 RTV (1 mm thick).

Figure 1.30: Radiation damage by the ^{60}Co source of glues used in the construction of the photon camera [25].

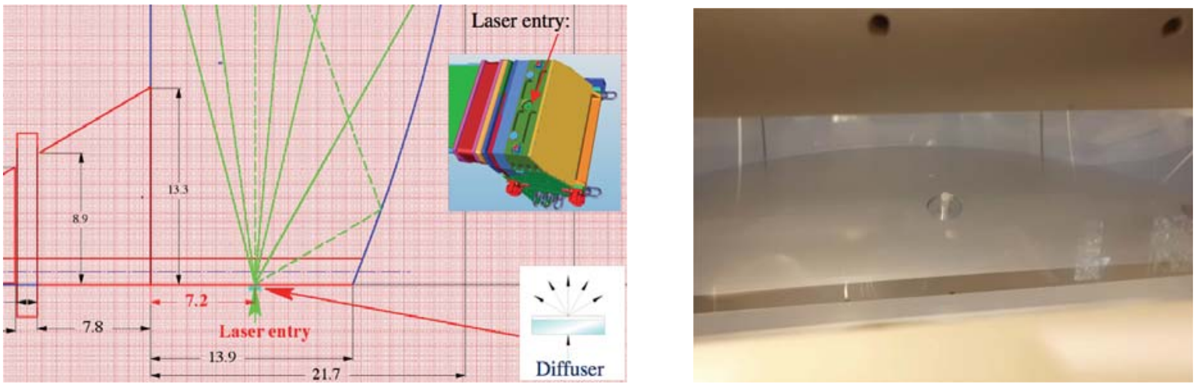

(a) Optical details of laser entry [21].

(b) OPAL diffuser used to spray laser photons into the FBLOCK.

Figure 1.31: Laser entry into the FBLOCK.

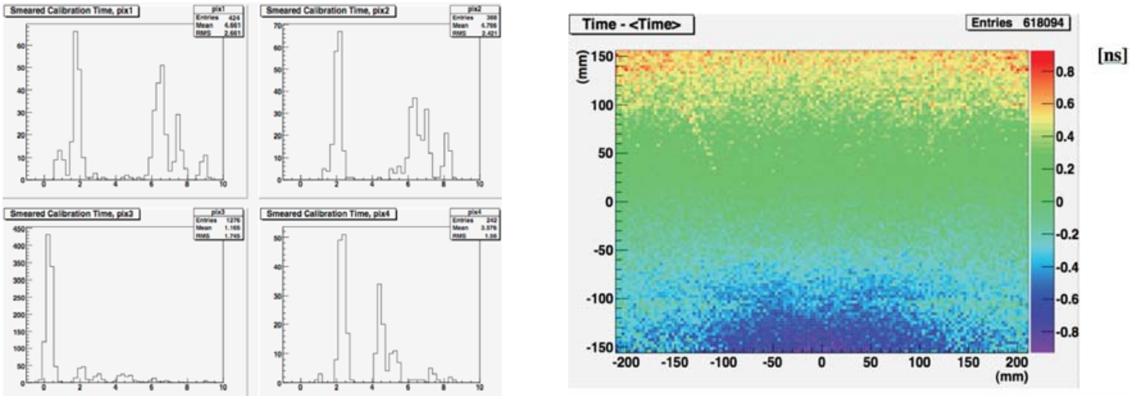

(a) Time peaks from the laser calibration as it appears in several pixels [13].

(b) Laser time spread is a few ns across the focal plane [13].

Figure 1.32: Laser calibration timing.

peaks. This calibration scheme is going to be tested in the final FDIRC prototype.

Laser and fiber optics choice We will use the Pilas laser diode providing a light with 407 nm. We would like to split the light from one Pilas source into 6 branches, but the fiber splitter has yet to be tested to check that splitting is equal. If this works we will need two Pilas control units serving the entire system. The Pilas control unit can be triggered externally so we can control both the timing and when the calibration should happen.

1.4.4 FDIRC Mechanical Design

Description of BABAR bars, bar boxes We will reuse bar boxes from the *BABAR* DIRC. Bar boxes will not be modified as it is considered too difficult to do. This has some disadvantages, for example, the old wedge, with its 6 mrad angle at the bottom surface, somewhat worsens the new camera optics by adding ∼0.5 mrad to the Cherenkov angle resolution. Another potential problem is that the glue has sees ∼10 years of radiation during the *BABAR* experiment. Extensive studies were performed with the *BABAR* di-muon data and no detrimental effect was found on the glue transmission [26]. However, we do need to be extra careful when transporting bar boxes, as it is not known if the Epotek 301-2 glue strength was not affected, and some tests will be required.

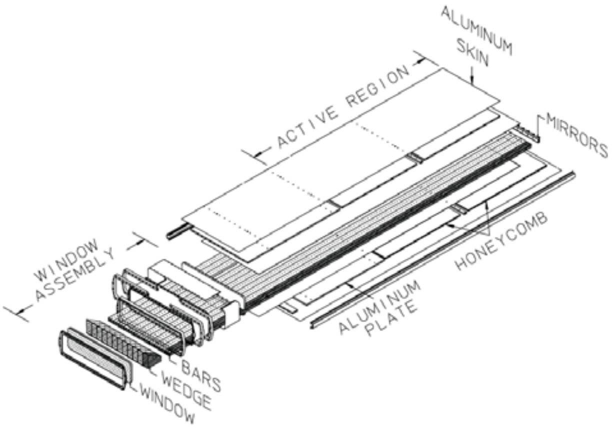

Figure 1.33: *BABAR* DIRC bar box [4].

Figure 1.33 shows the *BABAR* DIRC bar box with its 12 Fused silica bars, each glued out of 4 bar segments 122 cm long [4]. Figure 1.34 shows the nominal dimensions of each bar including the wedge. In reality it is somewhat more complicated, as bar dimensions vary and each bar box is slightly different. This has been recorded in spreadsheets [27]. Figure 1.35 shows the cross-section of a bar box containing 12 fused silica bars. Figure 1.36 shows the bar end with a mirror. There are altogether 12 bar boxes and 144 full-length bars in the entire system.

Fused silica optics: New Wedge and FBLOCK The new Wedge and the FBLOCK

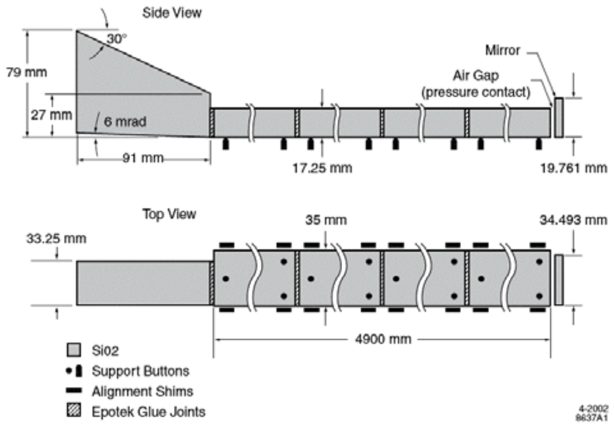

Figure 1.34: One bar segment with nominal dimensions [4].

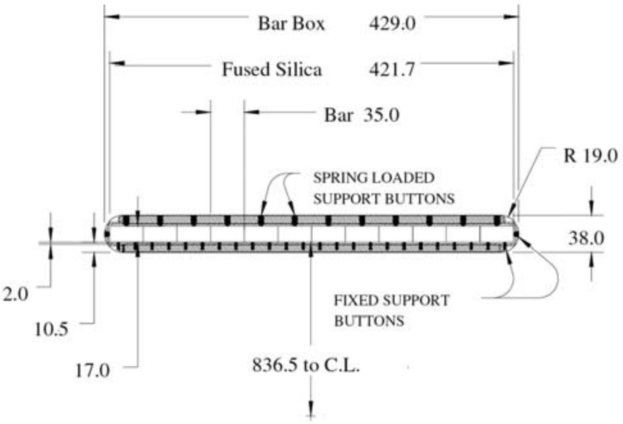

Figure 1.35: A cross-section of bar box with 12 bars [4].

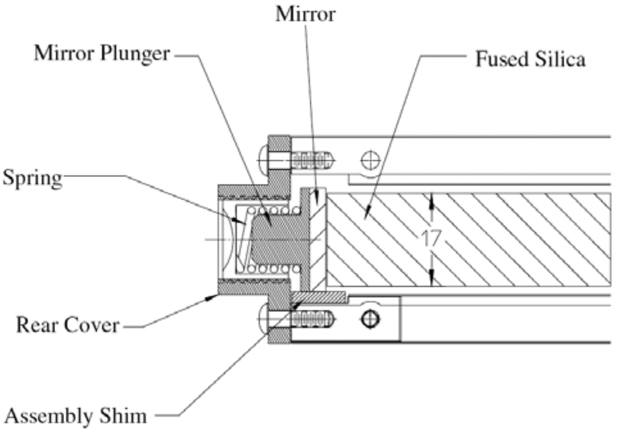

Figure 1.36: Bar end with a mirror [4].

are made of radiation hard Fused silica Corning 7980. Corning Co. makes fused silica 7980 material in a form of boules of up to 60" diameter – see Fig. 1.37. The striae are running typically perpendicular to axis of a 60 inch dia. boule. The best homogeneity of the refraction index dn/n is along the axis of the boule. There are two types of 7980 material: (a) standard (characterized much less and therefore should be checked more), and (b) so called KrF (very characterized material; Corning qualifies striae with an optical interferometer; to get this data we will have to sign a non-disclosure agreement). We chose the "standard" material, as the cost of the KrF material is about 2-3 times higher. For the standard fused silica material these are typical specifications: (a) dn/n is less than 1 ppm over the scale of a mm. (b) The bottom-to-top of the boule along the axis: dn/n less than 5 ppm at 200 nm and better at longer wavelengths. c) dn/n is about 5-7 ppm in the direction perpendicular to the bull axis. Part-to-part variation is expected at a level of dn/n ∼20 ppm in the visible wavelength range. One should avoid the very bottom and top of the boule as there could be larger stria. To avoid it one should buy thicker boule, and this issue should be remembered for the final production. We visited the company and tested the material for stria with a laser. None was detected. Out of one boule one expects to make three blocks such as shown in Fig. 1.38. One has to pay attention to orientation of the FBLOCK within the raw block. The back side of the FBLOCK needs to be at the bottom of the boule as there is more possible contamination from sand used as a seed of fused silica material deposition.

The manufacturing was then split into three steps done in three different companies: (a) grinding final shapes about 1-2 mm oversized, (b) polishing to final size and surface polish of better than 30 Å rms, (c) coating two FBLOCK's reflecting surfaces with aluminum with SiO_2 overcoat to protect it, and (d) the final QC of finished pieces. Figure 1.39 shows the finished new Wedge and FBLOCK (before the two mirror plating step). These optical pieces were successfully produced, which demonstrates

Figure 1.37: An example of the fused silica 7980 material in the form of a 60 inch dia. boule made by Corning.

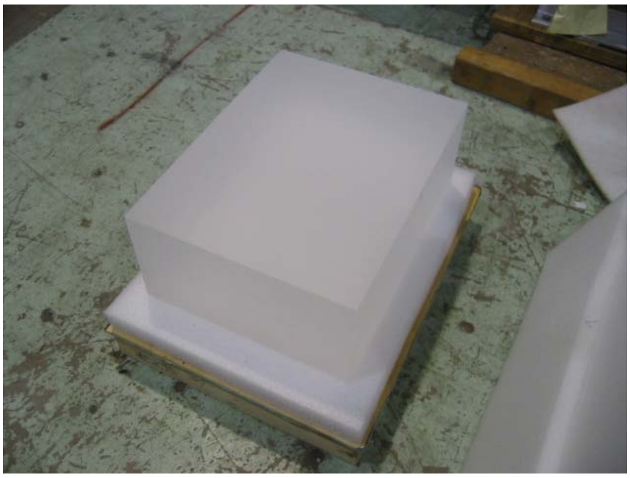

Figure 1.38: The fused silica 7980 material in a form of block ready for machining.

that the new camera optics is doable. However, there is a number of critical steps where error can be made, for example: (a) damages when handling, (b) surface pollution either before plating or in a final assembly, c) stria problem needs to be checked, (d) accidental swaps of correct and wrong materials, etc.

FBLOCK mirror surfaces It is absolute mandatory to have a very good surface cleanliness before the aluminum plating is attempted. Any contamination will result in peeling problems. FBLOCK's two aluminum plated mirror surfaces are protected by a SiO_2 layer. Even though there is the protection layer, mirror surface are still fragile, especially if the surface is polluted during handling.

Another complicated issue is the FBLOCK shipping from the polishing company to the laboratory where it will be used. The FBLOCK is very heavy and its polished surfaces and two mirrored sides can be easily damaged by a rubbing motion created by shipping. Surfaces have to be protected by a plastic film during the shipment, but the film must not stick to mirror surface to cause peeling problems. Based on our tests, we have decided to use the Grafix plastic vinyl film in future, which adheres to surfaces via electrostatic forces, does not remove plated layer and does not leave a surface pollution, which would be difficult to clean.

Gluing the new Wedge to the Bar Box Window This optical coupling of Wedge to bar box window is done in the clean room. Figure 1.40 shows a detail of coupling of the new Wedge to the bar box. The coupling is done with the Epotek 301-2 optical epoxy of 25-50 micron thickness. The bottom of the new Wedge is aligned to the bottom bar surface, i.e., not to the old wedge as it has a ∼6 mrad angle. The new Wedge is centered left-right in the bar box window. This coupling is not possible to remove in the future as one would risk damaging the bar box.

Gluing FBLOCK to Wedge The optical coupling between the new Wedge and the FBLOCK is done in situ, and, in principle, it is removable. We set the gap between the new Wedge and the FBLOCK to 1 mm, and fill it with Shin-Etsu 403 RTV. In case of some problem with Fbox, one can first separate the two pieces using a thin razor wire, then clean the surfaces and finally couple again the two surfaces. The penalty for this option is that an RTV joint is not as strong as an epoxy joint. The breaking force of this RTV coupling was measured to be ∼520 kg using glass windows of the correct size (we have not done with a quartz material); it was found

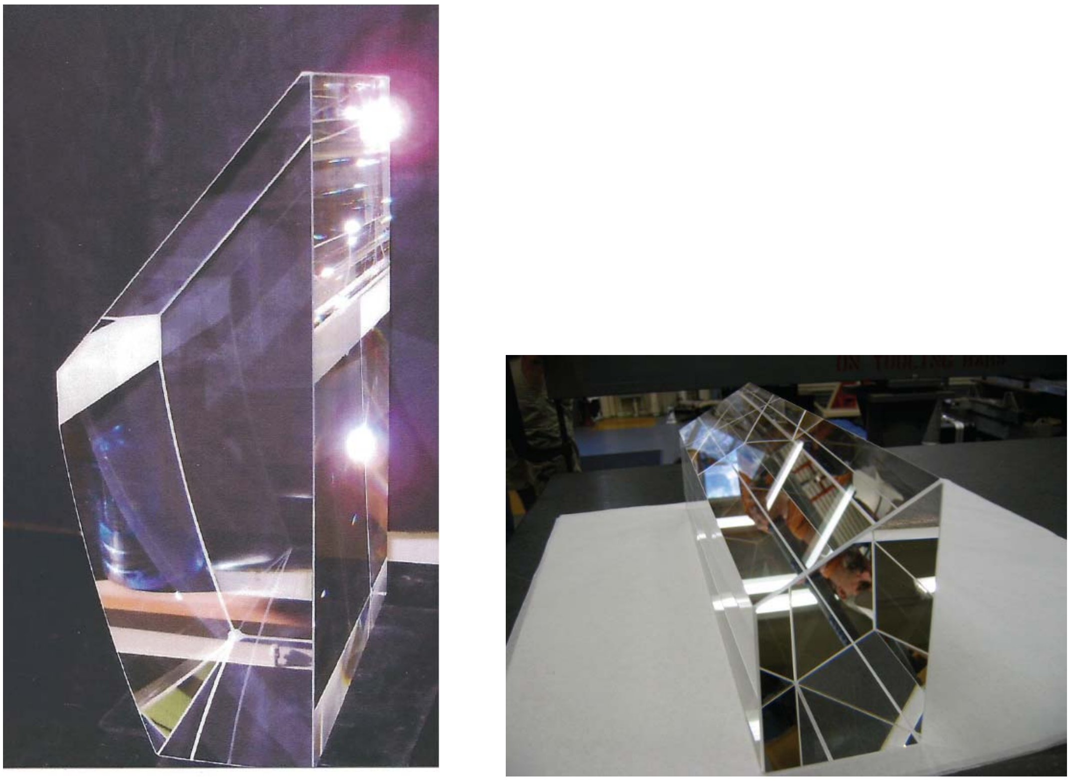

(a) FBLOCK after polishing but before plating.

(b) New Wedge after polishing.

Figure 1.39: New photon camera parts: New Wedge and FBLOCK.

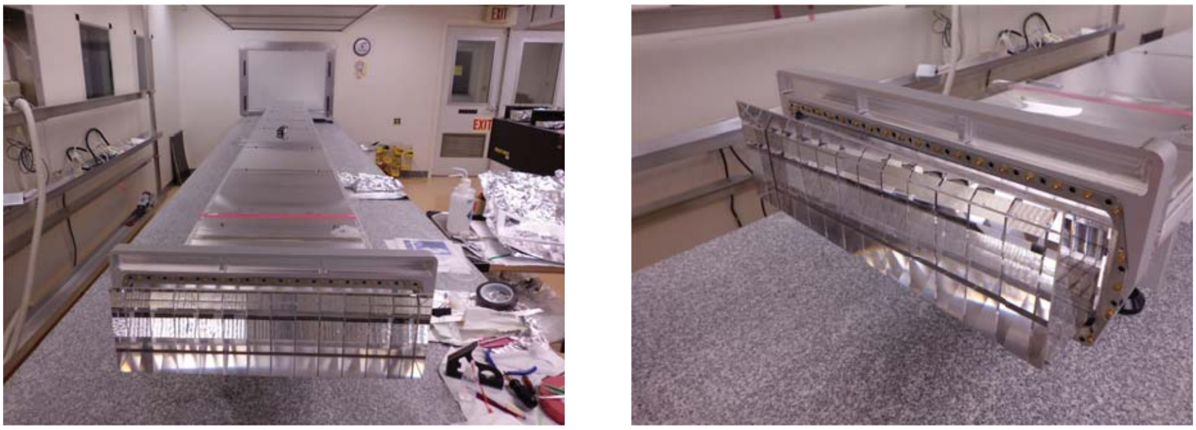

(a) The bar box with the new Wedge in the clean room.

(b) Detailed view of the new Wedge and the bar box window.

Figure 1.40: Coupling of the new Wedge to the bar box.

that this value depends strongly on the glass cleaning procedure. See Figure 1.47 and chapter "Support of Fbox in the Super$B$ magnet" for more details on the installation procedure.

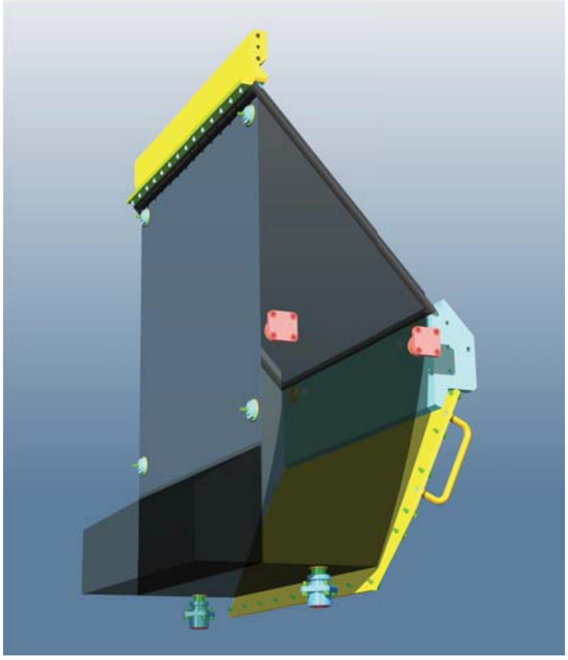

Figure 1.43: FBLOCK support buttons (small buttons are fixed, larger ones, two from the bottom and two from one side, are adjustable to keep FBLOCK stable even if Fbox, made of aluminum, expands due to thermal effects).

Fbox: Mechanical support of FBLOCK Figure 1.41 shows Fbox enclosure of the optics. Figures 1.42 and 1.43 show details of how FBLOCK is supported by plastic buttons. Plastic buttons, made of PET (polyethylene terephthalate) plastic, prevent FBLOCK optical surfaces from touching the aluminum surface of Fbox. Some buttons are fixed and some are spring-loaded. The spring loading is made using a stack of 8 belleville washers, which is the most compact way to produce predictable force. They are set to offset the total weight of FBLOCK and to take into account thermal effects. Placing the FBLOCK into the Fbox requires a very careful procedure as it is very heavy (~80 kg) and easy to be damaged. It was very useful to work out a step-by-step procedure [28] with a dummy plastic FBLOCK [29]. At the time of TDR writing, however, we already have the experience of putting together the real photon camera with the Fused Silica FBLOCK. Figure 1.44(a) shows the first step of Fbox assembly where we placed the FBLOCK on four plastic support buttons. We have chosen a four-point support rather than a three-point one because it was judged to be easier to place the FBLOCK on the Fbox base plate, which is actually a very tricky operation. The front mirror surface is protected by four quartz coupons about 1.5 mm-thick, glued to the flat mirror surface by Epotek 301-2 epoxy. These four coupons are then touching plastic buttons located in the Fbox. The idea is that a rubbing motion due to thermal effects will be better dealt with if plastic buttons slide on quartz coupons rather than on the mirror plating directly. Figure 1.44(b) shows a fully assembled Fbox with the real Fused Silica FBLOCK.

The Fbox and bar box have to be optically coupled. Figure 1.45 shows an example how this is done in the CRT setup.

Protection of optical surfaces As one deals with internal reflections, all optical surfaces have to be very clean, and therefore every part of the Fbox was very carefully cleaned before a final assembly to prevent outgassing. In addition, optical surfaces are protected against the environmental pollution and the moisture condensation by flowing a boil-off N_2 through the sealed Fbox. Fbox is sealed with a combination of Viton flat gaskets, Viton O-ring and the Gore gasket tape (near the detector area), and in some difficult sections simply with DP-190 glue. Based on experience in *BABAR* each bar box requires a flow of about 100 cc/min.

Bar box storage at SLAC Figure 1.46 shows present storage of 12 bar boxes. They are supported on pre-aligned shelves to prevent mechanical stresses due to support distortions. They are under a constant flow of the boil-off N_2 and thermally insulated. The storage box is kept at a nominal temperature of 18°C. In

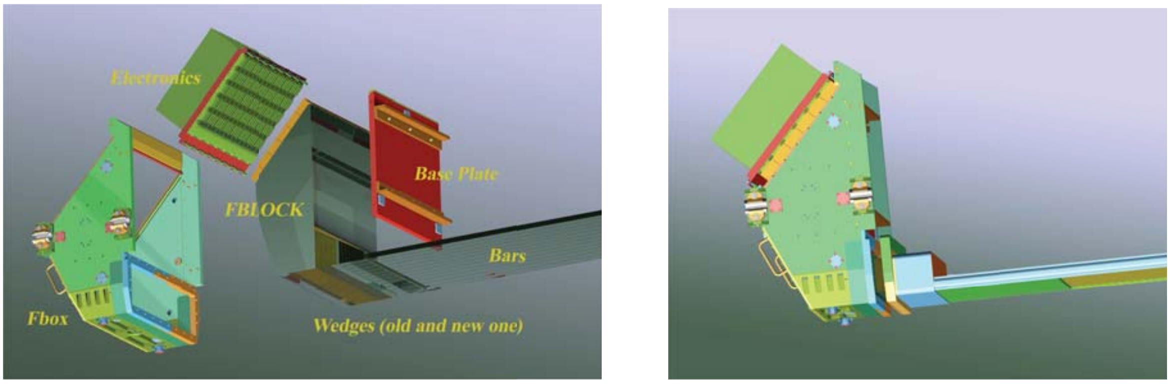

(a) Various components for the optics enclosure.

(b) Complete Fbox enclosure, including bar box.

Figure 1.41: Fbox enclosure of FBLOCK optics, including wedges, bars, detectors and electronics.

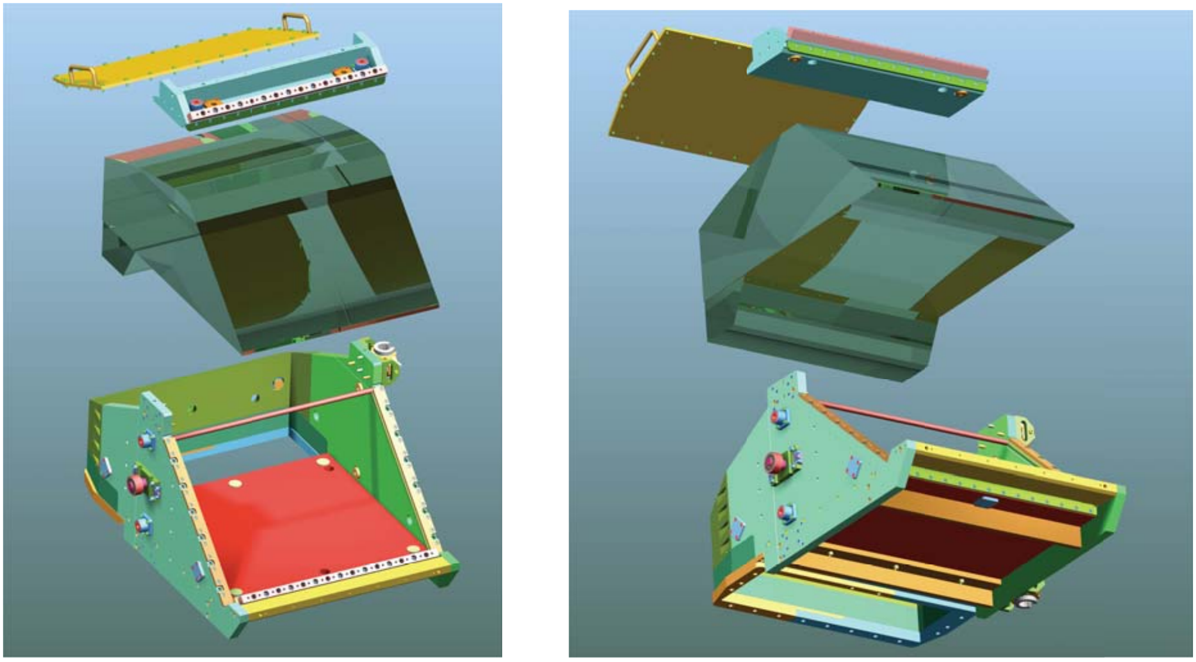

(a) Top view.

(b) Bottoms view.

Figure 1.42: Button support of FBLOCK optics in Fbox.

(a) FBLOCK placed on the base plate of Fbox.

(b) Assembled Fbox in front of bar box.

Figure 1.44: Fbox assembly around the real Fused Silica FBLOCK.

(a) Fbox and bar box in the CRT setup.

(b) Details of coupling of new Wedge to FBLOCK.

Figure 1.45: Fbox coupling to bar box in the CRT setup.

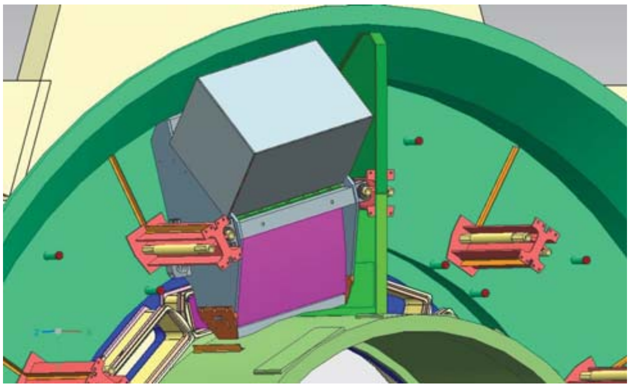

Figure 1.48: Finished installation of the camera.

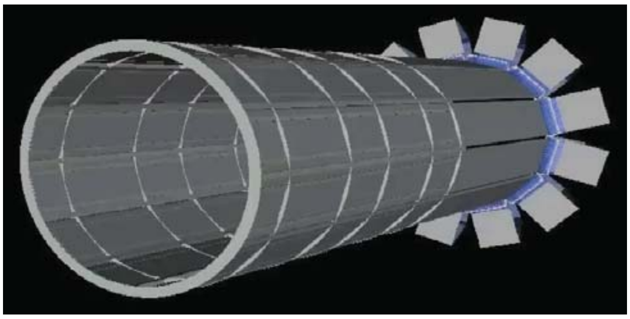

Figure 1.49: Overall view of the FDIRC layout with 12 bar boxes and 12 photon cameras.

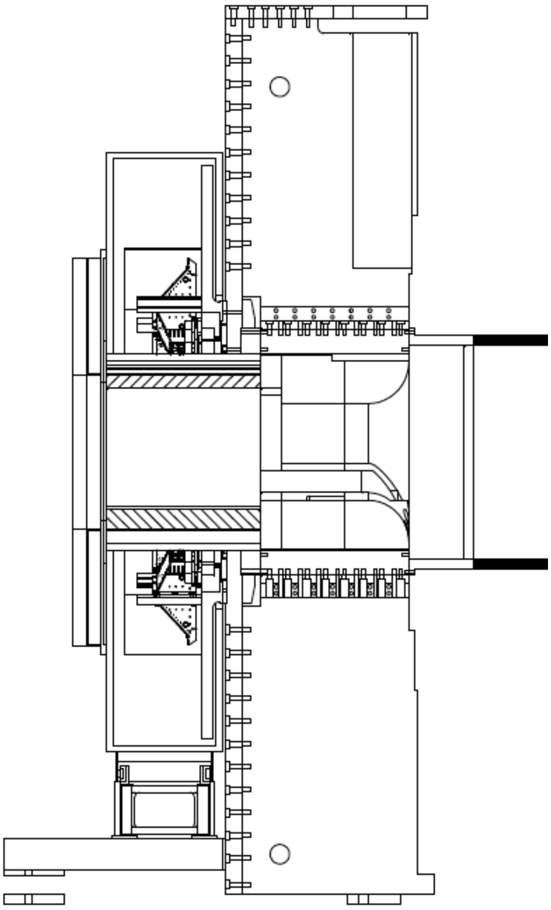

Figure 1.51: Side view of the FDIRC showing magnetic and background shields, and rails on which they move.

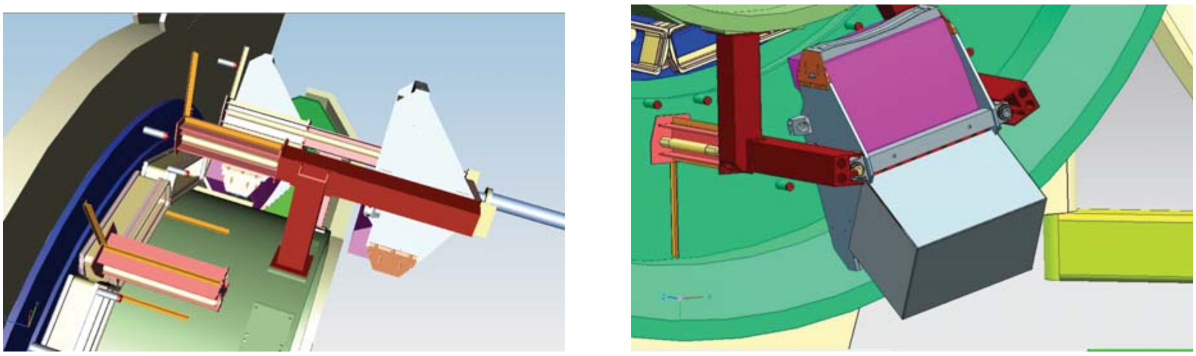

(a) Fbox installation fixture for position pointing up.

(b) Fbox installation fixture for position pointing down.

Figure 1.47: Fbox installation in the Super$B$ magnet.

addition, there is no light to prevent yellowing of the Epotek 301-2 glue, an important issue to consider in future.

Figure 1.46: Bar box storage at SLAC.

Support of Fbox in the SuperB magnet The plan is to install bar boxes with Wedge already glued to the bar box windows. The Fbox will be installed in situ. Figure 1.47 shows the procedure. The bar box has to be moved beyond the neighboring already installed Fbox, so one has enough room for gluing. With a temporary rail support it is possible to bring the Fbox close to the bar box so that the Wedge and the FBLOCK surfaces are parallel and the gap is set to 1 mm, bottom surfaces of FBLOCK and the new Wedge are aligned, and both are centered left-right. The gap between FBLOCK and the new Wedge is then filled with the Shin-Etsu 403 RTV. Once the RTV is cured, the gas sealing is made, the Fbox is pushed on the rail to its final position, and the earthquake bracing is installed. The temporary rail support is then removed. Figure 1.48 shows the finished installation.

Figure 1.49 shows the overall FDIRC detector schematic layout with its 12 bar boxes, and the 12 corresponding photon cameras. Figures 1.50 and 1.51 show overall mechanical views of the FDIRC in the Super$B$ experiment.

Background shielding to protect electronics & detectors We need background shielding to (a) reduce the contribution to the rate from the FBLOCK, which is located outside of the magnet, and (b) to reduce effect of radiation to detectors and electronics. Based on simulations, the dominant background in FDIRC is due to Radiative Bhabha scattering. The resulting background is mainly gammas, electrons, positrons and neutrons. The background estimate of the photoelectron rate without shielding is 120 kHz/double-pixel coming from the active region of bar boxes within the magnet, and 550 kHz/double-pixel coming from the FBLOCK section located outside the magnet. To reduce this rate, it is essential to provide a shield of the FBLOCK outside of the magnet. To design the shielding, two main con-

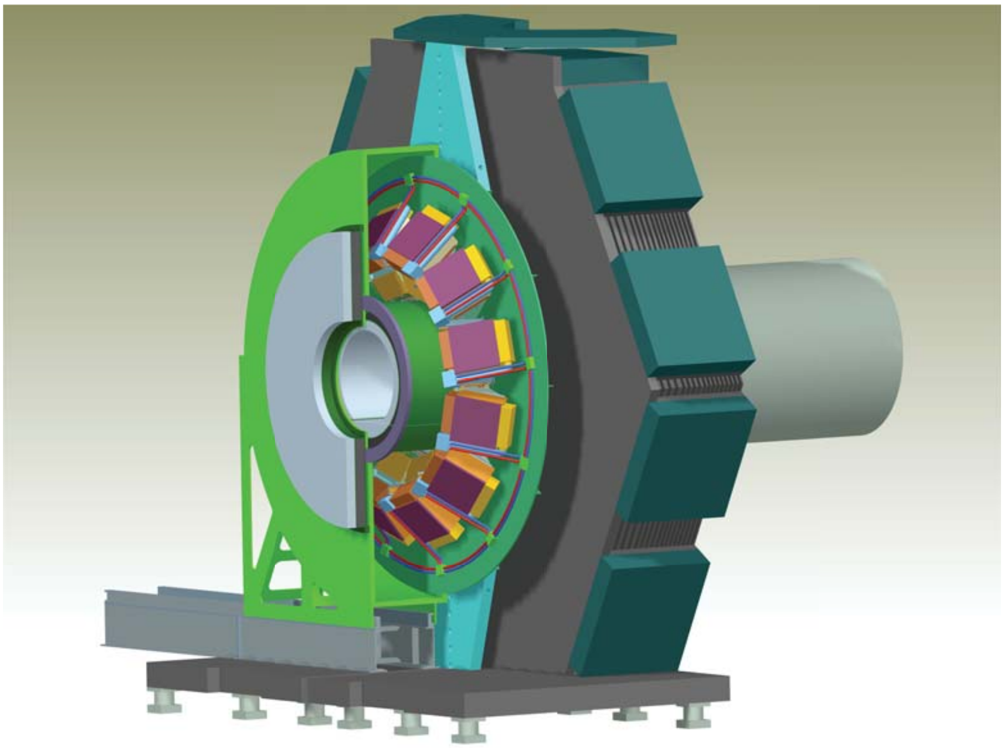

(a) A 3D view showing the new magnetic shield and background shields, and Fboxes.

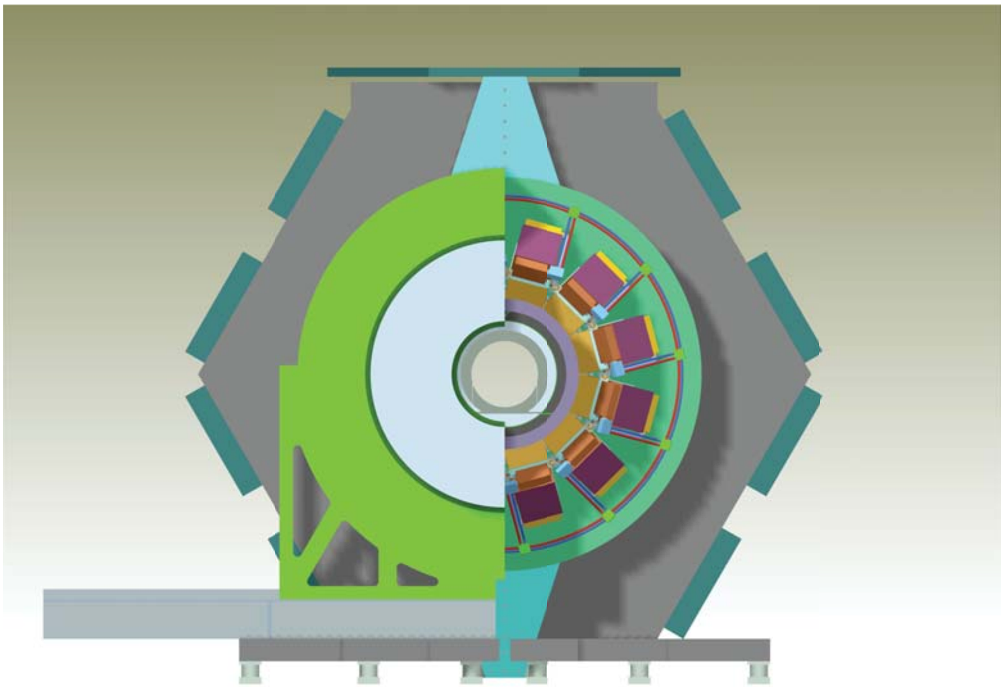

(b) Front view showing six Fboxes, the rest is hidden behind magnetic and background shields.

Figure 1.50: FDIRC in the magnet.

straints have to be taken into account: first, to allow an easy access to detectors and electronics, and then to minimize the overall weight of the shielding. Figure 1.52 shows the present concept of the FBLOCK shielding. It consists of 10 cm of Boron-loaded polyethylene layer sitting on 10-15 cm lead-steel sandwich, both located on inner radius and front side of the FBLOCK with its detectors and electronics. The front section of the shielding is moving on the magnetic door allowing a quick access to electronics and detectors – see Figure 1.52. In addition, the beam pipe tungsten shielding was strengthened. After this shield was added into the MC simulation, the FBLOCK contribution was reduced to ∼60 kHz/double-pixel, thus making a total rate of ∼110 kHz/double-pixel, and total dose of neutrons in the electronics region was reduced to ??? n/cm^2/year.

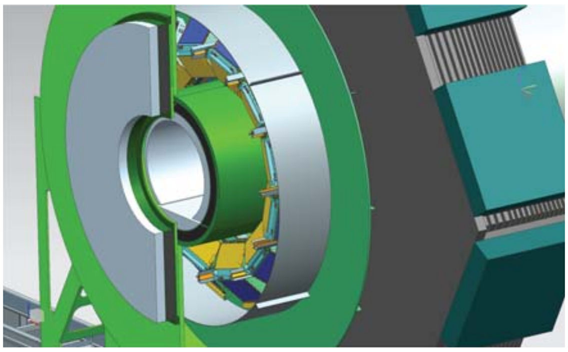

Figure 1.52: Details of local shielding around the FDIRC photon camera (a layer of 10 cm of Boron loaded polyethylene followed by 10-15 cm of lead-steel sandwich, located both on inner and front sides of the FBLOCK with its detectors and electronics).

Bar box shipment to Italy There are several issues to consider: (a) vibration and mechanical shocks, (b) thermal effects, (c) pressure changes, and (d) light exposure. Each bar box will have a container providing mechanical support and constant thermal environment. The vibrations and mechanical shocks will be mitigated by placing bar boxes on a precisely leveled support with a foam on top of it. The support structure will need telescopic mount to suppress large shocks. They will be thermally isolated and equipped with active thermal blankets to keep temperature constant. We will also provide a N_2 boil-off gas flow. Another important issue is pressure changes if air transport is used. The Hexel panels, used to construct bar boxes, do not have perforated walls, and therefore some stresses will be created. This has to be tested and carefully evaluated. Finally, bar boxes must not be left exposed to a strong light as one could yellow the Epotek 301-2 epoxy. [**To be finished or modified after we conclude all discussions**]

1.4.5 Electronics readout, High and Low voltage

The electronics for the FDIRC can be seen as an upgrade of the electronics of the *BABAR* DIRC. The new requirements of the experiment (trigger rate, background, radiation environment) and FDIRC specific requirements (resolution, number of channels and topology) have led to a similar but new design of the electronics chain.

The FDIRC electronics will handle 18,432 channels in total. The electronics chain is based on a high resolution and high count rate TDC, a time-associated charge measurement with 12 bit resolution, and an event data packing, sending data frames to the data acquisition system (DAQ). The target timing performance of the overall electronics chain is a time resolution of 100 ps rms. It has to deal with hit rate of 100 kHz per channel, a trigger rate up to 150 kHz, and a minimum spacing between triggers of about 50 ns.

The radiation level is expected to be less than 100 rads per year. The use of radiation tolerant components or off-the-shelve radiation-qualified components is mandatory. However, the expected energy of the particles may make the latch-up effect almost impossible. Thus, the design has only to take into account Single-Event-Upsets (SEUs). We selected the Actel family FPGA components for their non-volatile flash technology configuration memories, which are well-adapted to radiation environment.

Several architectures have been considered: (a) all electronics directly mounted on the FBLOCK, (b) all electronics mounted next to the detector and linked to PMTs by cables, and (c) a part of it on the detector (the Front-end boards) and the other part, called crate concentrator , situated close to the detector (this board is in charge of interfacing with the Front-end, reading out event data, packing and sending it to the DAQ).

The first solution has been chosen as baseline for the TDR for two main reasons: (a) The cost of cables (PMT to Front-end boards) is estimated to be close to 200 kEuros (1/3 of the price of the overall electronics cost), making this solution too expensive. Moreover, the possible option to have pre-amps on the PMT bases does not prevent from having electronics and power supplies on the detector. (b) The large amount of data per channel leads to have the L0 derandomizer and buffer on the Front-end boards. The FCTS receiver could be individually located on each Front end board but the number of cables needed pushes to distribute all the control signals on a backplane. Consequently the board dedicated to receiving and transmitting FCTS signals on the backplane naturally tends to also become the event data concentrator and the link to the DAQ. The baseline design assumes a 16-channel TDC ASIC, offering the required precision of 70 ps rms, embedding an analog pipeline in order to provide an amplitude measurement transmitted with the hit time. Thanks to a 12-bit ADC, the charge measurement will be used for electronics calibration, monitoring and survey purposes. The Front-end board FPGA synchronizes the process, associates the time and charge information and finally packs them into a data frame which is sent via the backplane to the FBLOCK control board (FBC). The FBC is in charge of distributing signals coming from the FCTS and the ECS, packing the data received from the FE boards to a n-event frame including control bits and transferring it to the DAQ.

The FDIRC electronics (Amp/TDC/ADC) An earlier version of the TDC chip, offering a similar resolution, has already been designed for the SuperNemo experiment. It provides a time measurement with both a high resolution (70 ps RMS) and a large dynamic range (53 bits). The architecture of this chip is based on the association of Delay Locked Loops (DLLs) with a digital counter, all of these components being synchronized to a 160 MHz external clock.

The Super*B* chip, called the SCATS, will keep the same philosophy but the high input rate requirement lead to a complete re-design of the readout part, in order to minimize the dead time per channel by increasing the data output speed. Instead of registers and multiplexer, which are the bottlenecks of the SuperNemo chip readout, it makes use of an individual FIFO memory per channel in order to derandomize the high frequency bursts of input data. With this architecture, data from the DLLs and the coarse counters are transferred into the FIFO memory within two 80 MHz clock cycles. When the transfer is complete, the channel is automatically reset and ready for the next hit. Simulations of the readout state machine showed an output FIFO data rate capability of 80 MHz. Time ranges for the DLLs and the coarse counter can be easily customized by adjusting the output data format (16, 32, 48 or 64 bits). Therefore, this chip is suitable for various applications with either high count rate and short integration time, or low count rate and long integration time. Figure 1.53 shows the block diagram of the Super*B* FDIRC TDC chip (SCATS).

A FIFO depth of 8 words (16 bits each) has been selected after simulation with a exponential distribution model of delta time between hits (mean rate $\sim$1 MHz) applied to inputs. To design this FIFO a full custom RAM has been developed. It permits reducing the size of the chip and consequently its cost. The chip is designed using known and proved mitigation techniques to face SEU issues due to the low-level radiation environment. The first version of the chip without the analog FIFO and the discriminator has been submitted in November 2011. We plan to submit by end 2012 one chip dedicated to the currently missing parts: (a) A

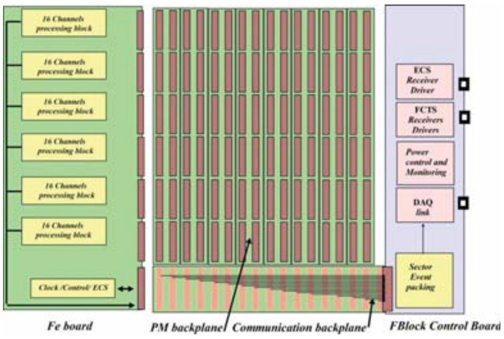

Figure 1.54: Front-end crate: PMT backplane, Communication backplane, FE-board, FBLOCK controller (FBC).

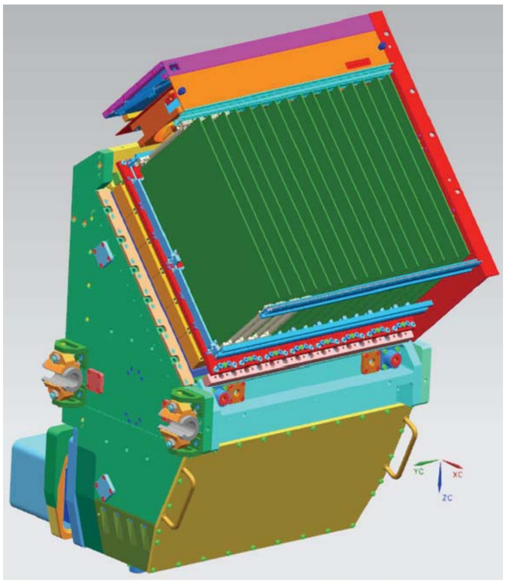

Figure 1.55: Fbox equipped with electronics and its cooling.

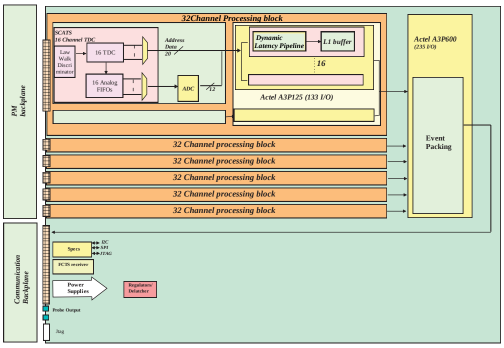

Figure 1.56: Front-end board connected to backplanes.

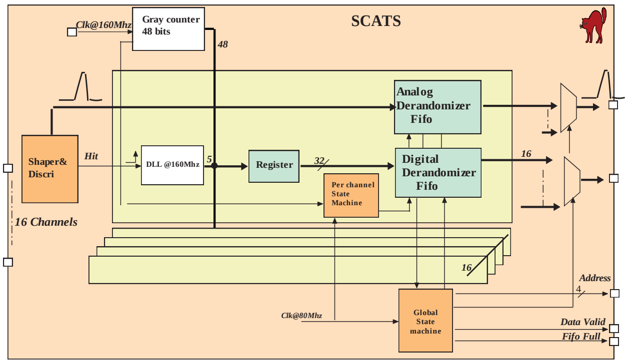

Figure 1.53: SuperB FDIRC TDC chip (SCATS) block diagram.

low walk discriminator receiving the PM outputs and sending logic signal to the TDC part of the chip, and (b) a peak detector. After testing and validation, a final version of the SCATS chip will then be assembled and submitted by end 2013.

The Front-end Crate: The board input will fit the topological distribution of the PMT on the FBLOCK – see Fig. 1.54. In each sector, the PMTs are arranged as a matrix of 6 in vertical direction by 8 in horizontal direction. Each column of 6 PMTs will fit to two FE boards. One vertical motherboard will couple to one column of 6 PMTs. There will be altogether 8 motherboards. The motherboard will convert 4 H-8500 PMT connectors to two connectors, one per FE board. Figure 1.55 shows the Fbox with the front-end electronics.

The motherboard will also distribute High Voltage to the PMT if we use H-8500D. However, in case that we choose the H-8500C PMT, each PMT will have its own HV cable and HV distribution will be separate. In addition to the 8 motherboards, the backplanes receives one communication board for distributing control signals and data between FE boards and the FBLOCK control board. The FB-crate will use many features of commercial crates, such as board guides, rails, etc.

The Communication Backplane: Distributes the ECS and FCTS signals from the FBC to the

16 FE boards thanks to point to point LVDS links. Connects each FE board to the FBC for data transfer. A serial protocol will be used between FE board and the FBC in order to reduce the number of wires and consequently ameliorate the reliability. It will also distribute JTAG signals for FPGA board reprogramming, and also distribute all signals for monitoring and control of the crate.

PMT Backplane: It is an assembly of 8 motherboards each one corresponding to column of 6 PMTs. One motherboard receives 2 FE boards. The 64 channels from 4 connectors per each PMT are merged on the motherboard into two connectors to get into the Front end board to get 16 channels per half PMT, i.e., 6 PMTs correspond to 96 channels per FE board. It also insures the ground continuity between the FE boards, the FE crate and the FBLOCK.

The Front-end Board (FE board): One FE board is constituted of 6 channel-processing blocks handling the 96 channels. The channel-processing block is constituted by one SCATS chip, one ADC, one small Actel FPGA and glue logics. The FPGA receives event data from the TDC and the converted associated charge from the ADC. From one 16 bit bus of the 16 channels coming from the TDC, it de-serializes to 16 data paths where events are kept in a buffer until they are thrown away if there are too old (relatively to the trigger) or sent upon its reception. The PGA master receives event data from the 6 channel processing blocks and packs the event. The FE board transfers the event frame in differential LVDS to the FBC via the communication backplane. Figure 1.56 shows the architecture of the FE-board connected to the backplanes.

The crate controller board (FBC): The FBC board gathers the front-end data and sends them via optical fibers to the DAQ system. There will be one PBC board per crate. The board is separated in several functionalities: (a) acquisition from the front-end boards and DAQ interface, (b) spy data building, c) ECS (SPECS or...) interface, (d) de-serialize clock and control signal from FCTS, and (e) monitor the crate temperature, power supplies, fans, etc.

Cooling and Power Supply: The electronics is located on the detector in a place enclosed by the doors. There are 2 major consequences: one is the problem of the cooling which must be carefully studied in terms of reliability and capability, and the second is that the location is naturally shielded against magnetic field. Consequently the use of magnetic sensitive components as coils or fan trays is possible. An estimate of the overall electronics consumption lead to $\sim$6.1 kW, not including the external power supplies. This can be broken down to individual contributions as follows: (a) electronics: 0.325 W/channel, 500 W/sector, and 6 kW/system; (b) HV resistor chain: 0.19 W/tube, 9.1 W/sector, and 109 W/system. The cooling system must be designed in order to maintain the electronics located inside at a constant temperature close to the optimum of 30 degrees. The air inside the volume must be extracted while the dry, clean temperature controlled air will be flowing inside. Each FB crate will have its own fan tray like in a commercial crate. Targeting a difference of 10 degrees between inside and outside temperature drives to a rough estimate value of 300 m^3 per hour per crate. 4000 m^3 per hour can be considered as the baseline value for the whole detector.

H-8500 PMT has a AC-connection to the last dynode, and this can be used either for triggering or calibration purposes. One can do the calibration with HV off by injecting a pulse and looking at response of all anodes. Figure 1.57 shows a relative pulse height response of 64 anodes to such pulse injection [22]. It is not uniform, but it could be useful to identify possible electronics problems.

Motherboard We presently consider two choices for motherboard geometry: (a) a PC-board combining a group of 6 PMTs (see Fig. 1.58), i.e., we need altogether 8 such motherboard per photon camera, or (b) a single PMT PC-board (see Fig. 1.59). The nominal choice is the 6-PMT motherboard. The total insertion force is 160N/FE board with ERNI connectors and this will have to be tested. To make sure that we do not bend pins in connectors,

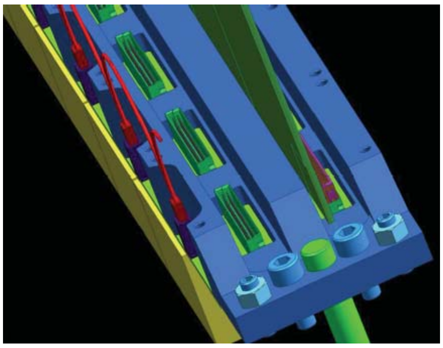

Figure 1.58: A motherboard for six H-8500D tubes, which uses ERNI SMC-Q64004 press fit connectors to couple to FE boards. The total insertion force is 160N/FE board.

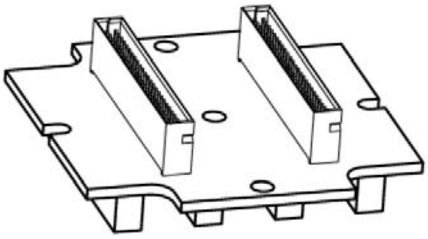

Figure 1.59: A single motherboard for each H-8500C.

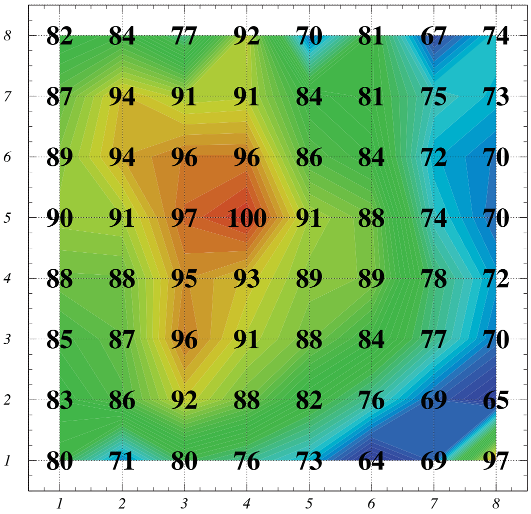

	1	2	3	4	5	6	7	8
8	82	84	77	92	70	81	67	74
7	87	94	91	91	84	81	75	73
6	89	94	96	96	86	84	72	70
5	90	91	97	100	91	88	74	70
4	88	88	95	93	89	89	78	72
3	85	87	96	91	88	84	77	70
2	83	86	92	88	82	76	69	65
1	80	71	80	76	73	64	69	97

Figure 1.57: A relative pulse height response of H-8500 anodes to a pulse coupled to the last dynode [22].

we will need guiding pins. We were considering also zero-insertion connectors (ZIF connectors), however, they are being discontinued and we were advised by TYCO co. not to use them. There will be 16 FE boards per one single FBLOCK. These boards will either be inserted or extracted with a help of tools and rails, a similar procedure as in some commercial crates. Figure 1.60 shows the complete photon camera with the electronics for 48 H-8500 PMTs and 1536 double-pixels.

HV distribution and HV power supplies In case that we choose H-8500C tube, HV cables will be routed under the motherboard as shown on Fig. 1.61. Drawback of this solution is that we will have 48 HV cables in a relatively small volume, and tubes will have to be rotated to fit HV cables in an efficient way.

Resistor chain of each H-8500 tube draws ~150μA at -1.0 kV. The HV power supply will be CAEN, Model A1835, or equivalent. It has 12 independent channels per module, each channel capable of providing up to 1.5 kV and either 7 mA or 0.2 mA (selectable by a jumper). The current monitor has 20 nA resolution. The entire FDIRC HV system would need 48 such HV power supplies, i.e., four per each photon camera. They will be located behind the background shield in the non-radiation area.

In case that we choose H-8500D tube, HV distribution will be distributed on the board as shown on Fig. 1.62. Drawback of this solution is that we would be grouping six PMTs on one HV power supply, which would have to supply 1 A.

Support services FDIRC detector will need these services:

- A boil-off N_2 flow in each bar box up to 100 cc/min per bar box. The N_2 gas has to be distributed in stainless steel electropolished tubing.

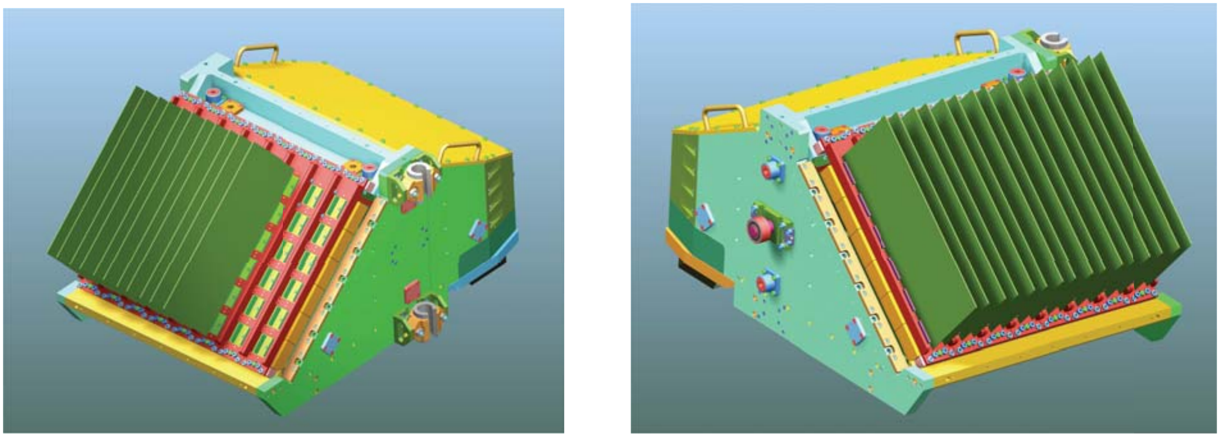

(a) Photon camera with its electronics. (b) Photon camera with its electronics.

Figure 1.60: Photon camera with a high density electronics for 48 H-8500 PMTs.

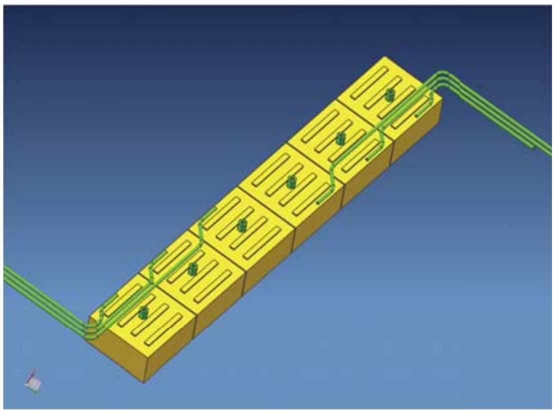

Figure 1.61: HV distribution to H-8500C tubes along the vertical column. Half of tubes are rotated to pack cables efficiently.

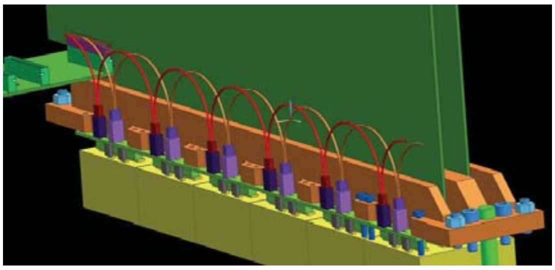

Figure 1.62: HV distribution to H-8500D tubes along the vertical column.

- Total power dissipation in the entire system is about 15kW. The cooling is with water-based heat exchanger and forced air.
- Etc.

1.4.6 Integration issues

Background shield and access to detector maintenance Because the front part of the FBLOCK background shield is mounted on the magnetic door, which is on rails, it will be easy to move it sideways to allow a quick access to the detectors and electronics – see Figure 1.52.

Earthquake analysis of FBLOCK & bar box structure Bar box axial and radial constraints will be equivalent to *BABAR* DIRC setup. The Fbox system itself is not critical, being compact, rigid, and with very limited lever arms. Of course the support disk and the support rails structures of the Fbox must be adequately stiff to avoid resonance in the typical quake range. Axially, the Fbox must be constrained as bar box. The increased risk relative to *BABAR* DIRC consists in the coupling of Fbox and bar box. However, the presence of a RTV gluing layer instead of a rigid coupling and an adequately stiff support of the Fbox should prevent risks due to this coupling. Calculations are in progress.

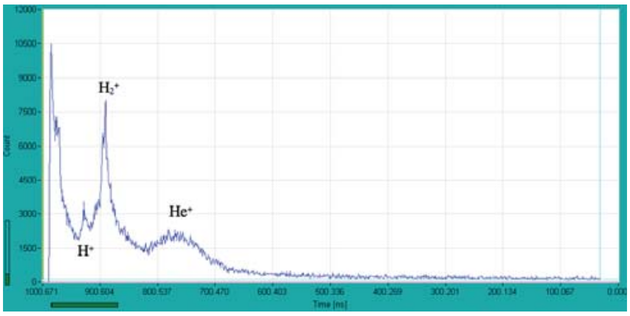

Figure 1.63: A time spectrum of after pulses showing H^+, H_2^+ and He^+ contamination [22].

PMT protection (helium, large backgrounds) It is well known that the PMT operation can be affected by a helium contamination, which can penetrate the PMT glass. These atoms convert to ions in the avalanche process, which can drift back to the photocathode creating secondary photoelectrons, often called 'after pulses'. Therefore, just like in case of the *BABAR* DIRC (which had ∼11,000 PMTs) we assume that any helium leak checking close to the Super*B* detector by accelerator people must not be allowed. Even if it is done far away in the tunnel, air draft could bring it to the detector. We will need a helium detector to monitor this.

Reference [30] summarizes the effect of helium contamination on a PMT. We should stress, however, that we did not do any experimental study with the H-8500 tube up to this point, i.e., we assume that it behaves the same way as any other PMT from this point of view, i.e., that its 64 feedthroughs do not affect it.

The ion contamination in a PMT can be estimated by measuring the after pulsing rate. Figure 1.63 shows how the H^+, H_2^+ and He^+ ion contamination [22] affects a time spectrum of afterpulses in a H-8500 tube. The total measured rate of after pulses was less than ∼1% rate for this tube. This measurement will have to be part of PMT QC procedure to weed out bad tubes. It will be useful to repeat it periodically on some tubes during the Super*B* data taking.

The H-8500 PMT sensitivity to large background were discussed in the chapter about PMT background rate and aging issues. Here we add only that a PMT protection strategy, for example an automatic HV lowering to 80% value if a certain background level is reached, has yet to be developed.

1.4.7 FDIRC R&D Results until now

Test beam results from the first FDIRC prototype Figure 1.5 shows the prototype. This prototype was tested in a 10 GeV electron test beam at SLAC. This beam entered the bar perpendicularly. It was a very successful R&D program resulting in a number of very useful results [9, 10, 11], which can be summarized as follows:

- Learned how to operate new fast highly pixilated detectors (Hamamatsu H-8500 and H-9500 MaPMTs; Burle MCP-PMTs). The H-9500 MaPMT was arranged to have 3 mm × 12 mm pixel size, while the other two tubes had 6 mm × 6 mm pixels.

- Test achieved ∼10× better single-electron timing resolution than DIRC: σ_{H-8500}∼240 ps, σ_{H-9500}∼235 ps, and $\sigma_{MCP-PMT}$∼170 ps.

- Learned how to design a new optics, which is a combination of pin hole coupled to focusing optics, resulting in ∼25× smaller photon camera that the *BABAR* DIRC SOB.

- This was the very first RICH detector establishing that the chromatic error can be corrected by timing – see Fig. 1.6. To be able to do such correction, one needs to achieve a timing resolution at a level of ∼200 ps per single photon, and the photon path length needs to be longer than 2-3 meters. The fact that FDIRC bars are longer due to a penetration of the magnet iron helps to improve this correction.

- With 6 mm size pixels we could reproduce *BABAR* DIRC performance of Cherenkov angle resolution of ∼10 mrad per single photon if we do not perform the chromatic correction. With the chromatic correction

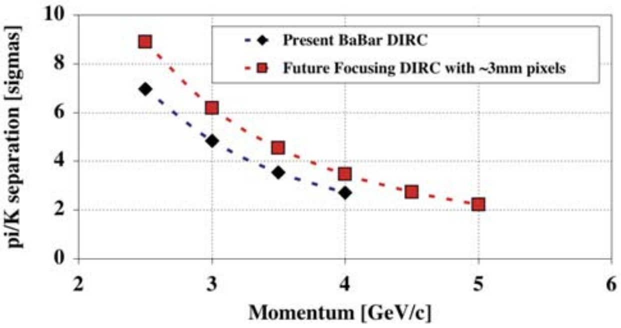

Figure 1.65: Expected $K-\pi$ separation as a function of momentum for a FDIRC detector equipped with H-9500 MaPMTs with 3 mm × 12 mm pixels, compared to the *BABAR* DIRC performance [11].

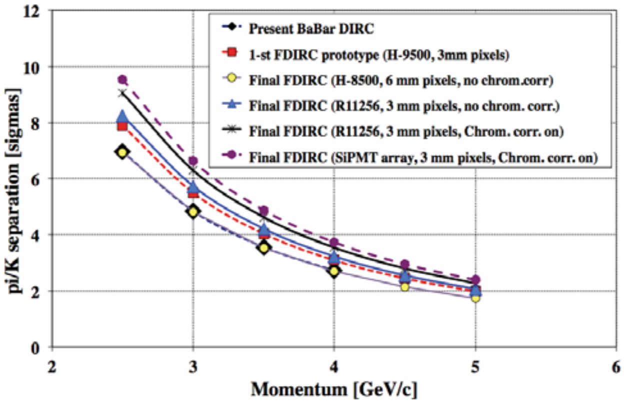

Figure 1.66: Expected $K-\pi$ separation as a function of momentum for various detector schemes, including R11265 pmt and a SiPMT 8 × 8 array (3mm pixel sizes).

one could improve this resolution by 0.5-1 mrad for photon path lengths longer than 2-3 meters – see Fig. 1.4.

- With 3 mm size pixels we could substantially improve on the FDIRC performance – see Figure 1.64. Figure 1.65 shows the expected overall PID performance relative to the *BABAR* DIRC. Clearly, smaller binning in the y-direction would be beneficial to improve the overall performance. However, Hamamatsu has strongly discouraged us to switch to the H-9500 tube as it could not guarantee the deliveries. In addition, the cost of H-9500 tube would be higher. Instead they encourage to use R11256 tube, which would give use 3 mm × 12 mm pad sizes, and possibly QE ∼36%. Figure 1.66 shows the overall PID performance for various detector schemes. The comparison also includes the new Hamamatsu 8 × 8 SiPMT array, where we assumed PDE ∼52% (this is just an example as we do not assume to use it due to its large random noise rate at room temperature and further worsening by a possible neutron damage).
- Discovered a new Cherenkov ring aberration, which worsens the resolution near the Cherenkov wings – see Figures 1.7, 1.8.

CRT test results from the first FDIRC prototype The first prototype was also tested in the cosmic ray telescope (CRT) [31]. The SLAC CRT setup consists of energy absorber made of 4 ft-thick iron, which provides a muon energy lower cut-off of 1.6 GeV. It also provides tracking with 1.5 mrad resolution over angular range of dip angles within 15 degrees. This was also a significant test because it allowed to investigate the Cherenkov angle resolution with 3D tracks [32]. Results can be summarized as follows:

- We learned how to handle 3D tracks in the Cherenkov angle analysis (during the beam test tracks entered perpendicularly [9], [10], [11]).
- Tail in the Cherenkov angle distribution is related to the ambiguity treatment and it is more significant for 3D tracks. The first FDIRC prototype had only two ambiguities: we could not tell a sign of photon vector in the x-direction for photons exiting the bar end, and therefore in the analysis we had to consider both signs. In the final FDIRC prototype we will have six ambiguities. This ambiguity effect enhances the tail as one cannot always reject wrong solution, and it is magnified by

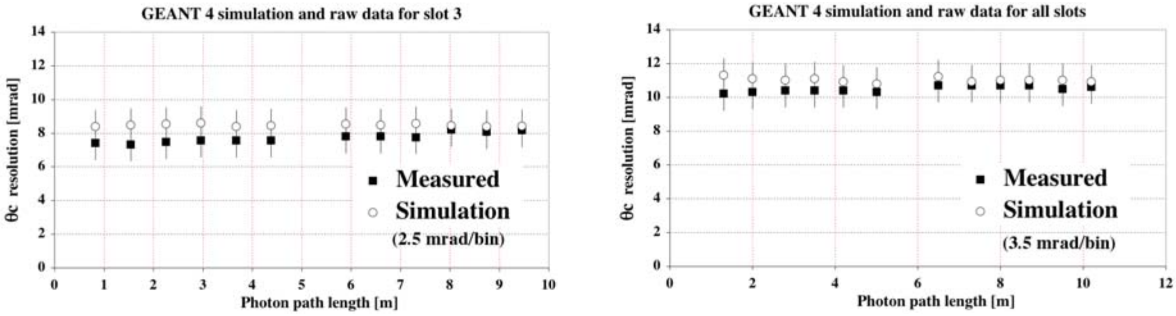

(a) Resolution with 3 mm pixels.

(b) Resolution with 6 mm pixels.

Figure 1.64: Measured and simulated Cherenkov angle resolution without chromatic correction [11]

a presence of background such as delta-rays or showers accompanying CRT muons. The CRT setup is very good to learn how to deal with it. The major conclusion is that one has to use a quantity dTOP = TOP$_{measured}$ - TOP$_{expected}$, where TOP = time-of-propagation of photon in the bar. One makes a tight cut on dTOP and this helps to reject the background, however, it does not help the ambiguity problem.

- Running CRT continuously allowed to test various versions of electronics very conveniently, and to produce the Cherenkov angle resolution under real conditions. So far, every electronics used in the CRT setup, was caught to have some problems, which then had to be fixed. Therefore, we consider the CRT test to be very useful. It is interesting to point out that Belle-II TOP people are trying to create a similar CRT setup.

- The CRT trigger was also used to trigger a PiLas laser diode, which provided a single photoelectron monitoring of all pixels all the time while we were running. The laser trigger did not overlap with the CRT data to avoid a confusion. This allowed to study the stability of FDIRC timing.

- This feature has not been studied so far, but we plan to test the Final FDIRC prototype at high rate background in the CRT setup. This will be done by admixing an asynchronous random light source to the laser calibration signal, while taking a normal CRT data. This task will be accomplished with a fiber mixer, which will mix the laser signal with the random light source. In this way we can study the reconstructed Cherenkov resolution as a function of the random background in a controlled way, and see at what point the reconstruction algorithm breaks down. At the same time we will be monitoring the timing resolution deterioration using the laser signal.

Scanning setups to test H-8500 PMTs and Electronics We have several PMT scanning setups located at SLAC, Maryland, Bari, Padova and LAL-Orsay. These setups differ in their capabilities, designs and electronics. Although these setups did not use yet the final electronics, they were nevertheless already very useful to reveal many H-8500 detector details. So far, the following topics have been studied in some details: (a) efficiency uniformity across PMT for 15 tubes, (b) gain uniformity for 15 tubes, (c) cross-talk, (d) charge charing, (e) after-pulses, (f) pre-pulses (amplification starts on first dynode), (g) anode response to pulses on the last dynode (for calibration purposes), etc. We used many results from these tests throughout this TDR chapter.

In these studies we learned that:

- Based on a study of 15 tubes (960 pixels), the gain uniformity among pixels is typically better than 1:2.5.
- The single photoelectron timing resolution (TTS) has a structure within each pad.
- The charge sharing effect is very small in this particular tube due to its electrode structure, and it is not worthwhile to utilize it to reduce the effective pixel size, which would help to improve the Cherenkov angle resolution.
- Although one can find a good spot in the H-8500 PMT giving a TTS resolution of ∼140 ps (see Fig. 1.13), if one averages over an entire pixel area the TTS resolution is more like $\sim 200 - 250$ ps, with edge pixels being worse (see Fig. 1.14).
- A typical pixel-to-pixel cross-talk in H-8500 tube is about 3%, judging from the scope measurement of pulse amplitudes on neighboring pixels using the SLAC amplifier – see Fig. 1.15.

1.4.8 Ongoing FDIRC R&D

Experience with the final FDIRC prototype in CRT During this stage we learned many things.

- It is possible to build this kind of optics, for affordable cost and within the required tolerances.
- It is possible to handle heavy FBLOCK fragile optics and to assemble Fbox around it.
- We learned how to couple bar box window to the new wedge with Epotek-301 glue.
- We learned how to couple optically the FBLOCK to the new Wedge. It is done with a 1 mm-thick RTV. It is a very large area optical coupling and we learned how to develop a bubble-free coupling. We have demonstrated that this RTV coupling can be cut by a razor wire, surfaces cleaned and glued again.
- The full size FDIRC prototype is now being studied in the cosmic ray telescope.

Detector studies in various scanning setups The study of the H-8500 PMT continues in several scanning setups: SLAC, Maryland, Bari and Padova. So far all tests used various kinds of electronics. It is essential to repeat some of these studies with the final electronics. This, however, cannot be done sooner than in 2013. We also want to make a decision of other tube possible tube choices, namely Hamamatsu H-9500 and R-11256.

Electronics R&D The final electronics is being developed at LAL. The detector motherboard is being designed at LAL, Padova and Bari. Once the first prototype of a small single-PMT motherboard is tested and understood in the Bari scanning setup, 2 complete packages will be available to join the CRT test at SLAC.

1.4.9 System Responsibilities and Management

Management board structure The PID group has a management board, where each institution will have a representative. The role of this management board is to resolve monetary, manpower and other global issues within various institutions as they come during the construction stage. It is assumed that this group will meet with PID conveners during collaboration meetings.

Institutional breakdown by task Table 1.2 shows a breakdown of tasks for various institutions. This should be considered as an expression of interest in a given topic at present. More detailed subdivision into deliverables will be made once the project is in more advanced stage.

1.4.10 Cost, Schedule and Funding Profile

Budget Table 1.3 shows a breakdown of major M&S costs. The cost of FDIRC optics is based on our experience building the FDIRC prototype; it is based on US-based sources. It is

Item	Task	Institution
1	FBLOCK optics	SLAC, Padova, Bari
2	Wedge optics	SLAC, Padova, Bari
3	Gluing Wedge to bar box	SLAC
4	Fbox	Padova, Bari, SLAC
5	Assembly of optics to Fbox	SLAC, Padova, Bari
6	Fbox mechanical support	Padova, Bari, SLAC
7	Electronics	LAL
8	Motherboard	Padova, LAL, Bari
9	Electronics cooling	LAL, Padova
10	Detector testing	Maryland, LAL, Bari, Padova, SLAC
11	Final FDIRC testing in CRT	SLAC, Maryland, LAL, Bari, Padova
12	High voltage	Padova
13	Low voltage	LAL
14	Fiber calibration	Maryland
15	Fast simulation	LAL
16	Full simulation	Maryland
17	Final installation in Super$B$	SLAC, Padova, Bari
18	Thermal protection	LAL, Padova
19	Background monitoring	SLAC, LAL, Padova
20	Helium protection	Bari, ???
21	Boil-off nitrogen distribution	Cabbibo lab, SLAC, Padova
22	Essential services	Cabbibo lab
23	On-line monitoring	???

Table 1.2: Institutional expression of interest in a given topic at present (SLAC involvement is only tentative at present).

interesting to point out that the cost came down by a factor two by the time we finished building it, mainly because we were working directly with companies involved building it. Therefore we have real companies behind each task, and, in principle, we are ready to build it. But one should realize that this is the cost as of the end of 2011.

Schedule and Milestones The FBLOCK production determines the entire production time line, i.e., all other tasks take less time. Figure 1.67 shows the present estimate of FBLOCK production (for clarity we show only 2 FBLOCK production cycles). The manufacturing speed is limited by FBLOCK machining and polishing. The total duration of FBLOCK production, as it stands now, is ∼28 months. The next longest part of the project is the PMT production, which will take about 2 years, including procurement, delivery and testing.

Critical path items Clearly, the most critical path items are: (a) machining and polishing of the FBLOCK optics and (b) delivery of 600 Hamamatsu H-8500 PMTs. The FBLOCK delivery is controlled by the production capacity, which limits deliveries to one FBLOCK every 6-8 weeks. We will try to find a way to speed it up, or find a parallel production possibility, but it is generally difficult to replicate relevant experience with a different company when one deals with a non-standard optics. Hamamatsu company told us that they can deliver 600 H-8500 tubes over a period of 2 years, which is about 25 tubes per month. It is important that we check that delivered tubes have required performance. We may have to split testing into 2 different scanning setups to be able to verify 25 tubes per month.

==========================

1.5 A possible PID detector on the SuperB forward side

1.5.1 Physics motivation and detector requirements

The Super$B$ barrel region is covered by a dedicated PID detector: the FDIRC, described in the previous sections of this report. The information from this detector, combined with the energy losses from the DCH, ensures a good π-K separation up to about 4 GeV/c.On the other hand, PID in the Super$B$ endcaps only relies on dE/dx measurements from the tracking system. In the high momentum region, pions and kaons are only separated at the $\sim 2\sigma$ level – however, the use of the cluster counting method in the DCH [**Ref!? Option or baseline?**], still under study, would increase this separation. Moreover, dE/dx distributions exhibit a 'cross-over' π/K ambiguity region around 1 GeV/c, inside which charged hadrons cannot be properly identified as the energy loss curves overlap.

Improving PID in these two regions requires thus new dedicated detectors which should be both powerful and relatively small. The latter characteristic is needed in order to fit in the limited space available in the endcap regions.

In the backward side – where the particle momentum is quite low in average –, the EMC group is proposing to install a veto calorimeter [**Reference!? Sentence to be updated!?**] to improve the Super$B$ energy measurement. Should this device be fast enough, it would allow one to separate pions from kaons using the particle time-of-flight.

Due to the Super$B$ boost, the forward region of the detector corresponds to a fraction of the geometrical acceptance larger than its angular coverage in the laboratory frame – about $17 - 25°$ – while the particles have higher momentum in average. Therefore, a forward PID detector should be efficient from about 1 GeV/c to 3 GeV/c.

Physics-wise, the Super$B$ performance would benefit from improved PID in many areas:

- larger efficiency in various rare and exclusive B decays;
- reduced background;
- improved exclusive reconstruction of hadronic and semileptonic B channels.

WBS	Task	M&S Cost (Euros)
1.3	FDIRC Barrel (Focusing DIRC)	4.2M total
1.3.1	Radiator Support Structure (new support disc)	18.8k
1.3.2	New magnetic door and inner cylinder	100k
1.3.3	FDIRC photon camera background shielding	125k
1.3.4	Background shield displacement system and rails	31.3k
1.3.5	Bar box transport to Italy	125k
1.3.6	Radiator box/Photon camera assembly	1160k
1.3.6.1	FBLOCK and Wedge material and raw finish (12+2)	761.6k
1.3.6.2	FBLOCK polishing (12+2)	235.2k
1.3.6.3	FBLOCK mirror plating (12+2)	31.25k
1.3.6.4	New Wedge polishing (12+2)	19.04k
1.3.6.5	Gluing Wedge to Bar Boxes	12.5k
1.3.6.6	Clean room (in Italy)	25k
1.3.6.7	Clean room fixtures	25k
1.3.6.8	Shipping charges within US and for shipping to Italy	12.5k
1.3.6.9	QC of optics with digital arm	12.5k
1.3.6.10	Storage cost, services in Italy	25k
1.3.7	Photon Camera mechanical boxes	293.75k
1.3.8	Photodetector assembly	2004.5k
1.3.9	Calibration System	75.6k
1.3.10	Temperature, water, nitrogen, helium leak safety system	10.5k
1.3.11	Alignment services	37.5k
1.3.12	Mechanical Utilities	62.5k
1.3.12	System Integration	125k

Table 1.3: M&S cost breakdown of major PID tasks, except electronics (FDIRC optics cost estimate is based on US-based quotes only and for quantity of 12+2) For currency conversion we used: 1.216 × Euro = 1 dollar.

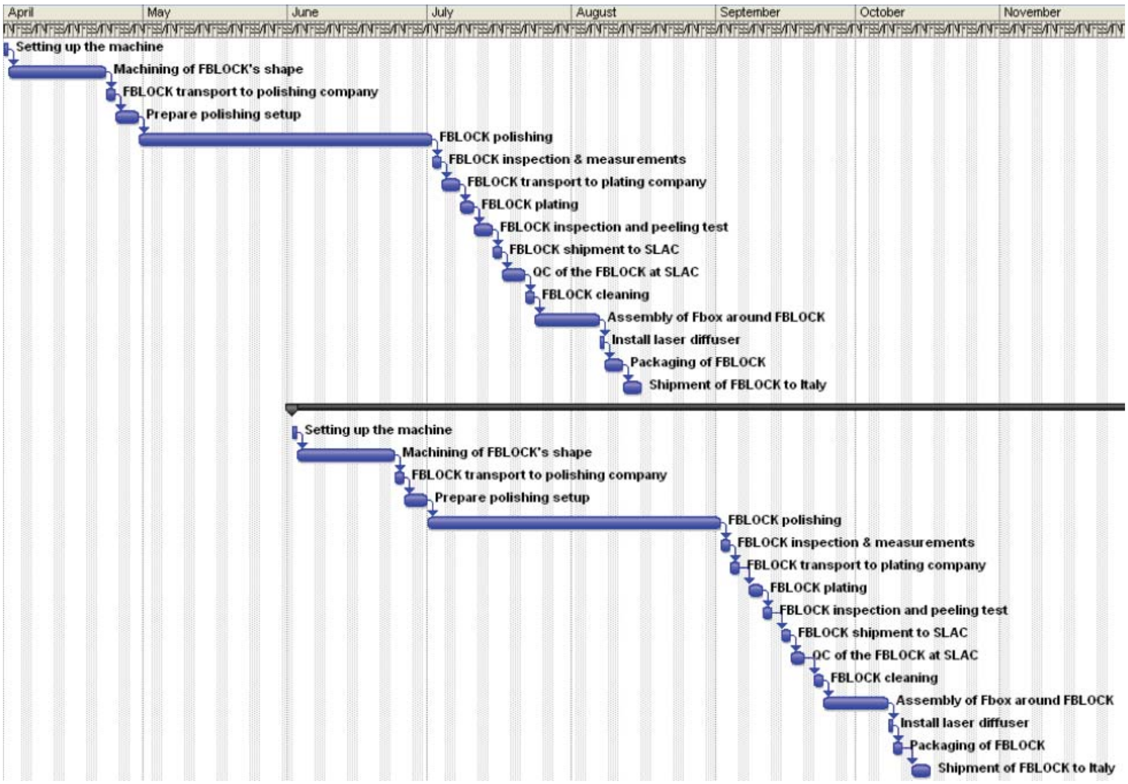

Figure 1.67: FBLOCK production schedule (2 FBLOCK production cycles only).

> This technique is used for recoil physics analysis of rare and hard-to-reconstruct decays. Based on the coherent production of a $B\overline{B}$ pair at the $\Upsilon(4S)$, it first identifies events for which one of the B's, the B_{tag}, is fully reconstructed. Once this is done, the rest of the event automatically corresponds to the (other) signal B: B_{sig}. This constraint provides additional kinematical information on B_{sig} decays which would otherwise be less constrained – e.g. because of undetected neutrinos in the final state. Each of the hundreds of exclusive modes used by this method to reconstruct the B_{tag} is characterized by two numbers: its reconstruction efficiency and the purity of the selected sample. Both numbers increase with an improved PID and the larger the number of particles in the final state, the faster the gain.

Given the integration constraints in the Super$B$ forward region [**update needed!?**], a forward PID detector must be compact. A total thickness around 10 cm would likely put some constraints on the position and dimensions of the DCH and of the forward EMC, but studies [**reference from Matteo!?**] have shown that such changes would only have a limited impact on the performances of these two devices. Yet, the forward PID detector should add the smallest possible X_0 fraction in front of the calorimeter to limit preshowers.

Finally, the cost of the forward PID detector should be moderate in comparison to the one of the FDIRC as it covers a much smaller fraction of the Super$B$ acceptance.

1.5.2 Forward PID R&D activities

From early 2009, several possible designs of forward PID detectors have been studied within the PID group. The proposals were submitted to a task force representative of the whole collaboration. It was charged to review the different designs and to make recommendations to the Super$B$ Technical Board, which would then take the final decisions This step was completed in June 2011 and lead to the choice of a technology, as reported below. In the following paragraphs, the main characteristics of the different proposals such as their advantages/drawbacks are briefly summarized.

Focusing aerogel RICH (FARICH) Ring Imaging Cherenkov detectors are the most powerful instruments used for hadron identification in the momentum region from ∼0.5 to ∼100 GeV/c. The use of multilayer aerogel radiators in proximity focusing RICH detectors (Focusing Aerogel RICH) significantly improves PID performance capabilities of such detectors in comparison with a single layer aerogel RICH. To provide PID at momenta below 0.6 GeV/c we put an additional radiator with the high refractive index.

The FARICH system was suggested for a particle identification in the forward part of the detector. It was known that the main drawbacks of the FARICH in the SuperB detector are space considerations and cost. One of the factors which drives the cost of such detectors is the number of channels. This design was optimized to minimize the number of channels and the total thickness of the system while keeping PID performance on a high level. The concept of the system is presented in Figure 1.68. The main parameters of the system are:

- Expansion gap – 65 mm (total thickness of the system ∼150 mm),
- Photon detectors – the Photonis MCP PMT with 6x6 mm anodes (8x8 matrix), photoelectron collection efficiency – 70%, geometrical factor – 80%,
- 2-layer 'focusing' aerogel, n_1=1.039, n_2=1.050, the total thickness 30 mm,
- NaF radiator, n=1.33, 5 mm thickness
- Number of PMTs – 312
- Number of channels – 20000
- Amount of the material (X/X_0) – 25% = 2.4%(aerogel) + 4.3%(NaF) + 10%(MCP PMT) + ∼8% (support, electronics, cables).

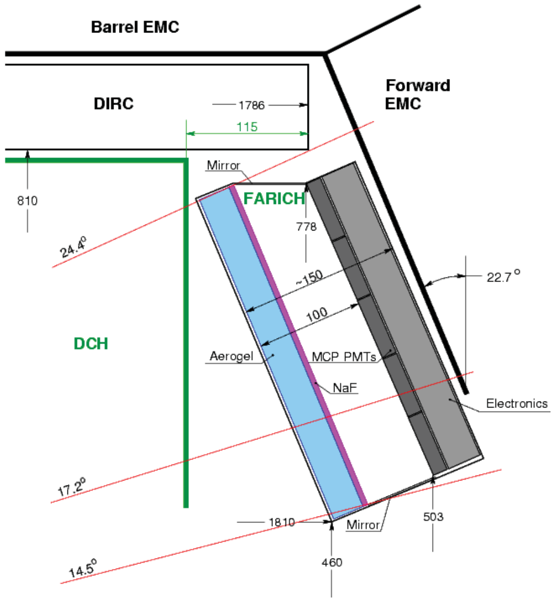

Figure 1.68: Possible FARICH detector layout in the SuperB detector.

The Monte Carlo simulation was done for the proposed configuration. The numbers of detected photons for $\beta = 1$ particle are 16 from the aerogel radiator and 10 from the NaF one. The detector will be able to perform the π/K separation at 3σ level and better from 0.2 to 5 GeV/c, the μ/π separation — from 0.13 to 1 GeV/c, π/p separation — from 1 to 8 GeV/c.

The main goal of the test beam experiment was to demonstrate 'focusing' capabilities of a real multilayer aerogel radiator at short expansion gap and to measure the contribution from aerogel radiator into the resolution on the Cherenkov angle. The measured aerogel tile had 4 layers, maximum index of refraction of the layer was 1.05 and total thickness of 30 mm. The FARICH prototype used 32 MRS-APDs (SiPMs) from the CPTA company (Moscow, Russia) as photon detectors. The APDs active area was 2.1x2.1 mm^2. The custom made discriminator boards and the CAEN V1190B multihit TDC were used for the signal readout. The test beam facility was constructed at VEPP-4M collider at the Budker INP in Novosibirsk for a detector development. The test beam apparatus also comprised the trigger and veto scintillation counters, the coordinate drift chambers and the NaI calorimeter.

During the experiment we have measured simultaneously coordinates of the track of 1 GeV/c electrons and coordinates of the detected Cherenkov photon from multilayer aerogel radiator. Having this information, we determined Cherenkov angle single photon resolution. The expected π/K separation based on measured single photon resolution and producer's data for Photonis MCP PMTs is presented in Figure 1.69.

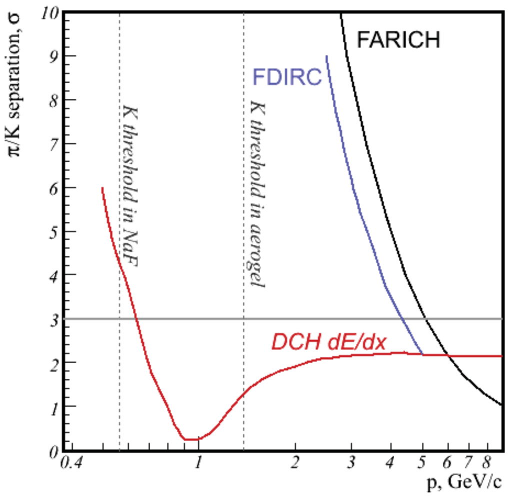

Figure 1.69: The expected FARICH π/K separation based on the test beam data together with expected FDIRC and dE/dX π/K separation.

Our research has shown the ability to build FARICH PID system for SuperB detector. The multilayer 'focusing' aerogel radiators are available. The background conditions are on the low level for this detection technology. The expected life time of the PMTs during experiment is about 10 years or more. After the detail investigations it was concluded that the gain in detection efficiency of the whole detector is not so significant in comparison with the cost of the system and the necessity to cut drift chamber to organize space for FARICH. Finally, the

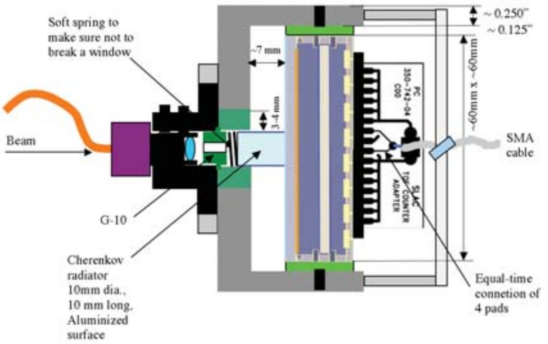

Figure 1.71: A geometry of pixilated TOF prototype detector used in our tests (a pair of such detectors were used in our tests).

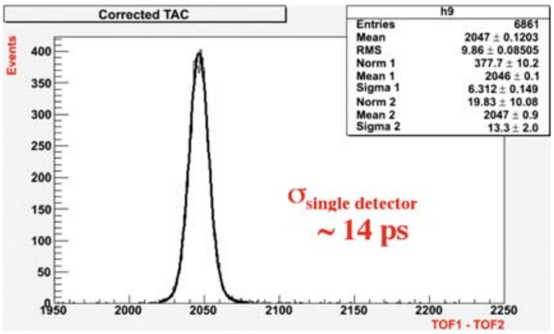

Figure 1.72: The best result obtained in the Fermilab test beam with the Ortec 9327 electronics.

FARICH option for Forward PID is not supported.

Pixelated time-of-flight detector with Cherenkov radiators Figure 1.70 shows a possible concept of a final TOF detector. It uses polished and side-coated fused silica radiator cubes, which are optically isolated from each other. The radiator cubes are coupled to a MCP-PMT detector with 10 micron holes. This concept is the most simple of all TOF concepts as it avoids complicated 3D data analysis and minimizes the chromatic effects. On the other hand, it requires a large number of MCP-PMT detectors, which increases the cost prohibitively at present. However, if such detectors would become cheap at some point in future, one could revive this concept again.

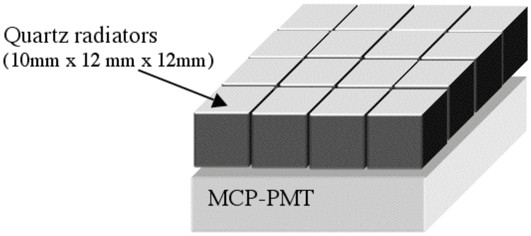

Figure 1.70: A possible geometry of final pixilated TOF detector: polished and side-coated fused silica cubes coupled to the MCP-PMT detector.

Figure 1.71 shows a prototype of the pixilated TOF concept, with a coated fused silica radiator cylinder. The detector had a fiber allowing calibration and laser-based bench-top tests. The radiator was coupled to Photonis MCP-PMT with 10 micron holes. There were two such detectors, operating in tandem, and the quoted resolution is a relative between them. The reference [33] summarizes all work towards this concept.

Figure 1.72 shows the best resolution obtained with the TOF prototype in the Fermilab beam test. The detector operated at low gain, which means it did not achieve the ultimate resolution. The low gain operation was intentional to avoid aging in the SuperB environment.

Figure 1.73 shows all our test results both in the test beams and laser-based bench-top experiments. These results were obtained with Ortec 9327 CFD electronics, WaveCatcher, DRS4 and Target waveform digitizers. One can see that waveform digitizers "almost" reach the resolution of the classical CFD electronics, but not quite.

Figure 1.74 shows the laser-based test results as a function of the signal-to-noise ratio (S/N). A large value of S/N ratio is essential to achieve a good timing resolution. In these tests we achieved $\sigma(electronics)$~2.42 ps with Ortec 9327 CFD electronics. Therefore the detector contribution to the final ultimate timing resolution was $\sigma(detector)$~3.6 ps for S/N of ~1400. To achieve such a high value of S/N ratio in

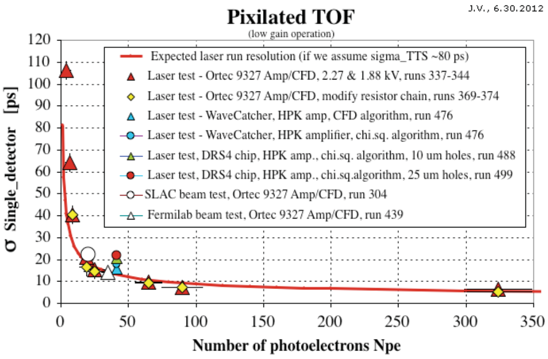

Figure 1.73: A summary of all results with the pixilated TOF prototype, which included beam and laser tests.

practice is difficult, as there are many limitations. The most important limitation is due to MCP detector aging, which erquires a low gain operation. One could also have to avoid using an amplifier entirely to improve S/N, as the amplifier is a large contributor to the noise (Ortec 9327 CFD electronics has internal 10x amplifier). It is probably more realistic in practice to reach S/N ∼200, i.e., the resolution of 10-12 ps.

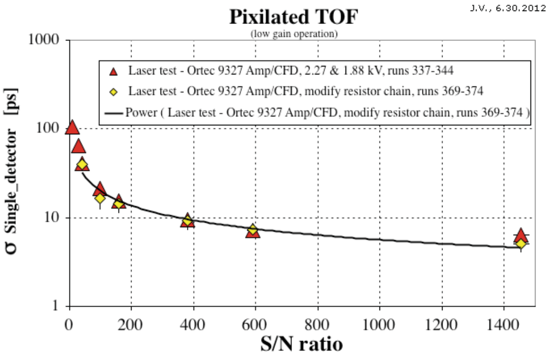

Figure 1.74: A summary of our laser-based results with the pixilated TOF prototype with the Ortec 9327 CFD electronics as a function of signal to noise ratio (S/N).

Scintillating detector coupled to G-APD arrays [Jerry] Because of the prohibitive cost of MCP-PMT detectors for the entire forward pixilated TOF detector design at present, we considered other possible "pixilated" schemes based on scintillators and G-APDs. We used the CRT telescope at SLAC capable of testing various options using 3D muon tracks. The 3D tracks with dip angle up to 20 degrees will somewhat worsen the timing resolution, however, it provides more realistic results compared to test beam. We used various types of scintillators (BC-404, BC-420, small and a full size LYSO) for the radiator. The logic for the full size LYSO radiator was to see if one could "parasite" on end-cap calorimeter by adding a 4x4 G-APD array on its front face. The photon detection in these tests was provided by either MCP-PMT (for a reference run only), or Hamamatsu 4x4 G-APD array (each pixel size is 3 mm x 3 mm), or simply a pair of single 3 mm x 3mm G-APDs (either MEHTI or Hamamatsu MCCP) coupled to side of the small scintillator. The overall goal was to reach ∼100 ps only to provide a PID identification in the dE/dx cross-over region. Table 1.4 shows a summary of all results [34]. One can see that we could reach resolutions between 110 and 180 ps for several small scintillators. However, the full size LYSO crystal results were considerably worse. Although one could search for some further improvements in future, it was felt that this type of TOF counter cannot compete with FTOF concept at present.

DIRC-like forward time-of-flight detector (FTOF) As indicated by its name, the FTOF [6] belongs to the family of the DIRC detectors [3]. Charged particles cross a thin layer of fused silica; provided that their momentum is high enough, they emit Cherenkov light along their trajectories. Part of these photons are trapped by total internal reflection and propagate inside the quartz until an array of Multi-Channel Plate Photomultipliers (MCP-PMT) where they are detected. Unlike the (F)DIRC, no attempt is made to reconstruct Cherenkov angles: K/π separation is provided by time-of-flight: at given momentum, kaons fly more slowly than pions as they are heavier. Given the short flight distance between the IP and the FTOF (about 2 meters, hence a 90 ps difference for 3 GeV/c particles), the whole detector chain must make measurements accurate at the

Radiator	Detector	Measured resolution
Small LYSO (17 x 17 x 17 mm^3)	MCP-PMT	109 & 159 ps
Small LYSO (17 x 17 x 17 mm^3)	4x4 G-APD array (pixel 3 mm^2)	140 ps
Large LYSO (25 x 25 x 200 mm^3)	4x4 G-APD array (pixel 3 mm^2)	220 ps
Scintillator (17 x 17 x 17 mm^3)	4x4 G-APD array (pixel 3 mm^2)	136 ps
BC-404 scintillator (38 x 38 x 25 mm^3)	Two single 3 mm^2 G-APDs	156 ps
BC-420 scintillator (38 x 38 x 10 mm^3)	Two single 3 mm^2 G-APDs	177 ps

Table 1.4: Results with TOF pixilated detector using scintillator radiators using 3D tracks in the cosmic ray telescope (CRT).

30 ps level or better. This is one of the main challenges of this design, the others being the photon yield, the sensitivity to the background (including ageing effects due to the charge integrated over time by the photon detectors) and the event reconstruction. Regarding the latter point, one should emphasize that the FTOF is in fact a two-dimensional device: the PID separation uses both the timing and spatial distributions of the photons detected in the MCP-PMT arrays.

1.5.3 The Forward task force

Charge and activities In July 2010, a taskforce on a possible forward PID system in the Super$B$ detector was formed. Its primary charge was to provide an assessment of

- the physics impact of a PID system in the forward region of the Super$B$ detector, roughly defined by the polar angle range 17° to 25°;
- the feasibility of the proposed detector technologies for the forward PID system.

The taskforce considered a list of questions and criteria for both physics and technology assessments, as discussed below.

- Physics evaluation
  - A list of key benchmark physics channels that are affected by a forward PID system were evaluated for both the gain and any potential negative impact due to the added material before the forward EMC or any required changes to the DCH dimensions.
  - A preliminary performance evaluation was made of some of the proposed technologies, in the presence of background hits.
  - The impact of each proposed forward PID technology on π^0 efficiency, and momentum and dE/dx resolutions in the DCH was performed.
- Detector technology issues
  - Estimates of cost, required manpower, and construction schedule for each of the proposed technologies were performed. These include information on the availability of components on the time scale of the Super$B$ construction schedule.
  - The need for a proof-of-principle was considered for each of the proposed technologies – at least with cosmic rays and if possible with beam tests. Issues common to nearly all devices are: performance in presence of background; the effect of the Super$B$ magnetic field on the photodetectors and on the overall performance of the device; photodetector aging.

  - Integration issues.

The taskforce met with forward PID proponents at all Super$B$ workshops between September 2010 and May 2011 when the committee recommendation was released. There were also phone meetings in between workshops.

Summary and taskforce recommendation The physics gain from a forward PID deviced is around 4-5 % for the benchmark channel $B \to K^{(*)}\nu\bar{\nu}$: roughly 2%/kaon. No physics channel with higher gain has been identified. Results based on simulation and beam test (1 GeV electrons) show no significant degradation of resolution & efficiency for γ and π^0. In addition, the impact on tracking resolution due to shortened DCH has been estimated to be ∼1% degradation in momentum resolution/cm cut.

The overall assessments for the proposed detector technologies are the following.

- FARICH. On the whole, this technology is likely to yield the most powerful – and robust – PID performance, extending well above the nominal 4 GeV for B decays. The expected performance is verified by impressive beam test results. However, no physics channel that would significantly gain from the extended performance has been identified. Moreover, the required cut of ∼17 cm to DCH length significantly degrades momentum resolution in this angular region. This is an unacceptably large negative impact on the detector performance and a too severe constraint on the tracking system. Hence, the taskforce does not see this technology appropriate for forward PID in the Super$B$ detector
- Pixelated TOF (LYSO plus G-APD array option). This technique, due to its potential minimal disturbance on the rest of the detector and likely modest cost, was deemed very attractive. At the aimed resolution of ∼100 ps, it would complement the dE/dx measurements for K/π coverage below 2 GeV. However, with the obtained time resolution (∼230 ps) for a full size LYSO crystal in cosmic ray tests, the proponent & taskforce have concluded that this technique will not deliver the required performance.
- FTOF. Simulation studies and cosmic ray tests – see below – have demonstrated that key aspects of this technique can be attained – including the goal of a time resolution of ∼90 ps/hit. But there remains significant uncertainties on the expected background level and its impact on PMT lifetime. The taskforce believes this technique could be appropriate for the forward PID system provided that background (and radiation) issues are understood – which may require further studies of the IR design and shielding – and that a full prototype of the system is developed and tested, to verify the expected performance, in particular the pattern recognition in the presence of background hits.

The final recommendation for the forward Super$B$ region is the following: the importance of hermeticity (and redundancy) in PID coverage will increase as we approach the systematics-dominated era in the Super$B$ physics program. Hence, the taskforce members believe – independently of the outcome of the current technology evaluation – that there is physics merit to allowing a gap of $\sim 5-10$ cm in the forward region for a PID device. This would allow for introduction of a system at a later stage of the experiment, in case the detector studies are not completed in time for the initial installation of the Super$B$ detector.

1.5.4 The DIRC-like forward time-of-flight detector (FTOF)

Design optimization The performances of the FTOF depend on two main parameters which should be optimized simultaneously. One is the photon yield per track, which should be as high as possible; the other is the photon timing jitter, which should be minimized in order to efficiently separate kaons from pions. Both are strongly related to the geometry of the detector.

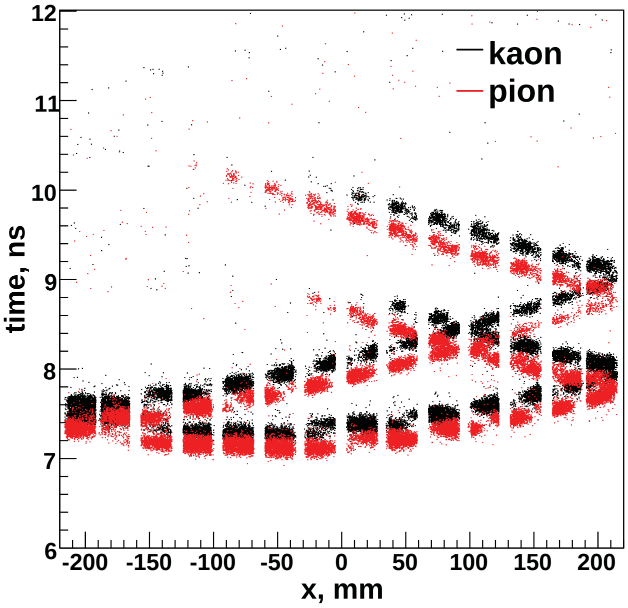

Figure 1.76: The FTOF is a 2D-device: in addition to the photoelectron timing, the distribution of hits in the MCP-PMT channels is also a discriminating variable to separate kaons from pions, as shown on the two plots displayed in this figure. Both show the time versus position of hits generated by 2 GeV/c kaons (black) and pions (red) **[To be updated]**. $t = 0$ corresponds to the particle generation at the IP while x is an axis along the tile width which shows the MCP-PMT position. The 14 photodetectors are clearly visible such as the small gaps between them.

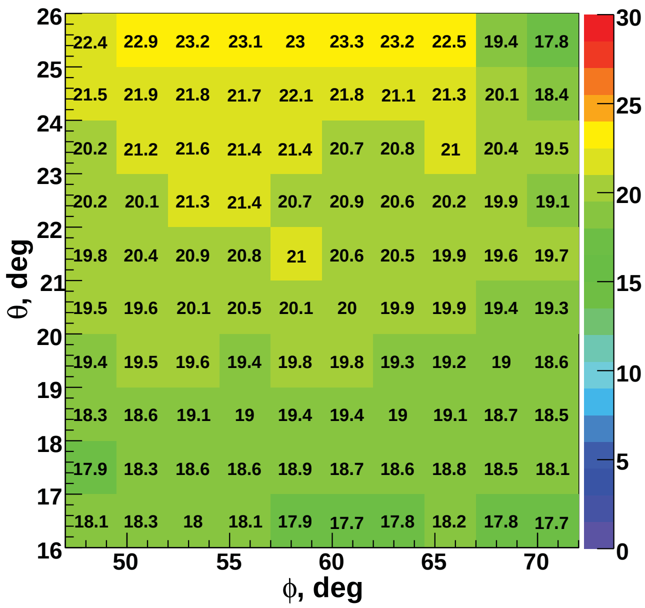

Figure 1.75: Map giving the mean number of detected photoelectrons in a FTOF sector as a function of the polar (θ) and azimuthal (ϕ) angles. This map is drawn for 800 MeV/c kaons shot from the IP in a simplified detector model including the 1.5 testa longitudinal solenoid field.

The number of Cherenkov photons produced by a given track scales linearly with its path length in fused silica. Simulations show that a 1.5 cm thickness for the quartz tile is a good compromise between light yield and detector thickness in term of X_0. This finite size introduces an irreducible component of the photon time jitter (about 50 ps), as Cherenkov photons are emitted uniformly along the track path inside the tile. Their initial directions lie on a cone which opening angle depends on the track velocity (which is a function of the particle measured momentum and of its unknown mass) and on the medium optical index ($n \approx 1.47$ in fused silica). The main axis of the cone is aligned with the track direction.

Therefore, it is clear that photons from a given track can follow several different paths before being detected in a MCP-PMT channel. This is another source of time jitter which has to be taken into account. One way to mitigate it is to select only the 'most-direct' photons which reach the detectors after at most few reflections on the tile front and back faces. This can be done by covering the tile sides by photon absorbers but the loss in photon yield would be too high. In the current design, only the tile

Figure 1.78: The 16-channel Wavecatcher board.

long and make their timing unusable. Indeed, with tiles perpendicular to the beam axis, photons are mainly ’upward-going’: they are travelling towards the tile outer radius first which is why the MCP-PMTs are located in this area.

Given the accuracy of the timing measurements required by the FTOF, chromaticity is another effect which cannot be neglected: the smaller the photon wavelength the larger its speed – ’red’ photons are faster than ’blue’ ones.

The FTOF photon yield also depends on the tile orientation as only Cherenkov photons trapped inside the quartz by total internal reflection can be detected. Using vertical tiles as reference, simulations show that a 10° tilt in the forward (backward) direction increases (decreases) the yield by about 15% in average. But configurations in which the FTOF is bent forward are impossible in practice, due to integration constraints on the Super$B$ forward side.

Current design The DIRC-like forward time-of-flight detector is made of 12 thin fused silica tiles (1.5 cm thick each, which corresponds to 12% X_0) located perpendicularly to the beam axis and covering 30° in azimuth each. The requirements for the tile dimension accuracy and the fused silica polishing quality are less stringent than for the BaBar DIRC bars, as the Cerenkov photons will bounce much less in the quartz. Therefore, building the FTOF tiles should not be an issue given the knowledge accumulated in this area over the past two decades.

Each FTOF tile will be placed into a light aluminium box which will be the equivalent of the DIRC bar boxes for the DIRC quartz bars. To keep the fused silica tiles as clean as possible, the tile box should not contain any other detector component; there will just be an optical contact between the quartz and the MCP-PMTs. Both the tile box and the box enclosing the MCP-PMTs will be light-tight; in addition, the tile box will be leak-tight and N_2 will flow continuously inside it to avoid any moisture.

The prototype FTOF front-end electronics is based on the new ’WaveCatcher’ boards commonly developed by LAL Orsay and CEA/Irfu Saclay. They are 12-bit 3.2 GS/s low power and low cost waveform digitizers based on the SAMLONG ultra-fast analog memory. The sampling time precision is as good as 10 ps rms, a value measured at the level of a crate hosting eight 2-channel boards. The photon arrival time is extracted via digital Constant Fraction Discrimination (CFD). A new 16-channel board recently designed has been characterized: it exhibits the same timing performances.

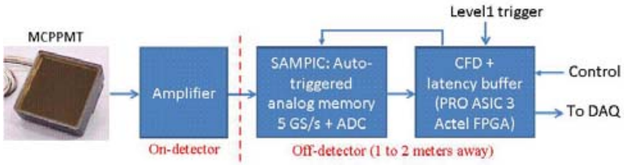

Figure 1.79: Schematics of the FTOF whole electronics chain.

The final electronics will be highly integrated and based on a new principle of TDC, called SAMPIC. The latter, designed in AMS CMOS 0.18 μm technology, will be able to tag the arrival time of 16 analog signals with a precision of

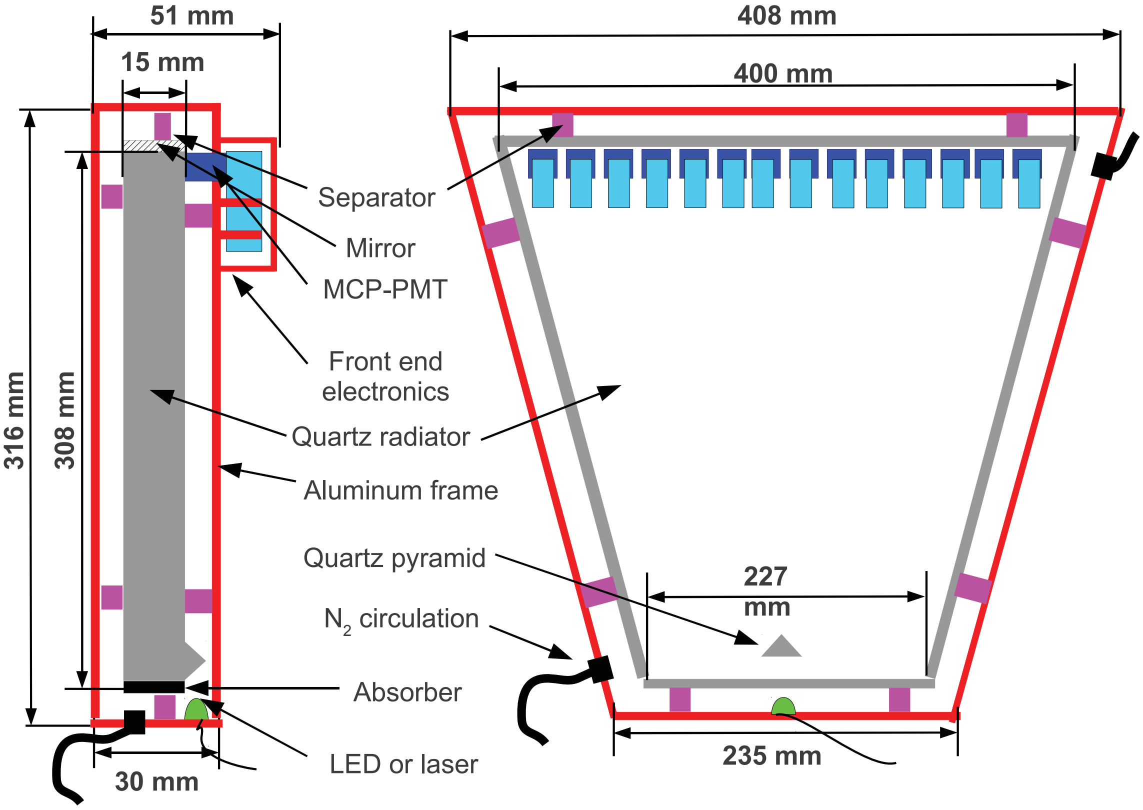

Figure 1.77: Current design of the FTOF tile: front and side views.

a few ps thanks to its embedded analog memory (running between 5 and 10 GS/s) and its embedded ADC. This will permit housing at least 64 channels in a final front-end board. In the current FTOF design, there are 56 channels per sector; hence, a single 16-channel Wavecatcher board will be enough to readout a sector (hence 12 boards will be needed in total for the whole FTOF).

The FTOF front-end boards will be located outside the detector, both for protection from background and radiation, and to allow easy access for repair. The analog signal will be amplified right behing the MCP-PMTs and then transfered to the front-end board via signal cables.

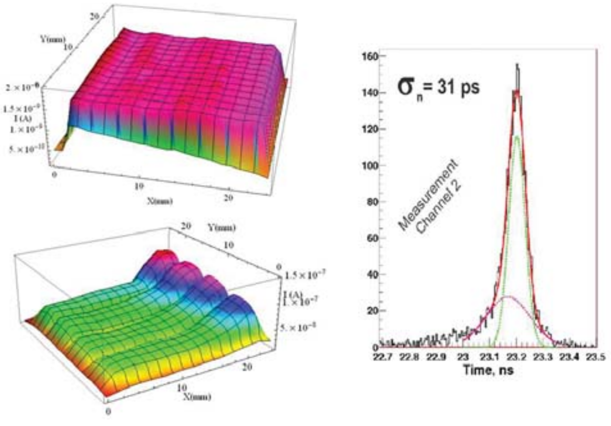

Figure 1.81: Top left plot: SL-10 photocathode response mapping; bottom left plot: 4 anode response mapping; right plot: single photoelectron timing resolution (FWHM).

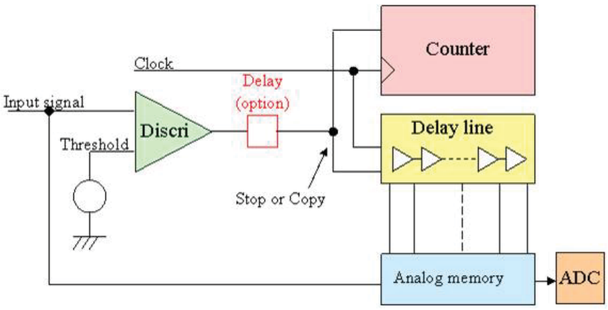

Figure 1.80: Scheme of the new TDC for the FTOF electronics.

As explained above, the whole FTOF measurement & processing chain must be ultra-fast. The time resolution per photon must be at the level of 100 ps or better, which makes the use of MCP-PMTs mandatory. Among the product available on the market, the Hamamatsu SL-10 is currently our baseline. With an advertised time-transit-spread (TTS) of 70 ps (FWHM), an active area of 22×22 mm^2, a quantum efficiency of 17% and a lifetime of $\sim$2 C/cm^2, it offers a good compromise given the FTOF requirements. Two such photon detectors will be characterized at LAL-Orsay in the coming months. In the current design, one needs 14 SL-10 per sector, hence 168 in total; each MCP-PMT will host 4 different channels which will all have their own HV channel. The HV power supplies will be located behind the detector shield wall and could then be accessed 24/7.

A fully instrumented FTOF sector is expected to be very light: about 12 kg total.

First test of the detection method A test of the FTOF detection concept was run at SLAC in the Cosmic Ray Telescope (CRT) between Fall 2010 and Spring 2011. The SLAC group provided the hardware (two short rectangular fused silica bars readout by a photonis MCP-PMT) and the test facility while the LAL team brought new 2-channel USBWC boards, which performances were tested for the first time at the level of a whole crate. The test setup is shown in Figure 1.82. Cosmic muons cross the two bars located on top one another. They emit Cherenkov light inside, which partly propagates until the instrumented end of the bars. By shorting and grounding pixels, one defined 16 MPC-PMT vertical pads – 8 for each bar – which were connected to the USBWC electronics.

For technical reasons, the CRT and USBWC DAQ systems were separated. CRT trigger is asserted by a fast Cherenkov counter located under the two bars. When a trigger signal is sent out, the 16 USBWC analog buffers are readout to see if photons have been detected by one or more pads. If this is the case, the USBWC event is written to disk. Coincidence between CRT and USBWC events is done offline by comparing the time of the recorded events in the two streams. After an initial period of commissionning, about 400,000 cosmic muons were collected during two months of nominal running. Absorber sheets had to be placed in front of the MCP-PMT to reduce significantly the number of photons detected by channel. Indeed, as the photon timing is measured by a sophisticated CFD-based algorithm, a second photon too close in time from the first detected one would distort the waveform shape and spoil the timing measurement.

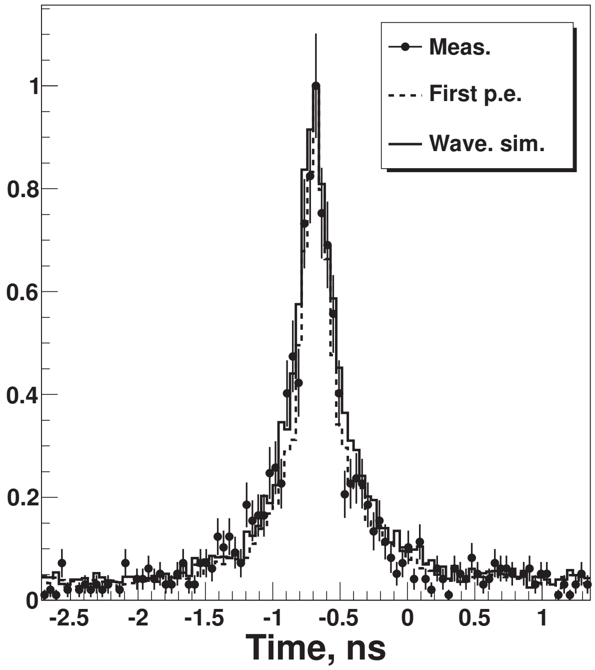

Figure 1.83: Comparison between data (bullets) and simulations (histograms) [**To be updated**] for the time difference between two MCP-PMT channels among the 16 readout by the USBWC boards. All distributions are scaled so that their peak is equal to 1 in arbitrary units. The data-MC agreement is impressive, both for the core and the tails of the distributions. Similar results are achieved for all pairs of channels studied.

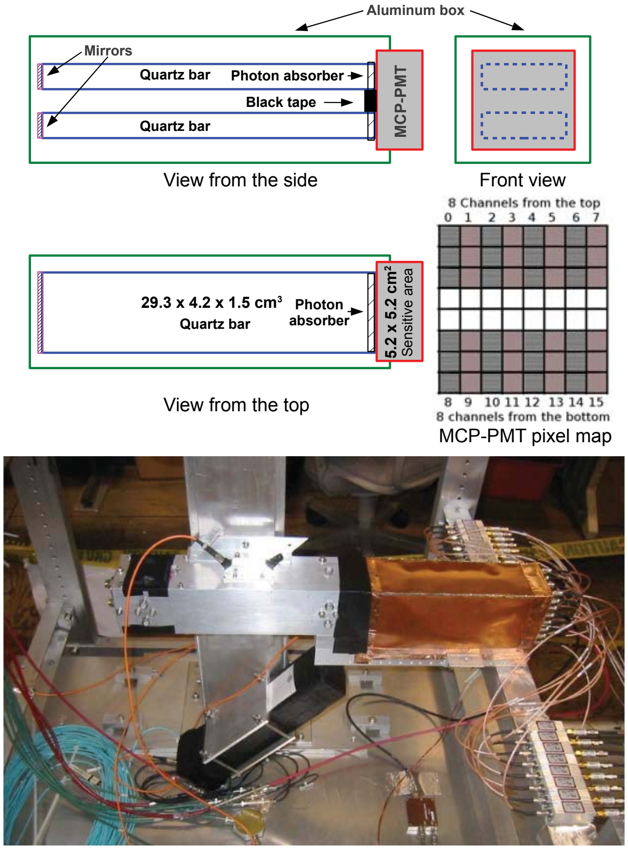

Figure 1.82: Top: side and top views of the 2-bar setup; the 16 channels readout by the USBWC boards are shown on the right-hand side. Bottom: picture of the apparatus in the SLAC CRT: the orange box is a Faraday cage containing the USBWC electronics while the grey box contains the prototype. Under these items, on can see the enclosure of the sloping fast quartz counter which is used to trigger the CRT in coincidence with the hodoscopes.

As explained above, USBWC events of interest are selected by requiring a time coincidence with a CRT event, plus some additional quality cuts on the CRT data. As no accurate timing reference is available, the current determination of the prototype time resolution is based on time difference between channels. All pairs of channels have been considered but they are studied separately as the resulting timing distributions depend on the photon paths compatible with the particular two MCP-PMT pads. The interpretation of these data is not straightforward as photons emitted by a muon track can follow several different paths to reach a particular effects (spread of the Cherenkov photon emission time due to the finite quartz tile width; multiple photon paths inside the fused silica to the MCP-PMTs; variation of the cosmic muon track parameters, etc.). This preliminary result should be confirmed by a reanalysis of the data based on 3D-tracking and aiming at comparing the photon measured and expected times.

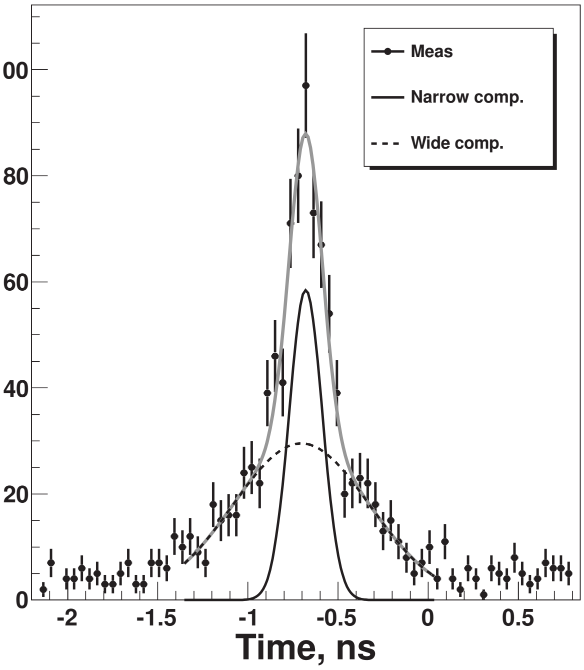

Figure 1.84: Double Gaussian fit to a representative distribution of the time difference between two channels. The width of the narrow component is interpeted as the prototype device while the wide component accounts for multiple photon paths (and hence multiple timings) between pads.

Background and ageing studies The FTOF sensitivity to background can be seen in two ways. First, background hits could shadow real signal hits too close in time and/or add confusion in the pattern reconstruction algorithms used to extract PID information from the FTOF data. Moreover, the background rate will translate into a acculumated charge on the MCP-PMT cathode. The consequence of the latter will be a slow decrease of the MCP-PMT quantum efficiency; at an integrated charge around 1-2 $\mathrm{C/cm^2}$, the photon detectors will cease working properly. Therefore, it is crucial to estimate the FTOF background accurately and to find ways to decrease it as much as possible. In addition, the MCP-PMT gain should be high enough to keep the TTS low, but not too high as it limits the MCP-PMT rate.

Full Geant4 simulations of the Super*B* interaction region (detector included) simulating the main backgrounds – radiative Bhabha, Touschek particles, etc. – have shown that the dominant FTOF background is due to off-energy positrons which hit the beampipe about one meter away from the IP on the forward side. This localized background source can be mitigated by increasing the thickness of the tungsten shield which protects the detector. Initial studies have shown that going from 3 cm to 4.5 cm decreases the FTOF rate by a factor 3 to about 115 $\mathrm{kHz/cm^2}$ The latter value is still a bit high for five years of high gain running at nominal luminosity; therefore, work is ongoing to confirm and improve this promising result.

Ongoing activities and plans As explained above, the FTOF technology has been chosen by the Super*B* collaboration for the forward PID detector. Therefore, if one such device is to be built, that will be the FTOF. Yet, to be included in the detector baseline, a full-size prototype of a FTOF sector must be built and validated, both in cosmics and test beam.

As a first step, a fused silica tile (Spectrosil 2000 from Heraeus) has been purchased by the LPSC Grenoble group (which joined the FTOF development in 2011). It will be placed in a cosmic ray telescope specifically designed for the FTOF geometry with an active area of 0.23 $\mathrm{m^2}$ and good resolution on position ($\sim 0.3 - 0.6$ cm) and angle ($\sim$0.2 deg). Different absorber thicknesses are used to select 7 momentum ranges of the muons from 300 MeV/c, the thicker absorber giving a lower cut at 1.7 GeV/c. The yield of this telescope is 1 Hz for the full momentum spectra and only 0.2 Hz for the higher energy bin. The main purpose of this setup is to study the photon yield versus the muon impact position and incident angle, using several coatings on edges and faces.

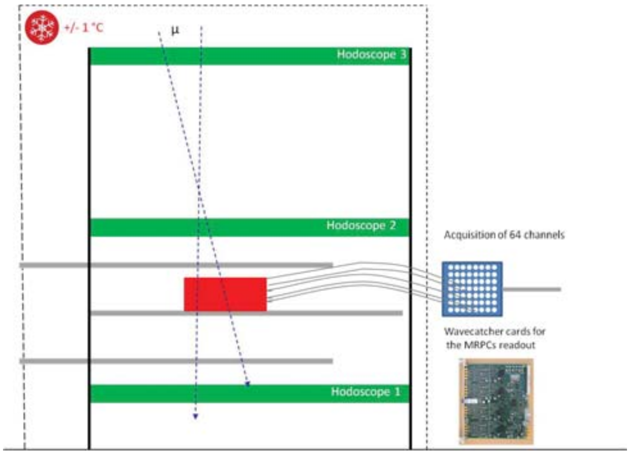

Figure 1.85: The CORTO setup.

These setups will be used to measure the photon collection efficiency and timing in various configurations. These data will allow one to validate the full Geant4-based optical simulations.

In CORTO, the fused silica tile will be tested with different MCP-PMTs: R10754X (SL-10) from Hamamatsu and XP85112 from Photonis. [+ **Russian MCP-PMT!?**]

In the meantime, the FTOF design will go on, benefiting from improved simulations and progress on the geometry of the crowded Super*B* forward region. Discussions are also ongoing about the best location of the MCP-PMTs: at the outermost radius they are subject to less background but accessing them for repair would be extremely difficult. On the other hand, putting the MCP-PMTs at the innermost radius would require tilting the FTOF significantly (to have a larger fraction of Cherenkov photons downward-oriented), which is likely unfeasible given the integration constraints on the Super*B* forward side.

Once the FTOF design is frozen, the building of the prototype will start – its cost is strongly dominated by the MCP-PMT price. Assuming that the whole project proceeds smoothly and that the FTOF is accepted by Super*B*, a detailled appendix of the present detector TDR will be published to provide all the needed information to support this innovative detector.

MCP-PMT	Effective area (mm^2)	Quantum efficiency (QE) @ 400 nm	Typical gain	Transit time spread (FWHM)	QE reduction after 2 C/cm^2 accumulated charge
R10754X-01-L4	22×22	17%	10^6	70 ps	20%
XP85112/A1	53×53	22%	10^5	82 ps	Unaffected

Table 1.5: Comparison of two MCP-PMTs candidate for the FTOF.

Bibliography

[1] C. Amsler *et al.*, (Particle Data Group), Phys. Lett. B 667, 1 (2008).

[2] `http://nobelprize.org/nobel_prizes/physics/laureates/2008/press.html`, and `http://www-public.slac.stanford.edu/babar/Nobel2008.html`.

[3] B. Ratcliff, SLAC-PUB-5946, 1992; and *Simple considerations for the SOB redesign for Super*B, `http://agenda.infn.it/conferenceDisplay.py?confId=458`, Super*B* PID meeting, March 18, 2008.

[4] I. Adam *et al.*, Nucl. Instrum. Methods Phys. Res., Sect. A **583**, 281 (2007).

[5] J. Va'vra *et al.*, Nucl. Instrum. Methods Phys. Res., Sect. A **639**, 404 (2011)282-286.

[6] J. Va'vra, Super*B* workshop, Perugia, June 2009, `http://agenda.infn.it/conferenceDisplay.py?confId=1161`, and Super*B* workshop, October 2009, SLAC, `http://agenda.infn.it/conferenceDisplay.py?confId=1742`.

[7] J. Va'vra *et al.*, Nucl. Instrum. Methods Phys. Res., Sect. A **606**, 404 (2009)404-410.

[8] E. Kravchenko, Super*B* workshop, June 2009, Perugia, `http://agenda.infn.it/conferenceDisplay.py?confId=1161`.

[9] J.Benitez *et al.*, SLAC-PUB-12236, October 2006.

[10] J. Va'vra *et al.*, SLAC-PUB-12803, March 2007.

[11] J. Benitez *et al.*, Status of the Fast Focusing DIRC (FDIRC), Nucl. Instrum. Methods Phys. Res., Sect. A **595**, 104 (2008) 104-107.

[12] J. Va'vra, *Simulation of the FDIRC optics with Mathematica*, SLAC-PUB-13464, 2008; and *Focusing DIRC design for Super*B, SLAC-PUB-13763, 2009.

[13] D. Roberts, Super*B* workshop, October 2009, SLAC, *Geant4 model of FDIRC*, `http://agenda.infn.it/conferenceDisplay.py?confId=1742`.

[14] M. Maino, Charactherisation of Multi-Anode Photomultiplier Tubes in Milano-Bicocca, Super*B* workshop, Frascati, March 2012, `http://agenda.infn.it/conferenceDisplay.py?confId=4441`.

[15] G. Varner, Deeper Sampling CMOS Transient Waveform Recording ASICs, TIPP conference, June, 2011, Chicago, `http://www.phys.hawaii.edu/~varner/TIPP_DeeperWFS_ASICs_10jun2011_varner.pdf`.

[16] C. Beigbeder, Status of FDIRC electronics, Super*B* workshop, Elba, May 2011, `http://agenda.infn.it/conferenceOtherViews.py?view=standard&confId=3352`.

[17] C. Field *et al.*, *Development of Photon Detectors for a Focusing DIRC*, Nucl. Instrum. Methods Phys. Res., Sect. A **553**, 96 (2005) and SLAC-PUB-11107, 2004.

[18] H. Kyushima *et al.*, *The Development of Flat Panel PMT*, Hamamatsu Photonics K.K., Electron Tube Center, Nuclear Science Symposium Conference Record, 2000 IEEE.

[19] R. Montgomery *et al.*, Multianode Photomultiplier Tube Studies for Imaging Applications, presented as NDIP conference poster, Lyon, France, 2011.

[20] F. Gargano, Update on H8500 test in Bari, Super$B$ workshop, Frascati, March 2012, http://agenda.infn.it/conferenceDisplay.py?confId=4441.

[21] J. Va'vra, FDIRC status, Super$B$ workshop, Elba, May 2011, http://agenda.infn.it/conferenceOtherViews.py?view=standard&confId=3352.

[22] G. Simi, H-8500 studies, Super$B$ workshop, Frascati, December 2011, http://agenda.infn.it/conferenceOtherViews.py?view=standard&confId=4107.

[23] C. Pauly, Single photon detection with H-8500 MaPMTs for the CBM RICH detector, DPG Munster, March 2011, http://www.gsi.de/documents/DOC-2011-Mar-233-1.pdf.

[24] P. Abbon *et al.*, Nucl. Instrum. Methods Phys. Res., Sect. A **595**, 204 (2008).

[25] J. Va'vra, FDIRC status, Super$B$ workshop, London, September 2011, http://agenda.infn.it/conferenceOtherViews.py?view=standard&confId=3827.

[26] N. Arnaud, Study of the glue transmission with di-muon *BABAR* data, 2009.

[27] J. Va'vra, spreadsheet accompanying each bar box construction, 1999.

[28] M. Benettoni, Fbox assembly procedure, Super$B$ workshop, Elba, May 2011, http://agenda.infn.it/conferenceOtherViews.py?view=standard&confId=3352.

[29] N. Mazziota, Activity in Bari, Super$B$ workshop, London, September 2011, http://agenda.infn.it/conferenceOtherViews.py?view=standard&confId=3827.

[30] N. Mazziotta, A study of after-pulse effect due to Helium permeation in the H8500 MaPMT, Super$B$ workshop, Frascati, December 2011, http://agenda.infn.it/conferenceOtherViews.py?view=standard&confId=4107.

[31] J. Va'vra, *SLAC cosmic ray telescope facility*, SLAC-PUB-13873, Jan. 2010.

[32] K. Nishimura *et al.*, *A detailed study of FDIRC prototype with waveform digitizing electronics in cosmic ray telescope using 3D tracks*, to be published.

[33] J. Vavra *et al.*, Development of pixilated TOF concept, Nucl. Instrum. Methods Phys. Res., Sect. A **595**, 270 (2008), Nucl. Instrum. Methods Phys. Res., Sect. A **606**, 404 (2009), Nucl. Instrum. Methods Phys. Res., Sect. A **629**, 123 (2011), and overall summary in DOE OHEP Review of Laboratory Detector R&D, Washington, July 24-26, 2012, available at http://www.slac.stanford.edu/~jjv/activity/fdirc/Vavra_DOE_review_detectorRD_2012.pdf.

[34] J. Va'vra, TOF with LYSO and G-APD, Super$B$ workshop, Frascatti, April 2011, http://agenda.infn.it/conferenceDisplay.py?confId=3410, Pixilated TOF options, Sept. 2011, http://agenda.infn.it/conferenceDisplay.py?confId=2303.

[35] D. Breton, E. Delagnes and J. Maalmi, *Picosecond time measurement using ultra fast analog memories*, talk and proceedings at TWEPP-09, Paris, September 2009. **Not used (2012/08/28)**

[36] G. Varner, Nucl. Instrum. Methods Phys. Res., Sect. A **538**, 447 (2005), Nucl. Instr. Methods Phys. Res., Sect. A **538** (2005) 447. **Not used (2012/08/28)**

[37] L. Burmistrov, PhD. thesis, Université Paris Sud (2011), http://tel.archives-ouvertes.fr/tel-00673482. **Not used (2012/08/28)**